Nano-scale electronic inhomogeneities in ultra-thin superconducting NbN

Clémentine Carbillet

École Doctorale de Physique et Chimie des Matériaux - ED 397

Thèse

Soutenue le 24 octobre 2014

Pour l'obtention du grade de

docteur de l'université Pierre et Marie Curie

Discipline : Physique des solides

par

Clémentine Carbillet

Nano-scale electronic inhomogeneities in ultra-thin superconducting NbN

Co-dirigée par M. Dimitri Roditchev et M. Christophe Brun

Composition du jury :

M[me] Hélène Bouchiat	examinatrice
M. Christophe Brun	co-directeur
M. Claude Chapelier	rapporteur
M[me] Claire Marrache-Kikuchi	rapportrice
M. Dimitri Roditchev	directeur
M. Abhay Shukla	examinateur
M[me] Brigitte Leridon	Invitée
M. Konstantin Ilin	Invité

Institut des Nanosciences de Paris Case 840
4, Place Jussieu
75 252 Paris Cedex 05

École doctorale Physique et Chimie de Matériaux Case 115
4 place Jussieu
75 252 Paris cedex 05

Acknowledgements

First of all, I would like to thank the whole SNEQ (Spectroscopie des Nouveaux Etats Quantiques) team at INSP : my two supervisors, Dimitri Roditchev and Christophe Brun, as well as Tristan Cren, François Debontridder, Yves Noat, Stéphane Pons, Denis Fokin and Vassily Stoliarov. Their patience and goodwill most certainly contributed to make a success of this thesis. For three years, I enjoyed their extensive knowledge in physics, which they passed on to me with passion.
A special thanks to Vladimir Cerchez with whom I shared the first two years of my thesis and who introduced me to the Scanning Tunneling Microscopy measurements.

This thesis work gave rise to a strong collaboration with Brigitte Leridon at LPEM. I want to thank her for her precious help with transport measurements, as well as for her kindness and availability. This collaboration led to remarkable results.
Brigitte also gave me the great opportunity to perform transport measurements under high magnetic field at LNCMI-Toulouse. Thereby, I would like to thank Baptiste Vignolles for having welcomed me so kindly during this week. It was such a valuable experience for me.

I would like to thank Claude Chapelier and Claire Marrache-Kikuchi who accepted to be rapporteur of my thesis. Thanks also to Abhay Shukla and Hélène Bouchiat, who were also members of this committee.

It is Konstantin Ilin who realized the NbN thin films studied during this thesis. Many thanks to him for having elaborated the samples I needed when I asked him. Thanks also for having welcomed me in his lab for a week and for having taken the time to teach me the elaboration process. It was precisely what I needed in order to get a better understanding of the NbN system.

Sergio Caprara and Marco Grilli, thank you for the calculations of the OD superconducting fluctuations.Your theoretical work helped us to understand and interpret the experimental results.
Thanks also to Lev Ioffe and Boris Altshuler for those fruitful discussions and for helping us in the interpretation of our STM/STS data. I am very much looking forward to collaborate with you.

While studying NbN thin films, I met a lot of people who shared their knowledge in their own field of physics with me.
Thus, I would like to thank Dominique Demaille and Ludovic Largeau, who helped me with the Transmission Electron Microscopy measurements. It was quite a hard work to thin the sapphire down. That is why I would like to thank Melanie Escudier who welcomed me in her lab and gave me the necessary tools to implement such a process. Thanks also to

Yannick Klein who introduced me to transport measurements with the PPMS. This could not have been possible without Francis Breton, who realized the precious sample holders for me. I thank him for that. Thanks to Laura Thevenard and Nicolas Bergeal who taught me the art of micro-bonding. This technique saved my transport measurements. And finally, thanks to Cheryl Feuillet-Palma, for her great efficiency and mastery of lithography process, without whom it would have been impossible to realize the NbN meander.

I also want to thank all the people who helped me in the everyday laboratory life : Lucdivine Bonnamy and Stéphanie Lagarde. Of course Sophie Hameau with whom I shared the office for one year, it has been a pleasure.

During this thesis, I have been very lucky to meet other students with whom I shared nice moments during coffee breaks and Thursday lunches : Lise, Gerbold, Sylvain, Bruno, Leonard, Rémi, Diego, and I am pretty sure that I am missing some of you.

Last but not least, I would like to thank all my friends who supported and encouraged me : Caroline, Karima, Camille, Timothée, Marie, Alice and Lucien. Your presence acted like a safety-valve during these three years. A special thanks to Dora who, by means of her own PhD experience, was able to give me precious advice at the most opportune moments. A great thanks to my family, my parents, my sisters and my brothers who had enough patience and kindness to support me. And finally, I want to thank Yacine who took care of me and never stopped encouraging me.

Abstract

Superconductor-insulator transition in NbN ultra-thin films

In order to better understand the various processes taking place at the superconductor-insulator transition (SIT), we have probed simultaneously the global and local electronic properties of NbN ultrathin films, elaborated *ex-situ* on sapphire substrate. The transition was approached by reducing the films thickness, increasing the normal state square resistance to several kiloOhms. The corresponding Tc's of the studied films ranged from about Tc $\sim$ 15K, which is close to T_{C-bulk}, to Tc $\sim$ 3.8K (Tc/T_{C-bulk} $\sim$ 0.23). In the range $0.4T_{C-bulk}$<Tc< T_{C-bulk} resistivity measurements are consistent with Finkelstein's reduction of Tc induced by disorder and electron-electron repulsion. Local scanning tunneling spectroscopy (STS) measurements show the emergence of granularity in the superconducting properties upon Tc reduction, as well as the progressive development of a strong Altshuler-Aronov background in the dI/dV(V) tunneling spectra, in agreement with Finkelstein scenario. For the most disordered film (Tc $\sim$ 3.8K), simultaneous *in-situ* resistivity and STS measurements allowed us to follow at the same sample area the evolution of these emergent granular superconducting properties as a function of temperature and magnetic field, which demonstrate a percolative behavior of the transition to the bad-metal normal state. This local picture finds an interesting signature in the change of the dimensionality of the Aslamasov-Larkin fluctuations above Tc from 2D to 0D. Besides, such a study is particularly interesting to better understand the various phenomena occurring in and limiting the behavior of single-photon detectors patterned out of NbN films.

Keywords

Superconductor-insulator transition, disordered superconductors, scanning tunnelling microscopy and spectroscopy (STM/STS), superconductivity, ultra-thin films, NbN, single photon detectors

---

Transition supraconducteur-isolant dans des films minces de NbN

Afin de mieux comprendre les différents processus qui apparaissent à la transition supraconducteur-isolant (SIT), nous avons sondé simultanément les propriétés électroniques globales et locales de films ultra-minces de NbN, élaborés *ex-situ* sur un substrat de saphir. La transition isolante a été approchée en réduisant l'épaisseur des échantillons, augmentant la résistance par carré de l'état normal jusqu'à plusieurs kiloOhms. Les Tc correspondant aux films étudiés varient de Tc $\sim$ 15K qui est proche de T_{C-bulk} à Tc $\sim$ 3.8K

($Tc/T_{C-bulk} \sim 0.23$). Dans la gamme 0.4 T_{C-bulk}<Tc< T_{C-bulk}, les mesures de résistances sont en accord avec la loi de Finkelstein pour la réduction de Tc induite par le désordre et les intéractions électron-électron. Les mesures de spectroscopie tunnel locale (STS) montrent l'émergence d'une granularité dans les propriétés supraconductrices en réduisant la Tc, ainsi que le développement progressif d'un fort fon Altshuler-Aronov dans les spectres tunnel dI/dV(V), ce qui est en accord avec le scenario de Finkelstein. Pour l'échantillon le plus désordonné ($Tc \sim 3.8K$), des mesures de résistance in-situ et de STS en simultané nous ont permis de suivre sur la même zone de l'échantillon, l'évolution des propriétés supraconductrices de cette granularité émergente en fonction de la température et du champ magnétique, qui ont démontré un comportement percolatif de la transition dans l'état normal de mauvais métal. Cette étude locale a trouvé une confirmation dans le changement de dimensionnalité des fluctuations Aslamasov-Larkin au-dessus de Tc de 2D à 0D. En outre, une telle étude est particulièrement intéressante pour comprendre les différents phénomènes qui se produisent, limitant le fonctionnement des détecteurs de photon unique basé sur les films de NbN.

Mots-clefs

Transition supraconducteur-isolant, supraconducteurs désordonnés, microscopie et spectroscopie à effet tunnel (STM/STS), supraconductivité, films ultra-minces, NbN, detecteur de photon unique

Contents

Introduction

The superconductor-insulator transition has been discovered several decades ago when decreasing the thickness of samples in order to search for superconductors with high critical temperatures. Currently, the topic experiences a renewed success, in particular thanks to the new experimental contribution from local probe techniques. Moreover, it has been demonstrated that some superconducting features in disordered thin films show some similarities to what was observed in high Tc copper-oxide based superconductors. It boosted an additional interest of the physics community for this kind of thin films.

We have chosen smooth NbN thin films to study the superconductor-insulator transition. These samples are polycrystallines, and the superconductor-insulator transition can be tuned either by varying the magnetic field, the thickness of the NbN layer or also the films stoichiometry. The study of such samples is particularly interesting to better understand the microscopic processes responsible of the superconducting-insulating transition. The films used for this thesis work were elaborated by our collaborator Konstantin Ilin at the Karlsruhe Institute of Technology who also fabricates single-photon detectors patterned out from NbN films. This makes the study of these films even more interesting. Indeed, it has recently been demonstrated that the maximum detection efficiency occurs for films thicknesses close to the superconductor-insulator transition.

On one hand, this thesis work aims addressing several questions concerning the mechanisms involved in the superconductor-insulator transition and, on the other hand, we would like to contribute to better understand the operating mode of single-photon detectors.

This thesis is organized in 7 chapters as described below:

Chapter 1: Experimental context: introduction to the superconductor-insulator transition and state-of-the-art
The study of the superconductor-insulator transition began several decades ago. There is a significant number of papers relating the results obtained both theoretically and experimentally, on a large variety of materials.
In this chapter, we compare the systems that exhibits a superconductor-insulator transition discovered when decreasing the film thickness. Then, we describe the three scenario developed to explain the superconductor-insulator transition. These two parts are based on the thesis of Olivier Crauste [Cra10] that constitutes a very good review of these concepts.
Finally, we describe the international context in which the work done during this thesis has been performed. We try to give an overview of the previous recent works on the superconductor-insulator transition, by discussing the main results obtained with various

experimental techniques.

Chapter 2: Samples fabrication process and characterization
The homogeneous NbN thin films studied during this thesis were elaborated in Karlsruhe Institute of Technology by our collaborators. The structural properties of films play a key role in determining the electronic properties at low temperature. We used Transmission Electron Microscopy and transport measurements to characterize the samples both structurally and electrically. It enabled us to suggest that the SIT corresponds to so-called homogeneous transition and that in addition the resistance and the superconducting transition temperature of the films evolve with time and thermal cycling. In this chapter, we describe the fabrication process of the NbN thin films and how we characterized it before further study.

Chapter 3: Experimental setup
Many techniques can be used to study the superconductor-insulator transition. However, Scanning Tunnelling Microscopy and Spectroscopy is a very promising tool since it gives a direct access to the local density of states. Combined with transport measurements, it becomes even more interesting because it enables one to compare the local conductance measurements of the sample with the global conductance. First, we have performed STM/STS measurements and transport measurements in separated experimental setups. Those results will be presented in chapter 5. Then we have used another more advanced setup and modified it to be able to measure *in-situ* the resistance of the thin films in the STM head. The results obtained are detailed in chapter 6.
After an introduction to electron tunnelling theory using the Bardeen work and Tersoff and Hamman work, we describe the experimental aspects of STM. Then, we depict the main characteristics of the experimental setups used during this thesis: STM M2, STM M3 and the Physical Properties Measurement System for the transport measurements.

The next three chapters concern the experimental results we obtained when studying the superconductor-insulator transition on the NbN thin films.

Chapter 4: Effect of magnetic field on the superconducting properties
A great effort has been made during this thesis to characterize the samples by transport measurements. It finally lead to interesting results. First, we studied the superconductor-metal transition induced by varying the magnetic field. It enables us to suggest the existence of a quantum critical point. Then, thanks to very high magnetic field measurements, we were able to drive the films to the normal state and to study the Aslamasov-Larkin fluctuations above the critical temperature.
After a review of the quantum phase transition theory and the different scenario that can be used to interpret the results, we present a scaling law analysis of our transport results obtained on NbN thin films.

Chapter 5: Effect of the film thickness reduction on the local superconducting properties
Before the beginning of this thesis, some results were already obtained in our group by scanning tunneling microscopy and spectroscopy on these NbN thin films. The superconductor-insulator transition has been approached by varying the thickness, reducing the critical temperature. The local superconducting properties probed by STS as a function of magnetic field and the film thickness are presented in this chapter.

First, we show the transport characteristics of the studied samples. Then, we demonstrate the BCS-like behavior of thick samples and how it becomes more and more unconventional when approaching the insulating transition. In the last section of this chapter, we present an interpretation and discussion of the results with respect to the current literature.

Chapter 6: Spectroscopic study of a thin film closer to the superconductor-insulator transition
In order to be able to measure *in-situ*, in the STM chamber, the resistance of the samples, we made some modifications of the experimental setup M3. It enables us to perform a further study of a sample which has a Tc of 3.8K, the closest to the superconductor-insulator transition among the studied samples. We succeeded to stay at the same place of the sample during all STS experiments and could realize a complete study of the B-T phase diagram (0T $\rightarrow$ 7T and 300mK $\rightarrow$ 7K) of the local tunneling characteristics. We also examined in details the V-shape background on which the superconducting gap develops, and found that it is linked to strong electron-electron interactions effects in the presence of disorder.
First, the effect of the temperature on the local superconducting properties is shown and then the effect of magnetic field is presented. In the second part, the Altshuler-Aronov background is studied, an interpretation and a discussion of the results are presented at the end.

Chapter 7: Application: Toward a local study of superconducting nano-stripes used for single-photon detection
The NbN thin films studied during this thesis are also used to fabricate single-photon detectors. The operating principle of these detectors is described in the first section of this chapter. In order to study such a device, we used nanofabrication techniques with electronic lithography to elaborate a meander, starting from one of our NbN thin film. The fabrication process is thus explained in the second part of this chapter. Finally, we have measured the meander structure by using an AFM/STM. Unfortunately, due to technical dysfunctions, we were not able to performed yet a spectroscopic STM study at low temperature. The AFM image of the structure obtained during this experimental run is shown in the last part of this chapter.

The **conclusion** summarizes the results obtained during this thesis and gives the outlook for the reminder of the study of the superconductor-insulator transition in thin films of NbN.

Chapter 1

Experimental context: introduction to the superconductor-insulator transition and state-of-the-art

Contents

The study of the superconductor-insulator transition began several decades ago. There is a significant number of papers relating the results obtained both theoretically and experimentally, on a large variety of materials. The first two parts of this chapter are based on the thesis of Olivier Crauste [Cra10] that constitutes a very good review of these concepts.

1.1 Granular versus homogeneous systems in the superconductor-insulator transition

It has been observed that when decreasing the thickness of some film, the Tc decreases. The first observation of this effect [STKC70], and the majority of the films showing the destruction of the superconductivity when reducing the thickness were quenched-condensed [BA71, DGR78, DBC$^+$80, OJG85]. It means that the substrate is maintained at low temperature during the evaporation of the film. No particular precautions were made regarding the wetting layer on the substrate. These films are granular.
Then, it has been discovered that when adding a wetting layer onto the substrate before depositing the thin film, it is possible to synthesize more smooth and homogeneous thin films. A sublayer of Ge was often used [GB84]. Later on, smooth Pb and Bi thin films [HLG89] with no wetting layer have been realized and studied.
Thus, it is clear that the structural properties of the samples play a key role in determining the electronic properties at low temperature. Thereby, the metallic films presenting a superconductor-insulator transition when decreasing the film thickness are commonly classified into two groups:

- Granular systems
- Homogeneous systems

In perfectly crystalline thin films, synthesized in UHV conditions, superconductivity has been observed and studied down to a single atomic layer; it was the case of Pb or In which were analyzed by means of scanning tunneling microscopy and spectroscopy [ZCL$^+$10]. A superconductor-insulator transition has not been observed in such system upon thickness reduction.
The superconductor-insulator transition can be induced by varying the thickness but not only. Increasing the magnetic field, changing the doping or the disorder can also induce the transition.

1.1.1 Granular thin films

Granular systems can be described as an array of Josephson junctions. Indeed, the grains composing the film are embedded in an insulating matrix and coupled together thanks to the tunneling effect. To illustrate the behavior of the samples composing this group, the study of Jaeger et al. [JHOG89] will be taken as an example.
Granular thin films are characterized by a disappearance of superconductivity when reducing their thickness in a way similar to what can be seen on figure 1.1. The superconducting critical temperature remains almost constant when decreasing the thickness of the films but become wider : the zero-resistivity critical temperature decreases but the onset critical temperature $T_{c,onset}$ at which the resistivity starts droping does not change much; even for films close to superconductor-insulator transition.

Otherwise, a re-entrance phenomenon of the superconductivity is often observed in granular systems. The resistance starts to decrease when decreasing the temperature, saturate and finally increases back when further decreasing the temperature. It is a typical

behavior of these systems. One important feature is also that the superconductor-insulator transition is observed when reducing the nominal thickness in a very narrow window of the order of few Angströms. For instance, in Ga samples (see figure1.1) [JHOG89], the thickness has been reduced only by approximately 2 Angströms between the lower and the upper R(T) curves.
For the insulating state, the evolution of the resistance as a function of temperature shows a characteristic activated exponential behavior associated to strong localization effects. Thus, the transition in granular thin films has been interpreted [Efe80, STKC70] as a competition between the Josephson coupling energy between grains and the Coulomb charging energy. Granular systems can be seen as an array of metallic particles embedded into an insulating matrix or separated by insulating grain boundaries. In the superconducting state, the granules are coupled together by Josephson junctions. It means that Cooper pairs can tunnel from one granule to another. The Coulomb charging energy corresponds to the change in energy of a grain when adding or removing an electron. It plays a crucial role in the transport properties in the insulating regime when electrons are localized in the grains, such that the charge of each grain is quantized [BLVE07].
At last, the granular structure induces fluctuations of the phase of the superconducting order parameter, and these fluctuations become more and more important when approaching the insulating transition.

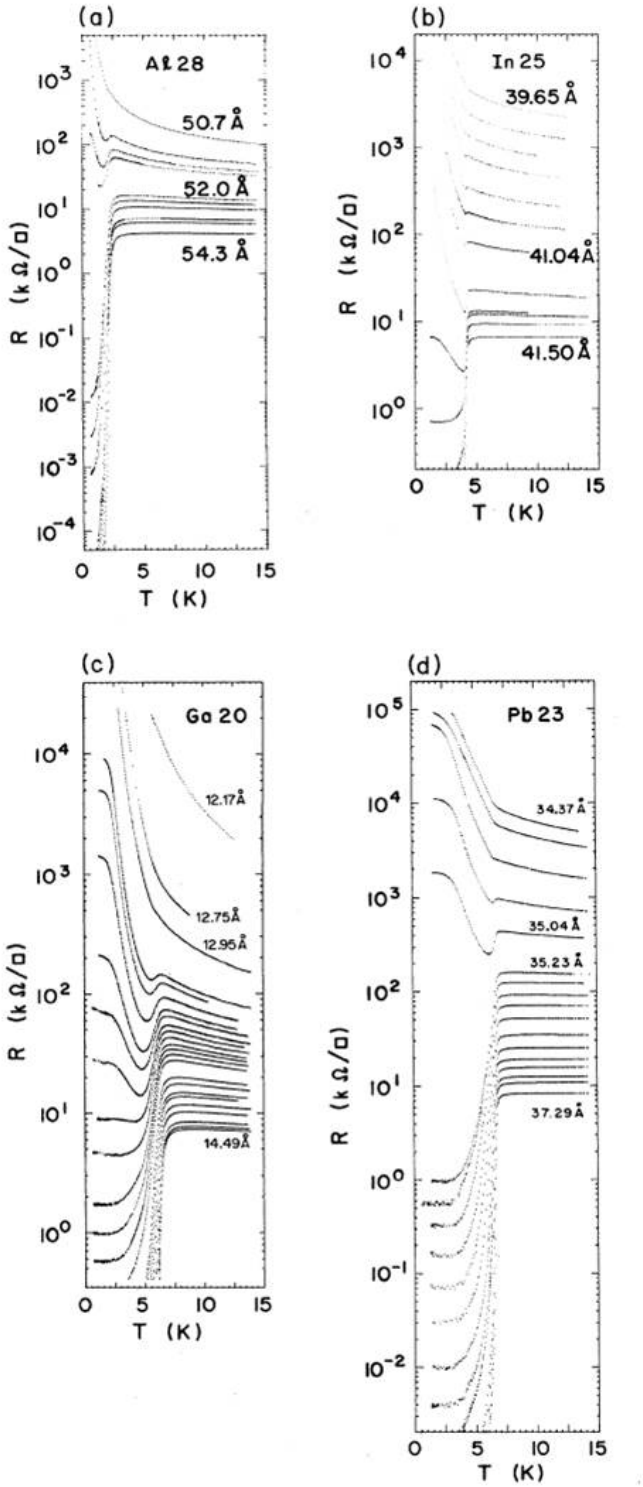

Figure 1.1: *Evolution of R(T) curves for so-called granular superconductors a) Al, b) In, c) Ga and d) Pb as a function of film thickness. In both cases, a superconductor-insulator transition is observed. (Extracted from [JHOG89].)*

1.1.2 Homogeneous thin films

Homogeneous thin films have not the same structure as compared to granular systems. Indeed, it has been shown that a thin wetting layer of Ge helps to have a better electronic coupling between grains. The best known example of superconductor-insulator transition in homogeneous thin films is that of Bismuth studied by Haviland et al. [HLG89], and is shown in figure 1.2. The samples were prepared by depositing a thin Bi film onto a liquid-He-cooled substrate that was first coated by a 6Åthick Ge layer.

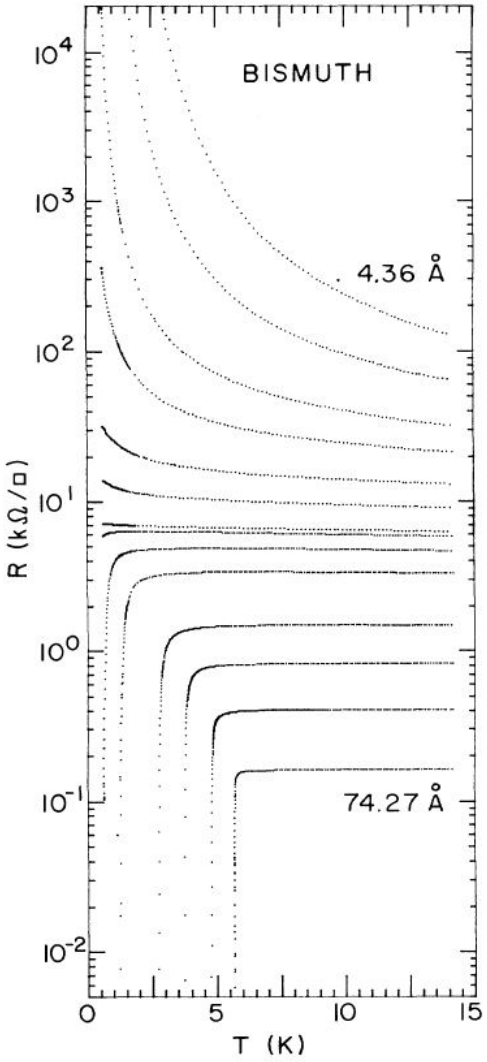

Figure 1.2: *Resistance evolution as a function of temperature for different thin film thicknesses of Bi on Ge extracted from [HLG89]. This is the characteristic behavior of superconductor-insulator transition in homogeneous systems.*

Homogeneous systems exhibit a completely different behavior with respect to granular systems. First, the Tc decreases continuously with thickness reduction and is close to zero before the insulating transition. The superconducting transition remains sharp when decreasing the film thickness but in some cases it broadens when approaching the transition. No re-entrance phenomenon of the superconductivity is observed in homogeneous thin films. To induce the superconductor-insulator transition, the thickness has to be reduced over a range of few tens of Angströms. For instance in Bismuth, the thickness is reduced

by about 70 Angströms. This class of systems contains the majority of thin films that are studied now. Depending on the importance of electron-electron interactions in the homogeneously disordered systems, two different behaviors can be distinguished.
The scaling theory of localization [AALR79] and the modelization of Coulomb interactions [AAL80] are at the basis to explain the destruction of superconductivity in disordered homogeneous systems. Then, Finkelstein [Fin87, Fin94] developed the formula that predict the evolution of the Tc in these systems.

1.2 Theory for the superconductor-insulator transition

1.2.1 Bosonic scenario

The first approach is based on the quantum phase transition to explain the superconductor-insulator transition in homogeneous films. It has been developed M. Fisher [Fis90] and describe the suppression of the superconductivity by using phase fluctuations of the order parameter and the Cooper pairs - vortex duality. Thus, before developing in more details the bosonic scenario for the transition, we need to introduce several notions related to superconductivity.

In the **Ginzburg-Landau** theory [Tin04] the supercurrent density is defined as :

$$J_S = \frac{2e}{m}|\psi(\overrightarrow{r})|^2(\hbar\nabla\varphi(\overrightarrow{r}) - 2eA(\overrightarrow{r})) \simeq 2en_s v_s \tag{1.1}$$

The complexe wavefunction $\psi = |\psi|e^{i\varphi}$, where $|\psi|$ is the amplitude and φ is the phase, is an order parameter that describes the superconducting electrons. $n_s = |\psi(\overrightarrow{r})|^2$ represent the density of superconducting electrons. And v_s is the superfluid velocity. This formalism allows for studying non-linear effects of the magnetic field or temperature that are strong enough to render n_s small. In the ground state the amplitude is maximum and the phase is constant, $\varphi(\overrightarrow{r})$=cste.
Ginzburg and Landau introduced the Ginzburg-Landau coherence length ξ, a characteristic scale on which $\psi(\overrightarrow{r})$ may vary in space upon external action (field, temperature, current). The ratio between ξ and λ which is the London penetration depth of the magnetic field, is $\kappa = \lambda/\xi$. For the materials with low κ the magnetic field is expelled (Meissner effect). The superconductor resists to rising magnetic field until the superconductivity is destroyed at H_C. For materials in which $\kappa > 1/\sqrt{2}$, Abrikosov [Abr57] have shown that there are not one but two critical fields. The superconductivity is not destroyed at H_C, but there is a continuous increase in flux penetration between H_{C1} and H_{C2}. Between these two critical fields, the flux penetrates in a regular array of quantum tornadoes called vortices. Each vortex carries a quantum of flux ϕ_0. Over H_{C2}, the superconductor recovers its normal state. Thus, κ parameter fixes the limit between two classes of superconductors called type I and type II. NbN we study in this work is a type II superconductor. It means that two critical magnetic fields define its behaviour (see figure 1.3).
By using the Ginzburg-Landau equation, it is possible to show that a vortex corresponds to a rotation of the phase φ of the order parameter around a specific point -vortex center- where the phase diverges as $\varphi(\overrightarrow{r}) \sim 1/r$. Around this singular point, there is a phase gradient, and the phase accumulation along any close loop around the point is 2π. This phase gradients generate currents around the vortex core (formaula 1.1) circulating in the direction opposite to the Meissner current. As can be seen on figure 1.4, the density of superconducting electrons $|\psi|^2$ turns out to go to zero in the vortex core. Thus the vortex

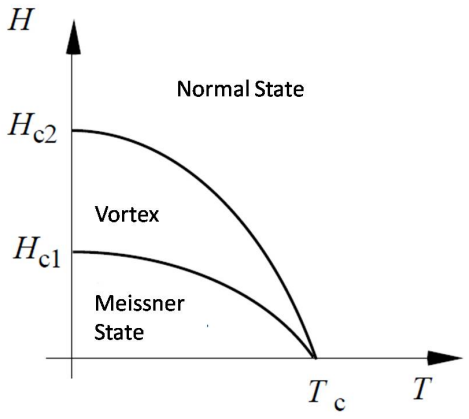

Figure 1.3: *Phase diagram of the type II superconductors.*

can be seen as a spatial excitation of the superconducting condensate where both $|\psi|$ and φ vary on a scale of ξ.
In practice, in thin superconducting films, the magnetic field penetrates fully the film and thus, $B \simeq H/\mu_0$ everywhere; screening of the magnetic field in the direction perpendicular to the surface is negligible.

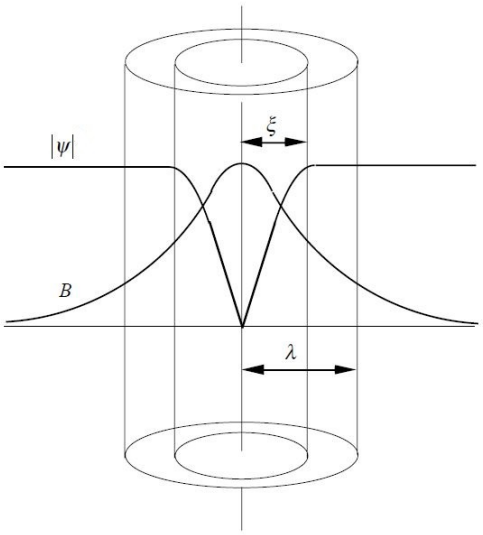

Figure 1.4: *Shape of the magnetic field B and the density of Cooper pairs $|\psi|$ close to a vortex. ξ is the coherence length that represent the size of the vortex core. λ is the penetration length which correspond to the size over which the magnetic field is screened by the super-current rotating around the vortex.*

The Berezinskii-Kosterlitz-Thouless transition [KT73] is a phase transition occurring in 2D for a system with an order parameter with 2 continuous components which could be amplitude and phase. It is based on the possibility of spontaneous generation of vortices in superconducting systems at temperature smaller than Tc_0, the bulk superconducting transition. These vortices form a gas of fluctuating regions in the superconductor. In this approach, the vortices are generated by pairs that have opposite directions of circu-

lating currents. They form so-called vortex-antivortex pairs. These vortices move, diffuse and after a collision, within a finite time, they annihilate each other by meeting with an opposite vortex. When decreasing the temperature and reaching $T_{BKT} < Tc_0$, a true transition to a zero-resistance superconducting state is induced. The spontaneous generation of vortices ceases and their concentration decreases exponentially. Moreover remaining vortices-antivortices bind by pairs. Thus, T_{BKT} corresponds to the critical temperature at which the vortex-antivortex pairs dissociate. According to this approach, in 2 dimensional superconductor, moving vortices are presents with Cooper pairs when $T_{BKT} < T < Tc_0$.

The quantum theory of M. Fisher [Fis90] focuses on the possibility of having a superconductor-insulator transition at T=0 induced by magnetic field or disorder as seen in the phase diagram in figure 1.21. In the absence of disorder, when increasing the magnetic field over B_M, the superconductor becomes normal. But in the presence of disorder, a vortex glass state appears in a finite range of temperature. In this phase, Cooper pairs are condensed and the vortices are localized. Over B_C, it becomes an electron glass which is an insulating state in which Cooper pairs are localized and vortices are condensed. This state is called the Bose glass in the bosonic scnerio. Thus, there is a quantum phase transition between the vortex glass and the Bose glass when increasing the magnetic field. The quantum phase transition theory will be detailed in chapter 4, to present the experimental signatures measurable at finite temperature.
Thus, in this scenario, there is a duality between the Cooper pairs and the vortices. The Cooper pairs - vortex duality enables to have an equality between the Cooper pair conductivity and the resistance of the vortices. This duality is used to calculate the critical resistance which corresponds to the resistance value that separates the superconducting state and the insulating state. It is predicted to be equal to the quantum of resistance for pairs $R \sim 6.45k\Omega$.
The phase transition established by M. Fisher is based on phase fluctuations of the order parameter due to the existence of vortices and disorder. The amplitude of the superconducting order parameter is assumed to be constant in this model.

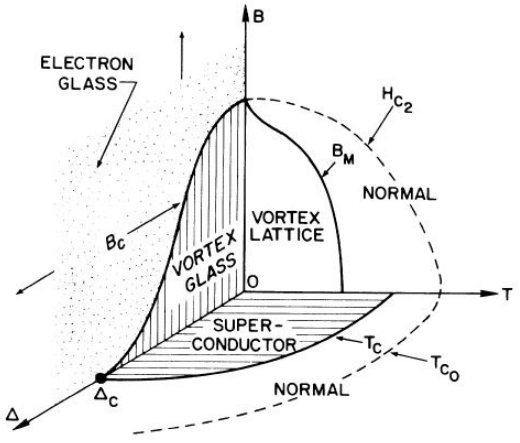

Figure 1.5: *Schematic phase diagram drawn by M. Fisher and extracted from [Fis90].* Δ *is the disorder, T the temperature and B the magnetic field. These three axis represent the three different ways to induce the superconductor-insulator transition.*

1.2.2 Fermionic scenario

The Anderson's theorem has been developed in 1959 [And59], and explain that non-magnetic impurities do not affect the superconducting critical temperature since Cooper pairs are formed out of time-reversed eigenstates. This theorem is valid for dirty superconductors but not to study strongly disordered systems, for which $k_F l$ is close to 1.

The localization effects has to be taken into account. Ma and Lee [ML85] extended the Anderson's theorem and shown that superconductivity can persists below the mobility edge when eigenstates become localized :

$$\rho \Delta l^D \geq 1 \tag{1.2}$$

Where ρ is the density of states, Δ is the superconducting gap and and l is the length of localization and D is the effective dimension of the sample. It means that the pairing of localized particles can occur if the energy gain Δ is larger than the energy level spacing of of particles confined within the localized length.

The electron-electron interactions have been introduced in the calculation of the Tc reduction when reducing the thickness of the films due to the work of ltshuler and Aronov [AAL80]. Indeed, they have shown that Coulomb interactions lead to e decrease of the effective density of states at the Fermi level. Fukuyama and Maekawa [MF81] as well as Kuroda and Takagi [TK82] first tried to calculate the effect of disorder and Coulomb interactions on the critical temperature of a superconducting film.

In the **Finkelstein model** [Fin87, Fin94], the Tc reduction in homogeneous systems is correctly describe by the following law:

$$\frac{Tc}{T_{C0}} = exp(-1/\gamma) \left\{ \left[1 + \frac{(t/2)^{1/2}}{\gamma - (t/4)} \right] / \left[1 - \frac{(t/2)^{1/2}}{\gamma - (t/4)} \right] \right\}^{1/\sqrt{2t}} \tag{1.3}$$

where T_{C0} is the bulk superconducting transition temperature without disorder, $\gamma = \ln(1/T_{C0}\tau)$, τ is the mean elastic scattering time and $t = \frac{e^2}{2\pi^2\hbar} Rsq$ is the normal state square resistance divided by the quantum of resistance. Thus, t is an indication of the amount of disorder in the system. In the fermionic scenario, no universal value of the critical resistance corresponding to the separation between the superconducting state and the insulating state has been found.
Finkelstein analysed a series of superconducting MoGe samples having various thickness. He plotted their Tc's as a function of Rsq and showed that they follow perfectly the law 1.3 (see figure 1.6).
In 1992, Valles et al. [VDG92] measured tunnel junction conductance of Bi films close to the superconductor-insulator transition. They have shown that the superconducting gap Δ and the critical temperature Tc decrease at the same rate and become very small when approaching the superconductor-insulator transition. It means that the suppression of the superconductivity could be attributed to the suppression of the order parameter. This is again in contradiction with the bosonic scenario in which the fluctuations of the phase of the order parameter are responsible for the destruction of the superconductivity.

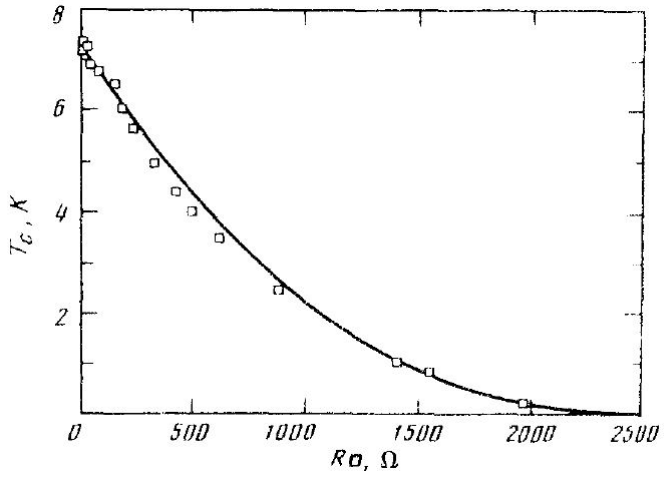

Figure 1.6: *Evolution of the Tc as a function of Rsq in MoGe samples extracted from [Fin87]. It follows perfectly the Finkelstein law for the reduction of Tc with increasing disorder.*

1.2.3 Fractal pseudo-spin model and numerical methods

More recently, Feigelman et al. [FIKC10] proposed a different scenario called the fractal "pseudo-spin" model to explain the superconductor-insulator transition in disordered thin films. This scenario also neglects Coulomb interactions and is also not based on the fluctuations of the superconducting order parameter. The fractal nature of the wave functions is the central phenomenon of this theory. The control parameter of the transition is the position of the Fermi level according to the Anderson mobility edge which is close to the region of localized states. Near the mobility edge, in disordered systems, the electrons wave functions have multi-fractal properties. It is thus possible to have correlations between two fractal wave functions and Cooper pairing becomes possible even if the Fermi level is below the mobility edge.

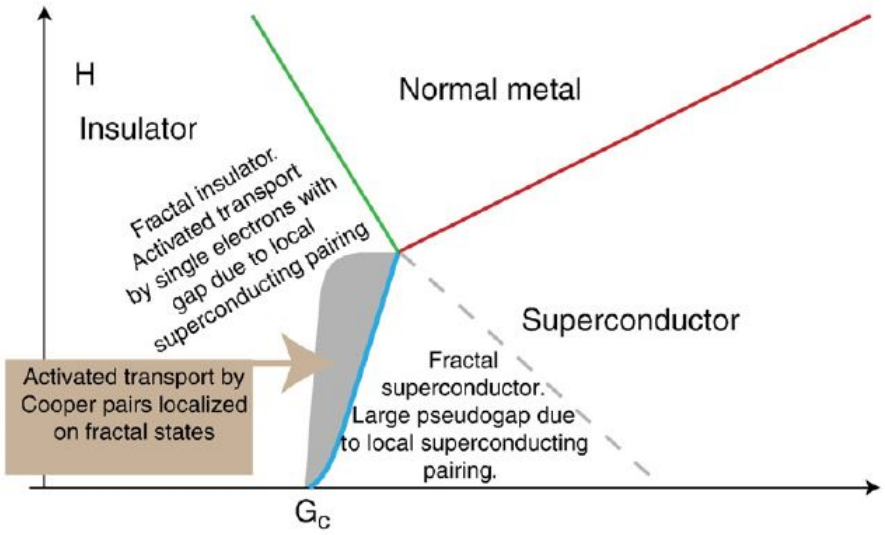

Figure 1.7: *Experimental phase diagram of homogeneously disordered films drawn by [FIKC10].*

Three regimes are distinguished in this approach at high disorder, and are visible in figure 1.7:

- The hard gap insulator state. Local pairing is still possible but there is no global coherence of the phase of the superconducting order parameter.
- The pseudogap state. It corresponds to a superconducting state that appears when the phase coherence develops between localized Cooper pairs.
- The fractal superconductor state. Without disorder, the BCS theory can be used to describe the system. When increasing disorder, close to the mobility edge, electrons start to localize and the fractal nature of the wave function must be taken into account.

In this model, on both sides of the superconductor-insulator transition, electrons are bound in pairs. The transition can be described in terms of the XY ordering of the Anderson pseudo-spin S_j. Hence the name given to this theory.
This theory has been developed to explain in particular the phenomena occurring at the superconductor-insulator transition in TiN, InO and Be ultra-thin films. The special features of the transition in these samples are the following:

- Direct transition between the superconducting state and the insulating state.
- Emergence of spatial inhomogeneities of the superconducting order parameter.
- Presence of a strong pseudo-gap above Tc.
- Disappearance of the coherence peaks when approaching the insulating state.

The fractal pseudo-spin model constitutes a recent attempt to summarize in one theoretical approach all the experimental observations when approaching the superconductor-insulator transition. Feigelman proposed a fully coherent theoretical picture describing the superconductor-insulator in disordered thin films. Other numerical models have been developed to describe the superconductor-insulator transition induced by disorder in thin films. Trivedi, Randeria et al. [GRT01, BLRT11] simulated the competition between superconductivity and localization and also ignored the Coulomb interactions. They considered a 2D lattice model of superconductivity with moderately strong local attraction with a negative-U Hubbard model and on-site disorder. They studied it by two numerical

methods: by solving the self-consistent Bogolyubov-de Gennes equations and by solving BCS pairing equations in the basis of exact single-electrons eigenstates. They observed that when increasing the disorder, the height of the coherence peaks gradually decreases, the gap is filling and a pseudo-gap persists above Tc. The spectra obtained when increasing disorder at a fixed temperature can be seen on figure 1.8. At weak disorder, the system can be described by the conventional BCS theory. The authors were able to simulate the local probe measurements and showed that the system becomes more and more electricaly inhomogeneous when increasing the disorder.

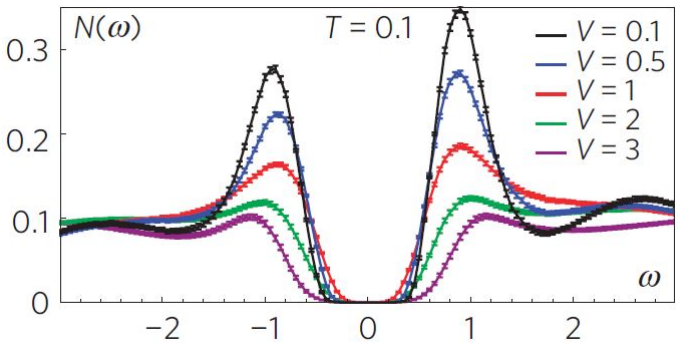

Figure 1.8: *Evolution of the local density of state $N(\omega)$ as a function of the disorder and at a fixed temperature extracted from [BLRT11]. A hard gap persists in the insulating while the coherence peaks exists only in the superconducting state.*

However, this analysis [GRT01, BLRT11] does not allow to study the physical properties of the system as a function of the coupling strength and the proximity of the Fermi energy to the localization edge. This corresponds to the new input of the pseudo-spin model developed by Feigelman et al. [FIKC10].

1.3 Recent results

1.3.1 Scanning tunneling spectroscopy measurements

The first significant results obtained with scanning tunneling spectroscopy measurements when studying the superconductor-insulator transition were performed on disordered TiN films in 2008 by Sacepe et al. [SCB$^+$08]. It constitutes the first direct observation of superconducting inhomogeneities in a nominally homogeneous conventional superconductor. These appear as spatial fluctuations of the gap in the tunneling conductance spectra, visible in figure 1.9. The inhomogeneities of the spectra are interpreted as an interplay between superconductivity and Anderson localization. Moreover, they observed that the ratio Δ/k_BTc increases with increasing disorder and that the apparent tunneling gap remains finite while Tc goes to zero, suggesting that Δ survives in the insulating state. It is also noticeable that the coherence peaks disappear in the most disordered samples. In further study, Sacepe et al. [SCB$^+$10] made a comparison between underdoped copper-oxide superconductors and TiN thin films. They highlighted the presence of a pseudogap state in TiN well above Tc. The origin of this pseudogap is interpreted as a suppression of the density of state by two-dimensional superconducting fluctuations which are enhanced by the proximity to superconductor-insulator transition. Sacepe et al. obtained more recently [SDC$^+$11] the same results in disordered InO films and claimed that, in this system, the route to the insulating behavior proceeds through the direct localization of Cooper pairs.

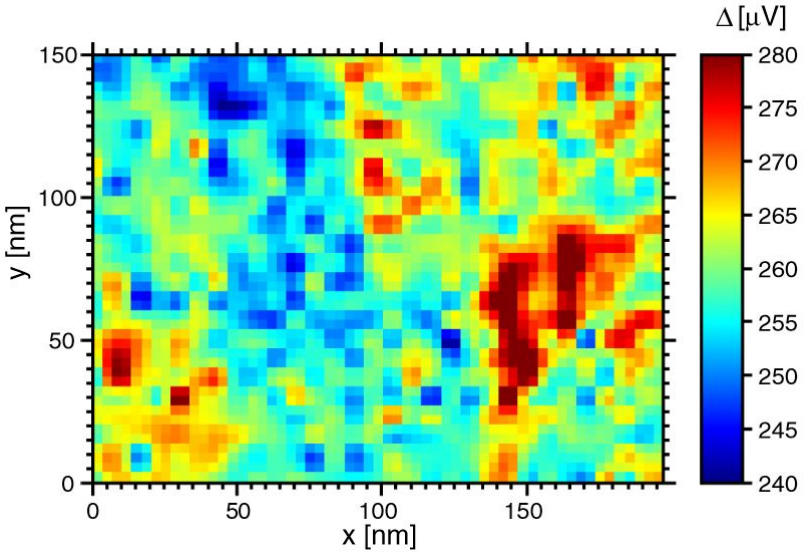

Figure 1.9: *Color map of the spatial inhomogeneities of the gap measured by STS in TiN and extracted from [SCB$^+$08].*

Further study on TiN thin films have been performed recently Kulkarni et al. [KSR$^+$14a] by using scanning tunneling microscopy and spectroscopy. They have shown that the tunneling gap develops on a strong Altshuler-Aronov background, and that the normal state local conductance also display the Altshuler-Aronov zero bias anomaly. They concluded that Coulomb interactions dominates the tunneling density of states at all temperatures and at high magnetic fields. In this work, the superconductor-insulator transition has been approached by using a thermal treatment. The increase of the resistance and decrease of

the Tc was achieved by heating the samples at 350°C in an ambient atmosphere. In a second work, Kulkarni et al. also succeeded to obtain atomic resolution images by using tunneling microscopy on their TiN films [KSR$^+$14b] and is visible on figure 1.10. They observed the presence of electronic charge density modulation appearing in the boundaries between two domains having different crystalline orientation. They observed that the conductance fluctuations measured by tunneling spectroscopy at energy close to the superconducting gap are influenced by these electronic charge density modulations.

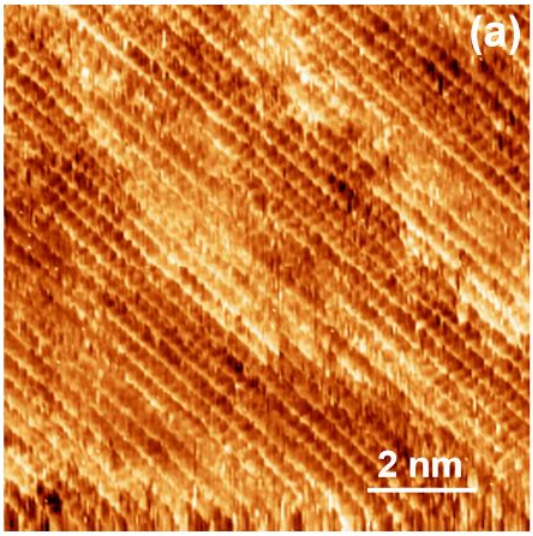

Figure 1.10: *Topographic image of the TiN film extracted from [KSR$^+$14b] and showing the atomic resolution on a 10nm x 10nm area.*

In parallel to these works, Raychaudhuri et al. studied the superconductor-insulator transition by various techniques including spectroscopic measurements in 50nm thick epitaxial NbN films deposited on MgO substrate. They made a study of the phase fluctuations in these system [CKS$^+$11, MKC$^+$11a] and explained how they play a central role in the formation of the pseudogap state that exists above Tc. Raychaudhuri et al. measured the local density of states of samples with different levels of disorder [CSK$^+$12]. For high disordered films, they observed the disappearance of the coherence peaks and the presence of a "V-shape" background that results of an Altshuler-Aronov type electron-electron interactions. They have shown that a conventional BCS superconductor can turn into an insulator due to strong phase fluctuations when increasing disorder. They also observed [CCK$^+$09] that the ratio Δ/K_BTc anomalously increases when increasing disorder.
Raychaudhuri et al. published more recently a paper [KDG$^+$13] where they show the evolution of the superconducting inhomogeneities as a function of temperature. The results can be seen on figure 1.11. They explain that at Tc, due to thermal fluctuations between the superconducting domains composing the sample, the phase coherence is destroyed. This will lead to the presence of coherent and incoherent Cooper pairs and to the measured pseudogap above Tc. They also calculate the correlations between the zero-bias conductance map and the average height of the coherence peaks and find a weak anti-correlation between the two. They conclude that the zero-bias conductance is possibly not governed by the order parameter alone.

Thus, local spectroscopic measurements can give precious informations about the super-

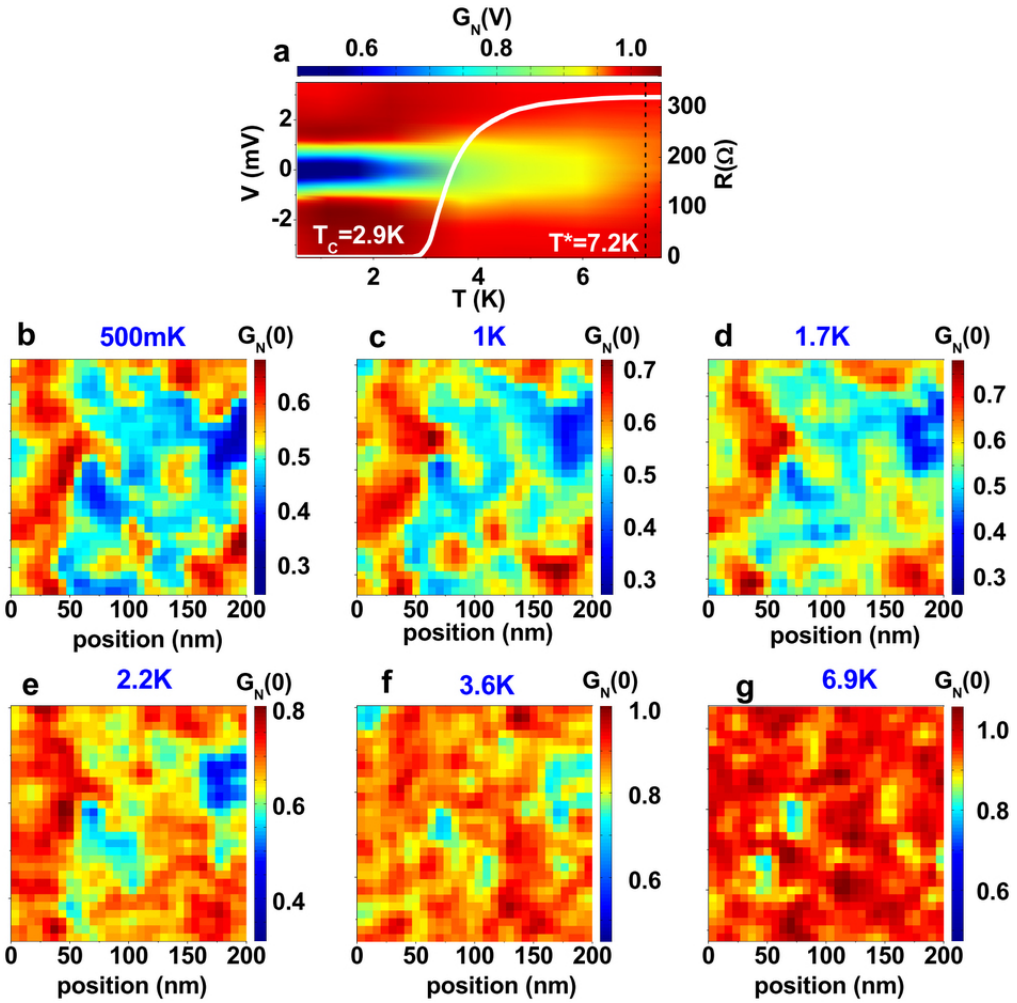

Figure 1.11: *Evolution of the superconducting inhomogeneities over the sample area as a function of temperature in epitaxial NbN film with a Tc of 2.9K extracted from [KDG+13].*

conducting state. The results already obtained on TiN, InO or NbN lead to different interpretations although the spectroscopic data are very close.

1.3.2 Transport measurements

First results on the superconductor-insulator transition have been obtained thanks to macroscopic transport measurements. The contribution of this experimental technique has steadily increased from that time. The literature is thus very rich, and this part will focus only on the most important and recent results.

The majority of the transport measurements lead to a scaling law analysis. The principle of this type of analysis is described in chapter 4. It enables to determine the critical exponents that define the dimensionality of the system and the universality class of the transition. But these exponents taken alone may not help describing the microscopic processes occurring at the transition. Transport measurements also bring useful informations about the Hall effect and the magnetoresistance.

A selection of results obtained on thin films by using transport measurements is summarized in [GD10]. The important point highlighted in this review is that there is no universal resistance that corresponds to the separation between the insulating state and

the superconducting state. Indeed, the quantum of resistance for pairs as a separatrix value between the two states has been found in a few number of systems as bismuth thin films [HLG89] and is visible in figure 1.12.

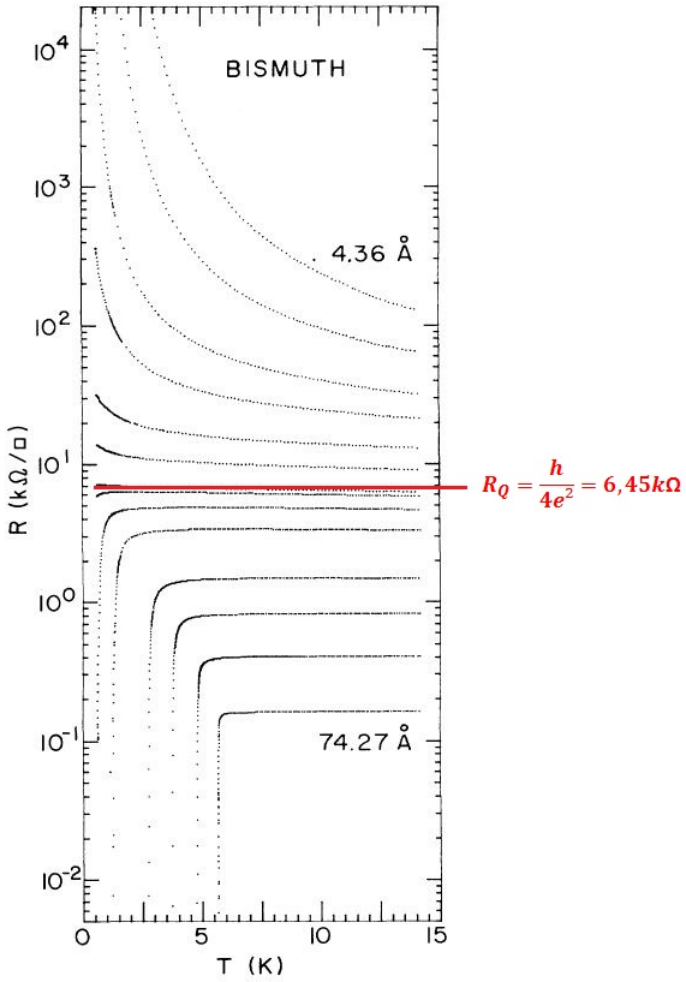

Figure 1.12: *Evolution of the resistance as a function of temperature for different film thickness extracted from [HLG89]. The separation between the superconducting and the insulating state appears for a resistance which is equal to the quantum of resistance for electron pairs.*

In InO thin films, a recent study performed by Shahar et al. [OKSS13] showed critical exponents $\nu z = 1.2$ see figure 1.13. This result is consistent with previous work on InO films [HP90]. The interpretation of the transport measurements carried out on TiN or InO both suggested that the insulating phase is a "Cooper pair insulator". Namely, the sample is formed of superconducting droplets embedded in an insulating matrix. Thus, the insulating state can be viewed as an array of Josephson junctions. This system has been studied in more details by Baturina and Vinokur [BV13]. They focused on the "superinsulator" state in a system made of superconducting islands connected by Josephson junctions. The phase diagram of these systems can be seen on figure 1.14.
The authors have shown that the critical component to observe the emergence of the superinsulator state is the high dielectric constant of the insulating phase. The later confines

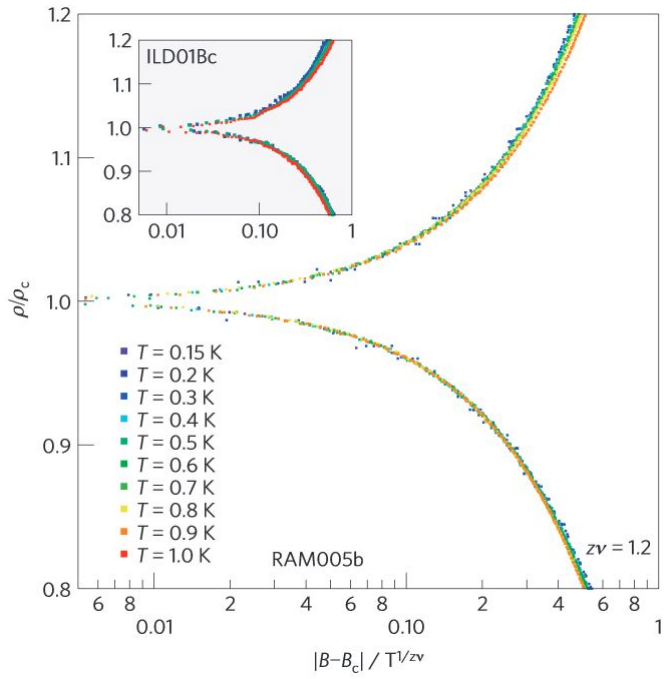

Figure 1.13: *Temperature scaling law analysis of the magnetic field tuned superconductor-insulator transition in an InO sample extracted from [OKSS13]. The critical exponents are found to be equal to νz=1.2.*

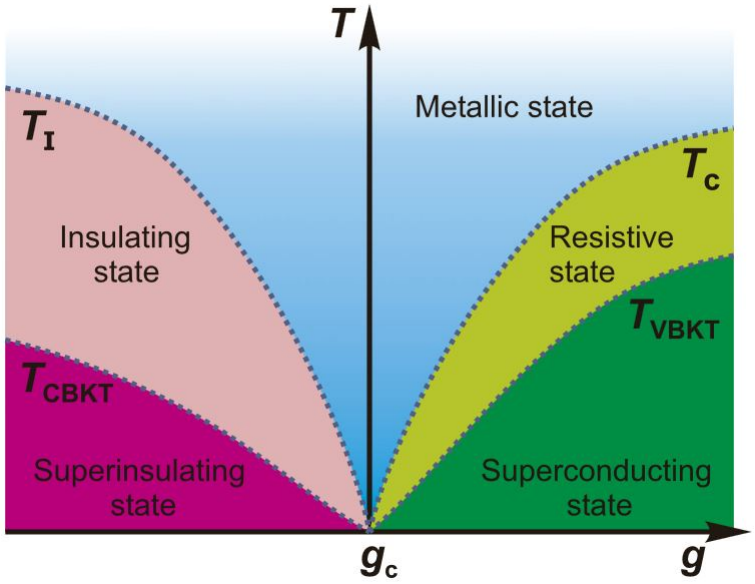

Figure 1.14: *Phase diagram T-g of the superinsulator-superconductor transition extracted from [BV13]. T is the temperature and g is the critical parameter. In the Josephson junction arrays, g represent the ratio of Josephson coupling and charging energy $g = E_J/E_C$ where E_J is the Josephson coupling energy of the two adjacent superconducting islands and E_C is the energy cost to transfer a Cooper pair between the neighbouring islands.*

the electric field and prevents from Coulomb screening.
The scaling law analysis can lead to other critical exponents values. This is the case for example of the results obtained by Markovic et al. [MCM$^+$99] in amorphous bismuth thin films. The scaling law analysis can be seen on figure 1.15 and gives $\nu z = 0.7$.

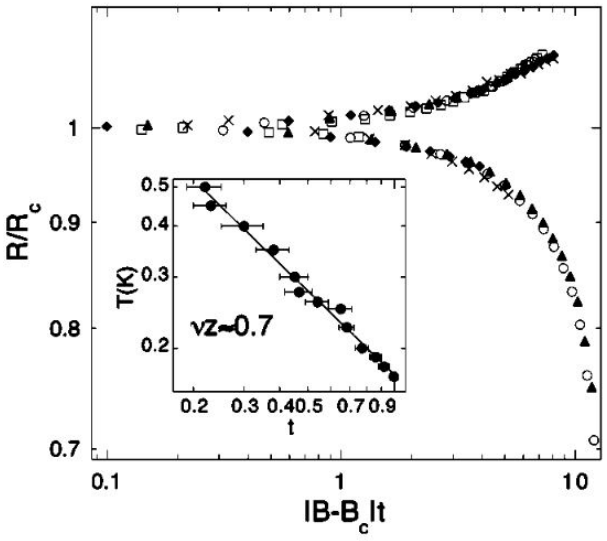

Figure 1.15: *Temperature scaling law analysis of the magnetic field tuned superconductor-insulator transition in Bi thin film extracted from [MCM$^+$99]. The critical exponent are found to be equal to νz=0.7.*

Transport measurements have also been performed on NbSi thin films [MKAP$^+$08]. The superconductor-insulator transition has been induced by varying the thickness from 12.5nm to 100nm. Critical exponents are found to be equal to $\nu = 0.4$ which is striking value that cannot be associated to one of the existing model. The superconductor-insulator transition can be driven by the composition of the film in Nb and Si [CCB$^+$14]. Crauste et al. studied the evolution of the critical thickness d_c below which the system becomes insulating for different composition of Nb and Si.They have shown that d_c is correlated with the bulk Tc and diverge when approaching the critical composition for which the superconductor-metal occurs in the bulk film.

In epitaxial NbN films, the Hall effect [CMX$^+$09] and the magnetoresistance [CCJ$^+$08, CMK$^+$12] have been studied. Magnetotransport results are consistent with the idea that Cooper pairs survive in the insulating state when applying a magnetic field. This is again in contradiction with magnetotransport measurements performed on InO [SEJ$^+$05] or in amorphous nanohoneycomb bismuth films [NHS$^+$09] where a huge peak of resistance is observed and interpreted as localized Cooper pairs in the insulating state. However, it is noticeable that the magnetoresistance peak in these two systems are not of the same order of magnitude as the magnetoresistance peak measured in NbN (see figure 1.16).

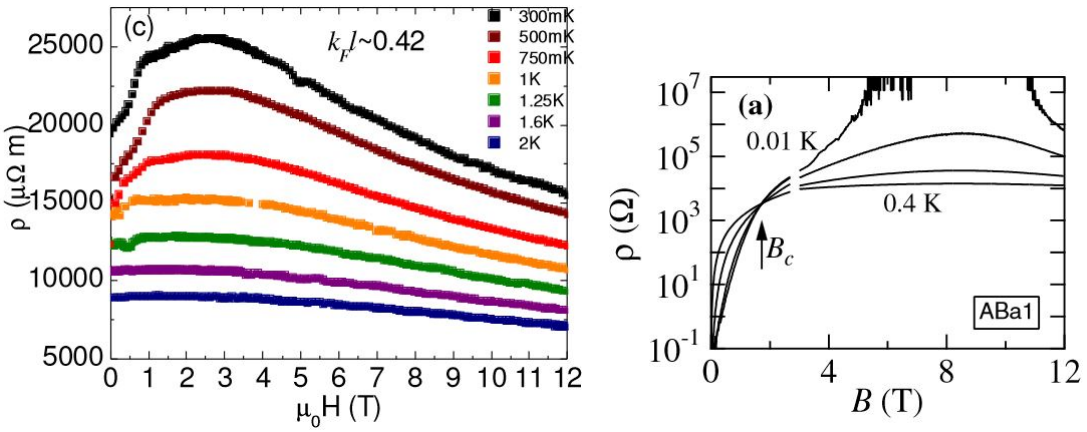

Figure 1.16: *Left: Magnetoresistance peak measured on epitaxial NbN film extracted from [CMK+12]. Right: Magnetoresistance peak measured on InO film extracted from [SEJ+05]. In NbN, the maximum resistance reaches is about 25000μΩ.m while in Ino it is more than $10^7\Omega$. This point highlights that the two materials have a completely different behavior under magnetic field.*

1.3.3 Other measurements

Recently, very interesting results have been obtained by microwave electrodynamics measurements on TiN thin film [CDB+13] which is used as the resonating element in a high-quality environment of NbTiN. A microwave signal from a vector network analyzer is fed to the sample through coaxial cables. The amplified forward power transmission S_{21} of the transmission line is recorded as a function of the temperature and the microwave frequency. More details on this experimental setup and the measurements technique are given in [CDB+13]. A highly disordered film ($k_F l \approx 0.8$) has been studied and the electrodynamic response of the superconductor has been described by a model which contains a disorder-dependent effective pair breaking parameter. For the weaker disordered film, the results are consistent with the scanning tunneling spectroscopy measurements obtained by Sacepe et al. However, close to the critical disorder, this model based on averaged properties is no more applicable due to the presence of superconducting inhomogeneities.

Microwave spectrometer can be used to get informations about the superconducting condensate in thin films. This experimental technique is described in [KOM08, SSD12]. InO thin films have been widely studied by Armitage et al. [CAJ+07, LKSA11, LPW+13]. In the first publication [CAJ+07], they have shown that the superconducting state has to be taken into account to describe the insulating state. More recently [LKSA11, LPW+13] studied the phase stiffness of InO film with a Tc close to 2.3K. The phase stiffness is the energy scale required to twist the phase of the superconducting order parameter, it is proportional to the superfluid density. The authors focused on the quantum phase transition and demonstrated that the transition without magnetic field, due to thermal fluctuations, corresponds to a 2D Kosterlitz-Thouless-Berezinskii transition type. Then, they have shown that a quantum phase transition in weakly disordered InO films occur for a magnetic field which is different of the field at which a crossing point is observed in the resistance versus magnetic field curves. It may suggest that all the scaling law analysis performed at this time have to be re-evaluated in light of these new results.

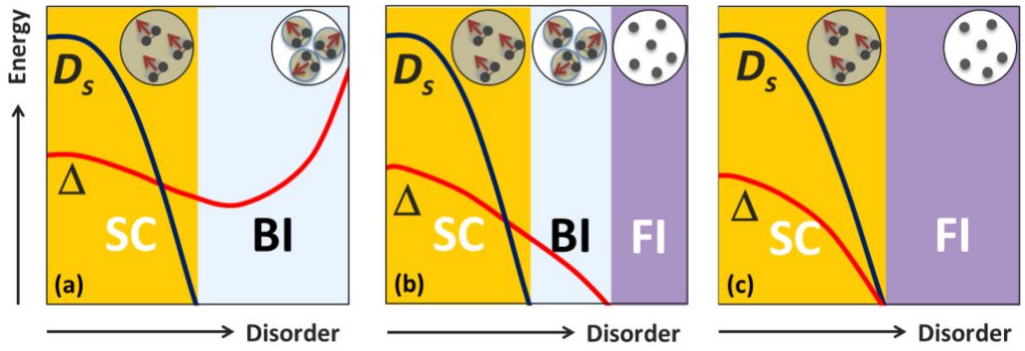

Figure 1.17: *Schematic representation of the three models used by [SGP+14] to described the superconductor-insulator transition in InO films. The effect of disorder on the characteristic energy scale of a superconductor are shown. The red line corresponds to the energy gap Δ and the black line to the superfluid stiffness D_S. The three scenario are the following: (a) transition between the superconductor state to the localized Cooper pairs insulator state (BI: Bose Insulator), (b) crossover from a localized Cooper pairs insulator to a Fermi insulator (FI) and (c) direct transition between the superconducting state and the Fermi insulator.*

Frydman et al. [SGP+14] also measured InO films by using terahertz optical spectroscopy and tunneling spectroscopy. To explain their results, they developed three models based on the interplay of BCS superconductivity, Anderson localization and Coulomb interactions. The three scenarios a), b), and c) are schematically represented in figure 1.17. In the first model (a), which ignores Coulomb interactions, the superconductor-insulator transition is described as a quantum phase transition leading to localized Cooper pair insulating state. In the second and third model, the Coulomb interactions are taken into account. The difference between the model (b) and (c) is based on the relation between the superconducting energy gap Δ and the superfluid phase stiffness D_S that leads to different conclusions. In scenario b), the insulating state is described as a crossover from a localized Cooper pairs insulator to a Fermi insulator of broken pairs. In scenario c), the transition is directly from a superconductor to a Fermi insulator, in better agreement with the results of their terahertz measurements. This work highlighted the importance of electron-electron interactions when increasing the disorder.

Finally, ac complex conductivity measurements on epitaxial NbN thin films have been performed by Raychaudhuri et al. [MKG+13] by using a broadband Corbino microwave spectrometer [SSD12]. Their results have shown that the superfluid stiffness depends on a temporal and spatial length scale for $T_c<T<T^*$ where T^* is the temperature until which the pseudogap state is observed. Moreover, the microwave measurements suggest that the superconducting transition is driven by phase fluctuations of the strongly inhomogeneous superconductivity.

1.4 Main results obtained during this thesis

Recently, scanning tunneling microscopy and spectroscopy experiments addressed the problem of the superconductor-insulator transition in NbN thin films deposited on MGo substrates [KDG$^+$13, CSK$^+$12, CKS$^+$11, MKC$^+$11a, CCK$^+$09]. NbN and MGo are alsmost lattice matched, so crystalline films are grown on MGo substrates. The film thickness in these studies is about 50nm and the transition is induced by tuning the disorder, namely by changing the Nb/N ratio and thus creating vacancies. A similar study has been done on TiN and InO films [SDC$^+$11, SCB$^+$10, SCB$^+$08]. TiN samples are elaborated by atomic layer chemical vapor deposition onto a Si/SiO_2 substrate. They are made of densely packed crystallites having a typical size of 4 to 6nm. InO thin films are elaborated by evaporation using an electron gun on a In_2O_3 target. The substrate used is also Si/SiO_2 and the films are also made of very small crystallites. The superconductor-insulator transition was induced by varying both the thickness of the films and the magnetic field applied perpendicularly to the sample. These various systems are very close to our NbN samples but lead to different interpretations. Thus, a study of the local properties of our NbN ultra-thin films could help to understand the microscopic processes occurring close to the superconductor-insulator transition.

The samples that were studied during this thesis were Niobium Nitride thin films deposited on a single crystalline sapphire substrate. They are elaborated *ex-situ* by our collaborators at the Karlsruhe Institute of Technology [SGB$^+$09] (see chapter 2). These NbN thin films are particularly interesting systems. Indeed, they are already used to fabricate single photon detectors [GOC$^+$01]. It has recently been demonstrated that the maximum quantum detection efficiency occurs for films thicknesses close to the superconductor-insulator transition [HRI$^+$10]. This aspect was also one of our motivations to study these systems. In order to achieve as realistic conditions as possible, we studied NbN films similar to the ones used to fabricate meanders for real photon detectors. As can be seen in figure 1.18 the resistivity of the films as a function of temperature follows a typical behavior of homogeneous systems : the superconducting transition is sharp, the Tc decreases continuously when decreasing the thickness and there is no re-entrance phenomenon; very similar to the Bi case, figure 1.2. However, very close to superconductor-insulator transition, there are slight deviations from this canonical behavior as detailed in chapter 4.

At the beginning of this thesis, some results were already obtained in our group on NbN thin films and were published later in an article [NCB$^+$13]. The results are presented in chapter 5 of this thesis. This study has enabled to show unconventional signatures in the tunneling conductance when approaching the superconductor-insulator transition from the superconducting side. Spatial inhomogeneities of superconductivity has been observed that affect the height of the coherence peaks and the width of the gap (see figure 1.19). Moreover, our study revealed that the gap develops on a strong "V-shape" spectral background. It constitutes the first direct STM/STS study of the vortex lattice in ultra-thin NbN measured in perpendicular magnetic field. It has been observed that vortices are moving during the scan and that their size is much bigger than what expected from the coherence length in NbN thin films. These were very interesting and promising results. However, the lowest temperature available was 2.3K with the M2 experimental setup, and that did not allow us to study samples with lower Tc i.e. closer to insulator transition. It was also not possible to measure the resistance of the sample or to apply a high magnetic field (>3T). Moreover, to perform further studies on NbN thin films, it was necessary to

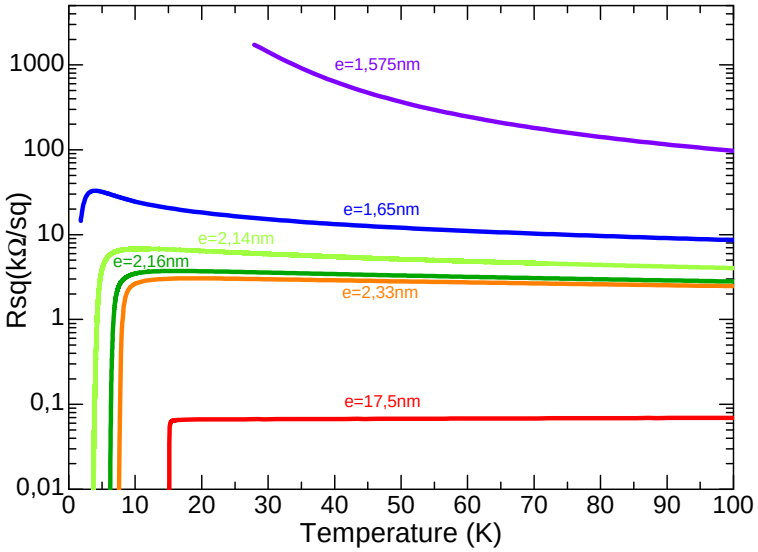

Figure 1.18: *Square resistance evolution as a function of temperature. The superconductor-insulator transition is induced by decreasing the film thickness. It has a behavior similar to what is typically observed in homogeneous thin films.*

have more stable experimental conditions in order to realize reproducible measurements on the same place of the sample.

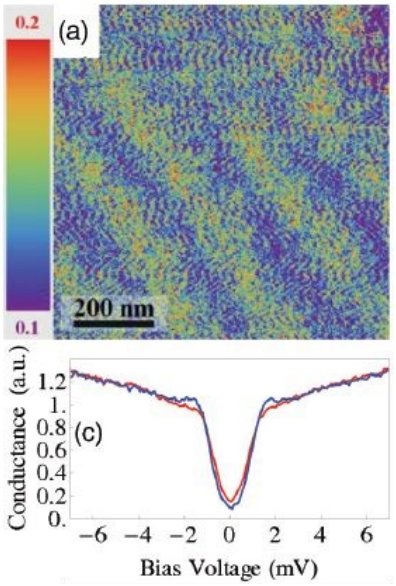

Figure 1.19: *Spatial inhomogeneities of the superconducting gap measured at 2K on a 2.16nm thick NbN sample by tunneling spectroscopy. The red spectra are representative of the red area of the conductance map and the blue one of the blue are of the conductance map. We observed that very small coherence peaks are present only in the blue regions.*

In this thesis, we have studied the transport properties of NbN thin films at low temperature and under high magnetic field. The results are presented in chapter 4. They enable us to show an evolution of the sample with time and thermal cycling. We have

also performed an analysis of the superconducting fluctuations regime above Tc using the Aslamasov-Larkin theory, and our results evidenced a 0D-2D crossover of the fluctuations when decreasing the film thickness. We have also investigated the properties of the quantum phase transition induced by magnetic field as a function of temperature and electrical field, and analyzed the critical exponents found by the scaling law analysis.

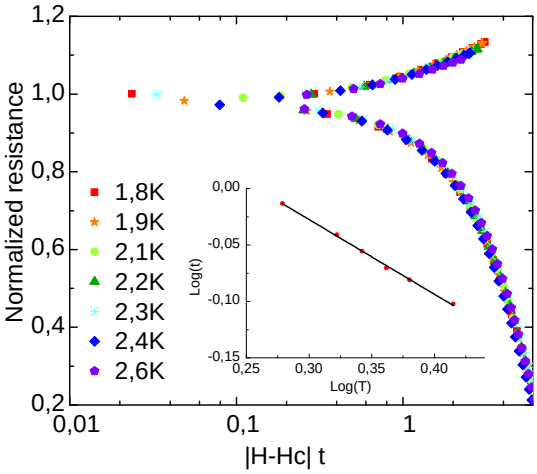

Figure 1.20: *Resistance per square as a function of the scaling variable |H-Hc|t for different temperatures at a magnetic field of 10.7T. We adjusted* $t = T^{1/\nu z}$ *in order to obtain the best collapse of the data. Inset: log-log plot of the parameter t versus temperature used to determine value of* νz.

Our magnetoresistance measurement highlighted the absence of a huge resistance peaks in high fields. It is in contrast with the behavior of InO and TiN films.

Taking into account the limitations of our STM M2 experimental setup, we performed further measurements on the M3 STM/STS which allowed us to reach lower temperatures and higher magnetic fields with a better stability. The aim was to study the evolution of superconducting properties of a film as close as possible to the insulating transition by means of tunneling microscopy and spectroscopy, by precisely controlling the temperature and the magnetic field, while always located on the same sample area. The lowest temperature accessible was 300mK and it allows us to obtain higher energy resolution. Moreover, we aimed to combine these STS experiments *in-situ* with electron transport measurements, in order to link macroscopic and microscopic scales.
Precisely, we would like to learn more about the origin of the "V-shape" background and how it affects the superconducting properties. In a second phase, we wanted to know how the macroscopic transport properties are related to the local data measured by tunneling spectroscopy. We have performed a complete study of the B-T phase diagram in a single sample area; the results are detailed in chapter 6. An example of the evolution of the conductance map as a function of temperature for zero magnetic field is shown in figure 1.21.

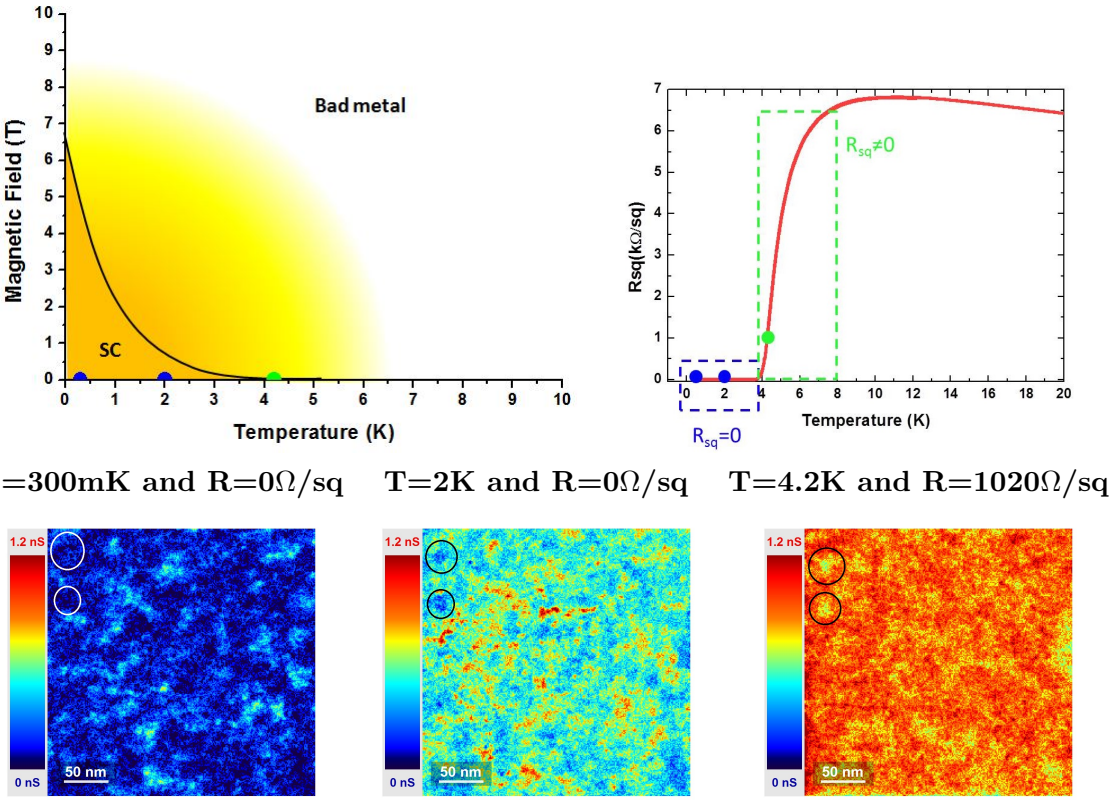

Figure 1.21: *On the first line is represented the phase diagram with the studied points as a function of temperature. In blue are the points where we measured zero resistance, the sample is in the superconducting state. In green are the point where the resistance reach a finite value. They are plotted on the resistance curve. On the second line are the conductance map measured over the same sample area with increasing the temperature.*

On the basis of our measurements we conclude that at T=0K and B=0T there is an emergent electronic granularity in NbN thin films. We observed a percolative transition toward the resistive state when increasing the temperature or the magnetic field. A strong V-shape background in the local density of states was identified as characteristic of the Altshuler-Aronov effect. It allowed us to say that electron-electron interactions become more important when approaching the insulating transition.

Finally, our last goal was to study a real single photon detector in operating mode by means of a scanning tunneling microscope combined to an atomic force microscope. At this stage of development, although several experimental difficulties prevented us from performing spectroscopic measurements, we have succeeded in the first steps: i) to elaborate a superconducting meander, and ii) to image it by Atomic Force Microscopy (see figure 1.22).

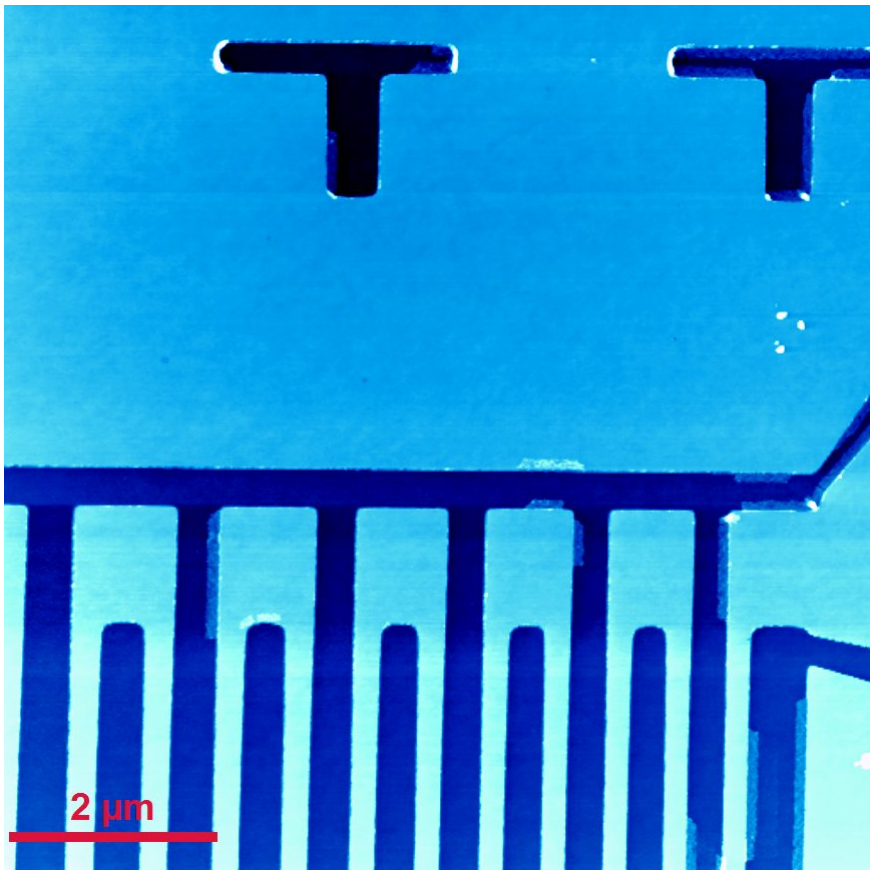

Figure 1.22: *AFM image of the NbN meander. In light blue are the area covered by NbN and in dark blue are the area where the NbN layer has been etched.*

Chapter 2

Sample fabrication process and characterization

Contents

2.1 Sample elaboration

The samples were elaborated in Germany by our collaborators at the KIT [1]. The same thin films of NbN are lithography processed and patterned in KIT to form single photon detectors [SGB+09].

2.1.1 Substrate

Al_2O_3 sapphire substrates which crystallographic structure is hexagonal were used. This substrate was chosen because it is a very good thermal conductor and an excellent electrical insulator. Indeed, for single photon detectors, based on a superconducting NbN meander, it is crucial to have an insulating substrate to avoid inverse proximity effects. High thermal conductivity is advantageous to rapidly relax the detector after photon count into its "wait" state, thus increasing the detector's counting rate. In order to study a system as close as possible to this device, we kept the same Al_2O_3 substrate. Besides, it provides a particular lattice mismatch between the substrate and the NbN layer due to the R- plane surface orientation (see figure 2.1). That determines among others the structural properties of the NbN films.
Substrates were chemically cleaned before depositing the NbN layer. The purpose of this process is not to obtain a reconstruction of the surface of sapphire but to remove impurities. Moreover, before depositing, substrates are annealed. This step enables the elimination of water molecules present on top of the substrate, thus avoiding the formation of Nb-O links at the NbN-Al_2O_3 interface.

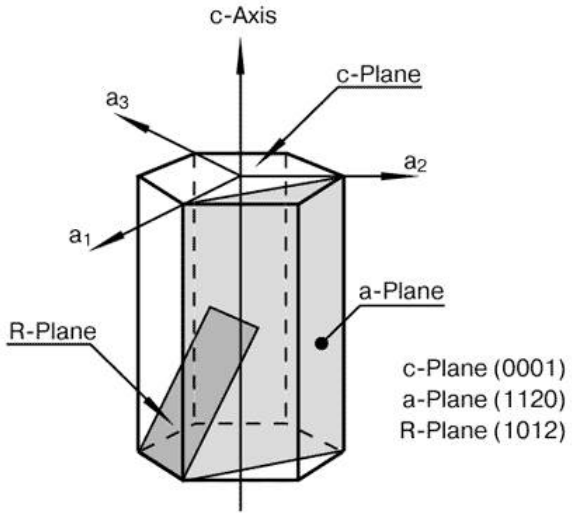

Figure 2.1: *Sapphire unit cell showing the possible orientation of the surface. The substrate used to deposit NbN films are R-plane oriented.*

2.1.2 Vacuum deposition

NbN thin films were grown *ex-situ* by DC reactive magnetron sputtering [KA00]. The apparatus used in the Karlsruhe Institute of Technology can be seen on figure 2.2. Before

1. Karlsruhe Institute of Technology - Konstantin Ilin

introducing the sample in the deposition chamber, the load-lock is pumped to 2.10^{-6}mbar. In the vacuum chamber, the pressure is typically around 1.10^{-7}mbar before deposition. In this fabrication process, a Niobium target (the cathode) is sputtered by ions coming from the plasma generated between the target and the sample holder. The sputtering take out the Niobium atoms from the target which will hit the substrate forming a thin film.

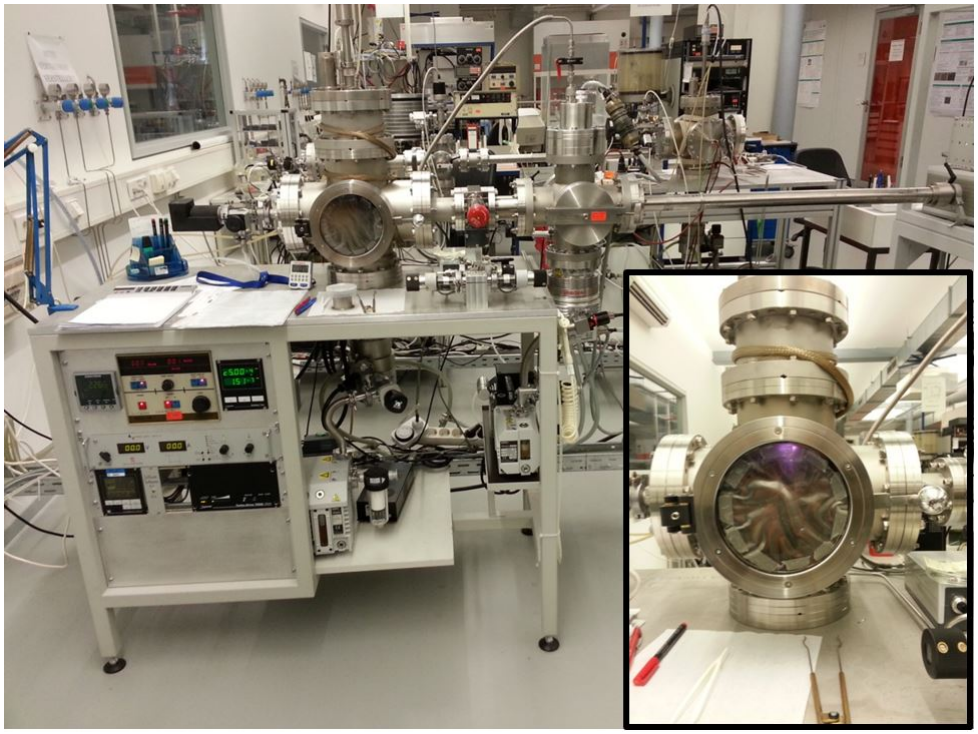

Figure 2.2: *Pictures of the UHV magnetron sputtering chamber used for the deposition of NbN thin films at the KIT. Insert: One can see the plasma formed in the chamber during the depositing (purple color corresponds to an Ar and* N_2 *plasma).*

2.1.3 Evaporating conditions

Before evaporation, pure Nb is sputtered (Ar plasma used with no N_2) in the chamber. As Nb is a getter material, it is very efficient to capture O_2 and other species that contaminate NbN during growth. The amount of evaporated Nb is optimized to allow efficient pumping during deposition. Then, the substrate is placed on top of the sample holder and heated up to 850°C. This is the temperature used during deposition. It is favourable for the epitaxial growth of the films while decreasing disorder. When the required temperature is reached, Ar and N_2 gases are introduced to form the plasma.
The exposure time of the substrates to the niobium target is calculated according to the desired thickness. The growth rate is typically around 0.17nm/sec.
The deposition process has been optimized with respect to the partial pressure of N_2 and the deposition rate in order to obtain as pure NbN as possible and reach the highest transition temperature for films with the smallest thickness.

2.1.4 Thin films thickness determination

The NbN thickness is determined from the exposure time of the substrates to the niobium target. Therefore, we need to calibrate precisely the deposition rate.

The thickness of thick films is measured by using a profilometer. The deposition rate can then be calculated from the exposure time assuming linear growth with time.

2.2 Sample characterization

2.2.1 Transmission Electron Microscopy measurements

The Transmission Electron Microscopy (MET) is an imaging technique based on an electron beam transmitted through a thin sample. Depending on the thickness and the electronic density of elements composing the sample, the electron beam will be more or less transmitted. Thus, the measure is sensitive to thickness variations and to the thin film composition.
In order to guarantee the transmission of electrons through the sample, it has to be thinned down to less than 100nm typically. Samples measured through their cross-section were made thinner using an ion gun. They were studied on a Jeol 2100 TEM at IMPMC [2] which achieve a 0.2nm resolution with an electron beam accelerated to 200keV and on a STEM-HAADF (Scanning Transmission Electron Microscope - High Angle Annular Dark Field imaging) at LPN [3]. Diffraction images can also be formed with this machine.

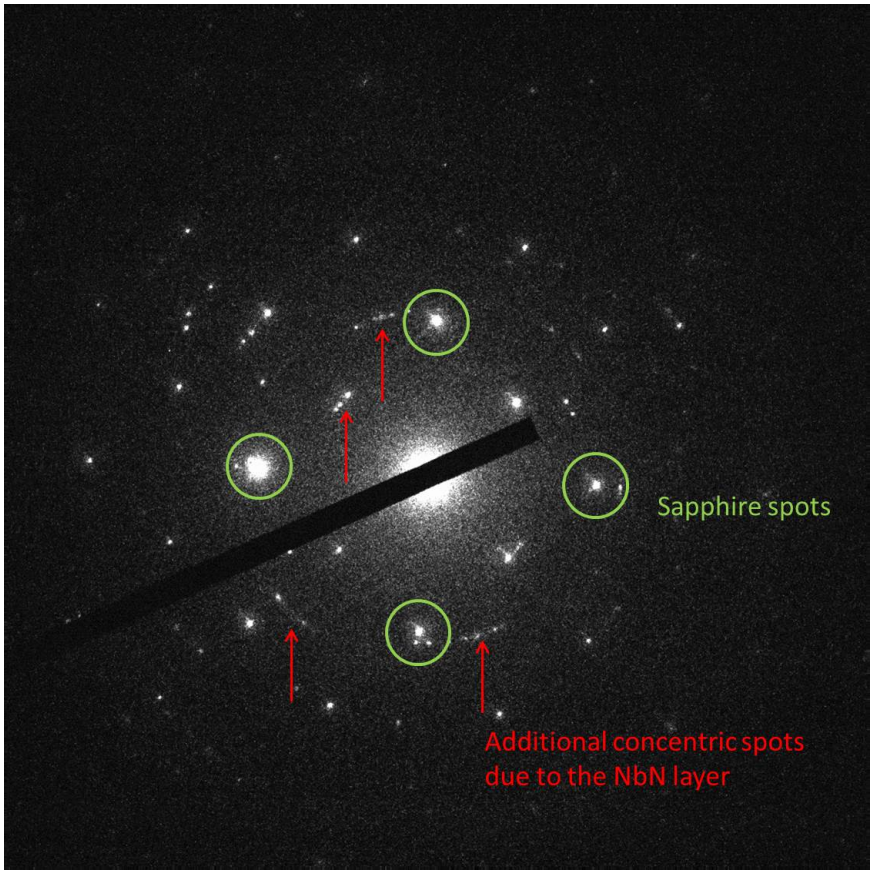

Figure 2.3: *Electronic diffraction pattern obtained by TEM on a 2.33nm thick NbN sample. Concentric circles (red arrows) are visible in addition to the spots due to the sapphire substrate (green circles). These features are characteristic of polycrystalline samples.*

2. Institut de Minéralogie et de Physique des Milieux Condensés - Dominique Demaille(INSP)
3. Laboratoire de Photonique et Nanostructure - Ludovic Largeau

Electron diffraction is used to characterize and identify crystalline phases and determine their crystallographic structures, orientation and defects. In the reciprocal space, a spot for each family of planes (hkl) of a crystal are visible.

2.2.2 TEM Results

Diffraction patterns (figure 2.3) show spots in concentric circles designed by the red arrow on the figure, in addition to those formed by the substrate's atoms designed by the green circles on the figure. It is characteristic of polycrystalline samples.
On TEM images (figure 2.4), we clearly see that the films are made of nanocrystals whose dimensions do not exceed few nanometers for the 2.33nm thick sample. Crystallites have different orientations due to the underlying Al_2O_3 substrate. We determined the sapphire

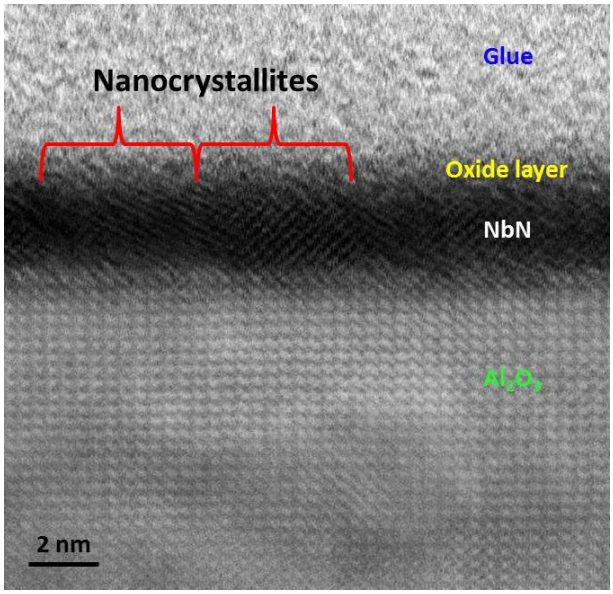

Figure 2.4: *TEM image done on a 2.33nm thick NbN sample in cross section view. Nanocrystallites of few nanometers are visible. The oxide layer has been detected by a chemical analysis but is too thin to be observed.*

zone axis: [221] as the NbN layer zone axis: [111]. The latter formed a 43.7 degree angle relative to the substrate in most of the observed area. At the KIT, they determined that the films with an optimal Nb and N composition have a face centered cubic structure with a lattice constant of 0.44nm. Otherwise, nanocrystals and their various orientations relative to the underlying substrate of Al_2O_3 give a grainy aspect to NbN films. We observed this effect thereafter in the scanning tunneling microscope images.
To perform a chemical analysis the STEM-HAADF (Scanning Transmission Electron Microscopy - High Angle Annular Dark Field) has been used. Indeed, this apparatus enables to perform energy dispersive X-ray analysis (EDX) which is a technique for chemical characterization of a sample. It relies on the interaction between a X-ray source and the sample. This measurement highlighted the presence of an oxide layer on top of NbN films (see figure 2.6). The oxide layer appears within a few minutes after exposing the film to air for the first time. On newly prepared samples, its thickness varies from 0.5 to 1nm. Further oxidation proceeds much slower. The oxide layer has been detected during STM measurements. It is clearly an insulating layer since the tip penetrates into it before detecting the tunneling current. On the time scales of several months the sample gets

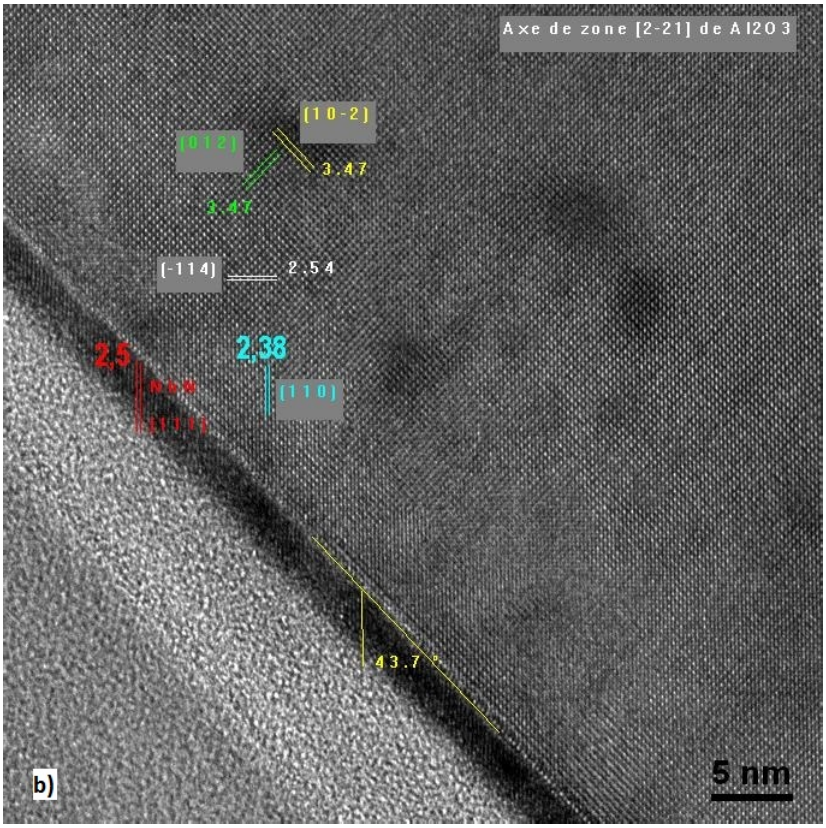

Figure 2.5: *TEM image done on a 2.33nm thick NbN sample in cross section view. The zone axis of the NbN layer and the sapphire substrate and the angle formed between the two have been determined from this image.*

"older": The tunneling barrier formed by oxided NbN at the sample surface becomes too thick to allow for a tunneling current to circulate through it between a STM tip apex and the underlying NbN. This in turn forbids reliable STM/STS experiments. The analysis of the topographic images showed that the tip is touching the surface during the scan.

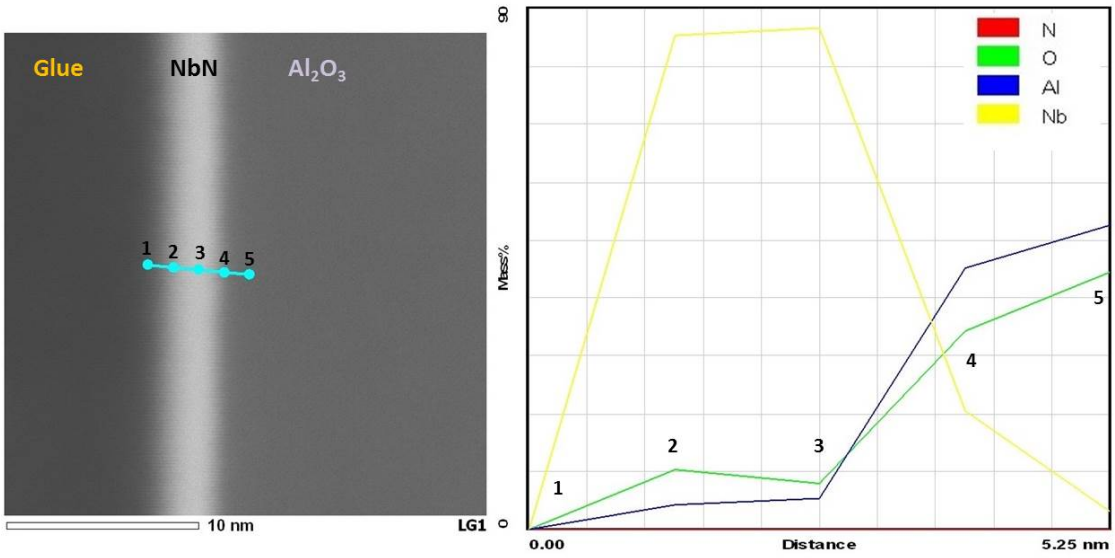

Figure 2.6: *Chemical composition of a NbN sample along its cross section. The identified elements are O, Al and Nb. The N curve is constant at zero because it can not be detected by the analyzer.*

2.3 Ex-situ transport measurements

2.3.1 Preliminary measurements after deposition

At the Karlsruhe Institute of Technology, freshly prepared NbN samples are contacted by a standard four terminal method using Al-bonding. Then, the resistance versus temperature characteristics are measured to evaluate the superconducting critical temperature directly after deposition.
Measurements are done in a helium cryostat at temperatures ranging from 300K down to 4K (see figure 2.7).
To evaluate the properties of the films, the sheet resistance and the critical temperature of the samples are more relevant parameters than the thickness. Indeed, the resistance as a function of temperature can be measured precisely. However, the thickness is calculated from the time exposure of the substrate to the Niobium target. This parameter is not perfectly controlled.

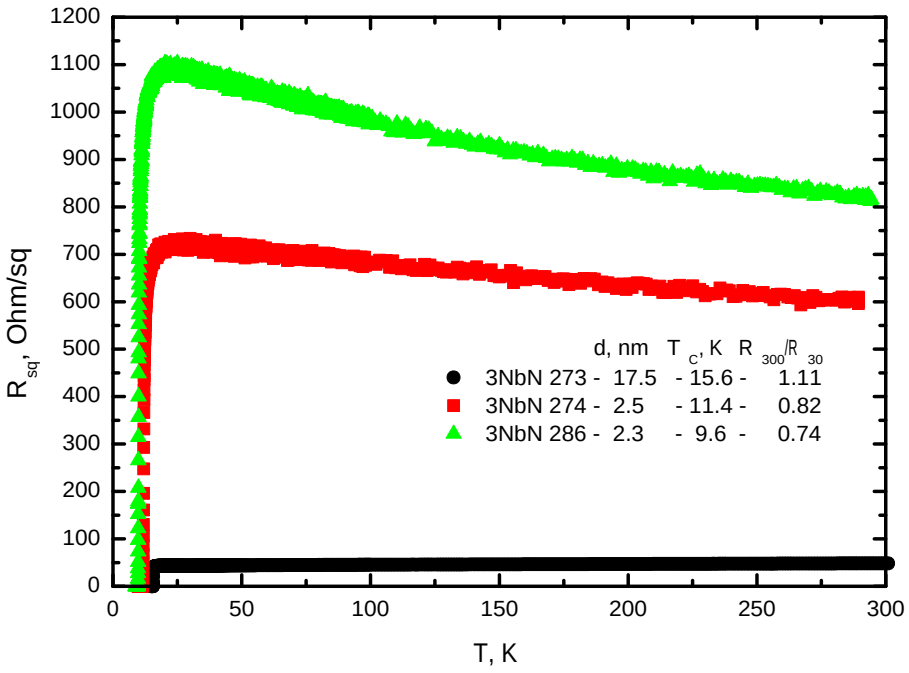

Figure 2.7: *Curves showing the resistance evolution as a function of temperature measured for several NbN films thicknesses directly after deposition at the KIT.*

2.3.2 Detailed magneto-transport experiments

A part of the transport measurements have been done later after sample fabrication, at LPEM [4] and IMPMC [5].
Transport measurements were performed by means of a standard four probes technique with Al-bonding in a Quantum Design PPMS (Physical Property Measurement System). More details are given in the following chapter. The results are similar to those obtained directly after NbN deposition.

2.3.3 Resistance evolution as a function of film thickness

We have measured the evolution of the resistance as a function of temperature for several NbN films. Typically, we observed a critical temperature decrease and a resistance increase when the film thickness is reduced. The superconductivity reentrance phenomenon is not observed in our NbN samples, as can be seen on figure 2.8.

4. Laboratoire de Physique et d'Etude des Matériaux - Brigitte Leridon
5. Institut de Minéralogie et de Physique des Milieux Condensés - Yannick Klein

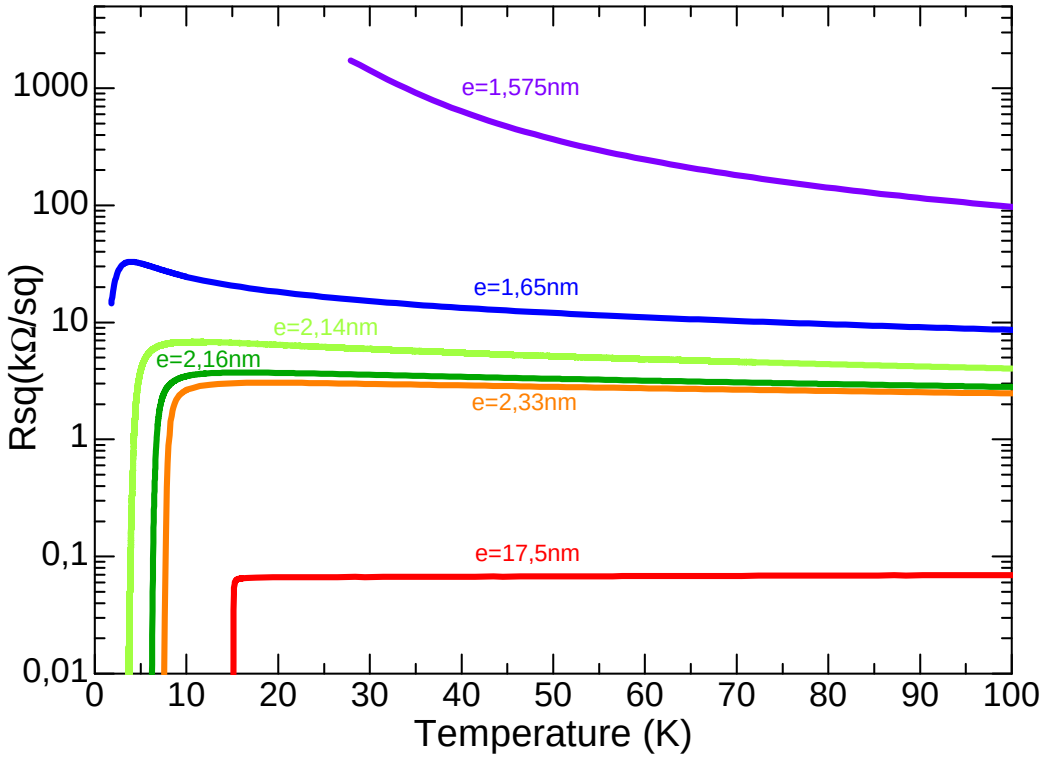

Figure 2.8: *Curves showing the resistance evolution as a function of temperature measured for several NbN thicknesses. We observed a resistance increase and a critical temperature decrease as the thickness is reduced.*

2.3.4 Resistance evolution as a function of time

It is noticeable that the electronic properties of NbN samples evolve in time. We observed that the superconducting critical temperature decreases and the resistance increases with time. This phenomenon is amplified by thermal cycling imposed to the sample (figure 2.9).
Thus, it is very important to know precisely the critical temperature of samples.

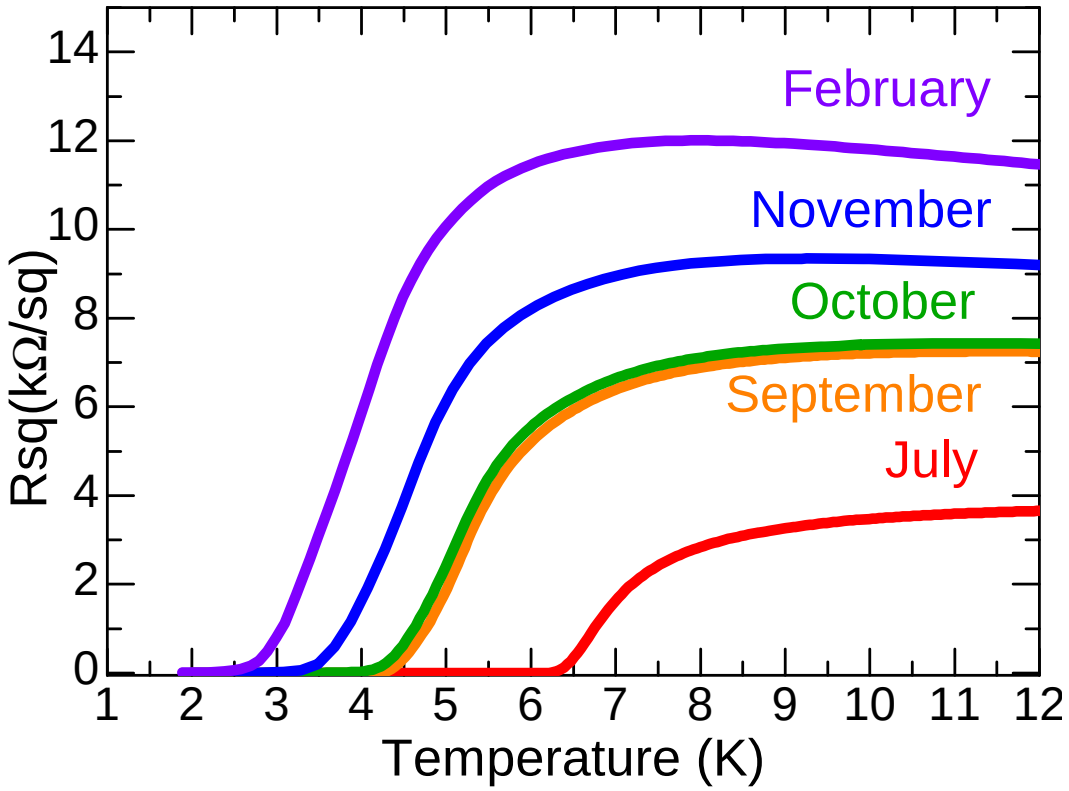

Figure 2.9: *Resistance evolution of a 2.16nm thick sample as a function of temperature at different time intervals. The superconducting transition temperature decreases and resistance increases as the sample is thermally cycled and gets older.*

Chapter 3

Experimental setups

Contents

Scanning Tunneling Microscope (STM) was invented in the 80s by two physicists: G. Binnig and H. Rorher. They got the Nobel Prize a few years later. This invention paved the way for new possibilities in tunneling spectroscopy. Indeed, it provides a tool to measure the tunnel conductance at atomic scales. No other experimental setups are able to reach such precision.
The phenomenon behind STM is the quantum tunneling of electrons. When two electrodes are separated by a thin potential barrier such as an oxide or vacuum, electrons have a non-zero probability to tunnel through the barrier. This phenomenon, forbidden in classical physics is allowed in quantum mechanics. In scanning tunneling microscopy, the first electrode is the tip and the second one is the sample.
Before describing in more details the scanning tunneling microscope operating mode, the quantum phenomenon of tunneling will be developed.

3.1 Electron tunneling theory

The basic theory of tunneling has been introduced by the work of Bardeen [Bar61]. Because the particle wave function is not null in the barrier but decreases exponentially, the particle has a non-zero probability to tunnel through the barrier. The Bardeen model is useful to express the tunnel transmission of simple particles and quasiparticles. The two electrodes composing the tunnel junction are considered as independent systems in this approach. The tunnel current calculation as a function of the sample and tip density of states has been first developed for planar junctions. The measured current is thus averaged over the junction surface which is of the order of mm^2 to $\mu\mathrm{m}^2$ for the smallest.
The particles transfer through the barrier is described by the Hamiltonian:

$$H = H_L + H_R + H_T \tag{3.1}$$

H_L and H_R are the Hamiltonians corresponding to the left and right electrodes. H_T is the transfer Hamiltonian which is responsible for the transfer of electrons across the junction. Energy and eigenstates of H_L et H_R are respectively E_μ, Ψ_μ and E_ν, Ψ_ν.
The tunneling current could be expressed as:

$$I = \frac{2\pi e}{\hbar} \sum_{\mu\ \nu} f(E_\mu)[1 - f(E_\nu + eV)]\ |M_{\mu\nu}|^2\ \delta(E_\mu - E_\nu) \tag{3.2}$$

With $f(E)$ the Fermi function and V the voltage drop across the junction. $M_{\mu\nu}$ is the matrix element of H_T which couples eigenstates Ψ_μ of the tip and Ψ_ν of the surface.
Bardeen expressed this matrix element as follows:

$$M_{\mu\nu} = -\frac{\hbar^2}{2m} \int_{S_0} d\vec{S}[\Psi_\mu^* \vec{\nabla} \Psi_\nu - \Psi_\nu \vec{\nabla} \Psi_\mu^*] \tag{3.3}$$

With S_0 the surface of the two electrodes.

In order to understand tunneling in STM, the previous equation has to be reevaluated in terms of real space wave functions.
Tersoff and Hamann [TH83] performed the first calculation of the tunneling matrix element for the STM junctions. They took a simplified geometry for the electrodes.
Electrons of the tip in vacuum are described by an evanescent wave coming from the apex supposed to be a sphere of radius R and center r_0:

$$\psi_\mu(r) = A_\mu \frac{e^{-\kappa|r - r_0|}}{|r - r_0|} \tag{3.4}$$

With

$$\kappa = \sqrt{2\mathrm{m}(\phi - \mathrm{E})/\hbar^2}$$

the inverse range of the evanescent wave of an electron which have an energy E in vacuum. ϕ is the work function. A_ν is a renormalization constant.
To describe electronic states at the vicinity of the surface, Tersoff et Hamann considered a periodic crystal. The wave function ψ_ν of the sample in a given point r of the tunnel barrier is thus a Bloch wave in the (xy) plane. This Bloch wave is weighted by an exponentially decreasing component along z:

$$\psi_\nu(r) = \psi_{k_{\mathrm{ll}},E} = \sum_G C_{k_{\mathrm{ll}},G}\ e^{i(k_{\mathrm{ll}}+G)x}\ e^{-\alpha_{\nu,G}.z} \tag{3.5}$$

With $\alpha_{\nu,\mathrm{G}} = \sqrt{|\mathrm{k}_{\mathrm{ll}} + \mathrm{G}|^2 + \mathrm{K}_\nu^2}$ and $\mathrm{K}_\nu = \sqrt{2\mathrm{m}(\phi - \mathrm{E})/\hbar^2}$. Here, k_{ll} is the wave vector component parallel to the surface. G is a wave vector of the reciprocal 2D lattice. $\mathrm{C}_{\mathrm{k}_{\mathrm{ll}},\mathrm{G}}$ are the coefficients of the Fourier series development. Moreover, by supposing that tunneling voltages are small with respect to the workfunction and states are close to the Fermi surface, we obtain:

$$K_\mu = K_\nu = \frac{\sqrt{2m\phi}}{\hbar} \tag{3.6}$$

It assumes for simplicity that the work function is the same for the tip and the sample $\phi_\mu = \phi_\nu$.
By replacing (3.4) and (3.5) in (3.3):

$$M_{\mu\nu} = -\frac{2\pi\hbar^2}{m}\ A_\mu\ \psi_\nu(r_0) \tag{3.7}$$

Thus tunneling current can be written as:

$$I = \frac{(2\pi\hbar)^3}{m} \sum_{\nu\mu} A_\mu^2\ |\psi_\nu(r_0)|^2\ (f(E_\nu) - f(E_\mu))\ \delta(E_\nu - E_\mu + eV) \tag{3.8}$$

We supposed A_μ to be constant, and by expressing the density of states in terms of wave functions, it comes:

$$I \propto \int dE\ \rho_s(r_0, E)\ \rho_p(E - eV)\ (f(E - eV) - f(E)) \tag{3.9}$$

Where $\rho_\mathrm{s}(\mathrm{r}_0, \mathrm{E}) = \sum_\nu |\psi_\nu(\mathrm{r}_0)|^2\ \delta(\mathrm{E} - \mathrm{E}_\nu)$ is the local density of states of the sample at the position of the tip apex which could be calculated from the formula (3.5).
The tunnel current expression can be generalized to:

$$I = \frac{e}{\hbar} \int_{-\infty}^{+\infty} dE\ \rho_s(r_0, E)\ \rho_p(E - eV)\ T(E, V, z)\ (f(E - eV) - f(E)) \tag{3.10}$$

With T(E,V,z) being the transmission factor of the tunnel barrier. This term contains the exponential dependence. As it is a function of z, it shows the deformation of the barrier for high voltage applied to the junction $\mathrm{V} \sim \phi/\mathrm{e}$. In STM, the voltage is always weak (less than typically 0.1V) compared to the tunnel barrier height ϕ and the Fermi energy $\mathrm{E_F}$. Thus, in our experiments, we could do the following approximation: $\mathrm{T(E, V, z)} \approx \mathrm{T(E_F, z)}$. Then:

$$I = \frac{eT(E_F, z)}{\hbar} \int_{-\infty}^{+\infty} dE\ \rho_s(r_0, E)\ \rho_p(E - eV)\ (f(E - eV) - f(E)) \tag{3.11}$$

Depending on the sign of the voltage, the tunneling current probes empty states (V>0) or filled states (V<0). The first experimental verification of the tunneling effect has been done by Giaver [Gia60] in the planar junction formed by a normal metal and a superconductor isolated by a thin oxide layer.

3.2 Tunneling spectroscopy of a superconductor

In the case of superconductors, when T<Tc, electrons couple in Cooper pairs which form a quantum condensate. This condensate is coherent on a macroscopic scale and is described by a global wavefunction. Condensation of Cooper pairs gives rise to a gap Δ in the excitation spectra. The conventional superconductors are described by the BCS theory in which the density of excitations is given by:

$$N_s(E) = N_s(0)\frac{E}{\sqrt{E^2-\Delta^2}} \quad for \quad |(E)| > \Delta, \quad or \quad 0 \quad otherwise. \tag{3.12}$$

Thus, tunneling spectroscopy gives information about the spatial and energetic repartition of the electronic excitations. At T=0K, there are no elementary excitations (quasiparticles) with energies below Δ. It means that the current is zero when the voltage between the tip and the sample is lower than the gap divided by e but is not null for higher voltages. The tunnel junction between a normal metal tip and a superconducting sample is depicted on figure 3.1.

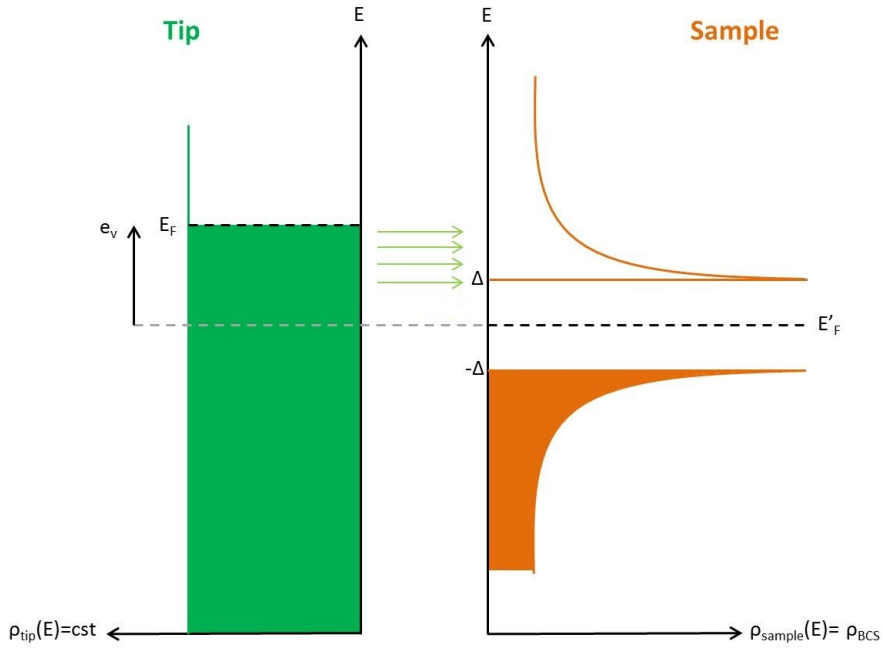

Figure 3.1: *Tunneling spectroscopy with a normal metal tip on a superconducting sample. On the left is the density of state of the tip (green) as a function of energy. On the right is the density of state of the sample (orange) as a function of energy. The occupied states are represented in plain color.*

3.3 Experimental aspects of STM

From the expression above, it is seen that the tunneling current I_T exponentially depends on the tip-sample distance d. It is a key point to obtain a vertical resolution, on the z axis of the tip, of about a picometer:

$$I_T \sim e^{-2\kappa d} \tag{3.13}$$

With

$$\kappa = \sqrt{\frac{2m\Phi}{\hbar^2}}$$

In metals, the work function Φ is typically of 4eV. Thus, the tunnel current decreases by a factor 3 when increasing the tip-sample distance of 1Å.
The lateral resolution essentially depends on the wave functions and the tip-sample distance. Thus, STM provides an opportunity to obtain images in real space at atomic scale.
The tunneling regime is defined by three independents parameters:

- Distance between the two electrodes d (typically 5 to 10Å).
- Tunneling current I_T ((typically 10-1000nA)).
- Tunneling bias V_T (corresponding to the spectral window of interest, typically 0-100mV).

For stability reason and not to heat the sample, I_T and V_T are chosen in order to have tunnel resistance $R_T = V_T/I_T$ of 10MΩ to 1GΩ.

3.3.1 Topographic mode

The scanning tunneling microscope enables to collect topographic and spectroscopic data locally. There are two modes to reveal the topography of a surface (see figure 3.2).

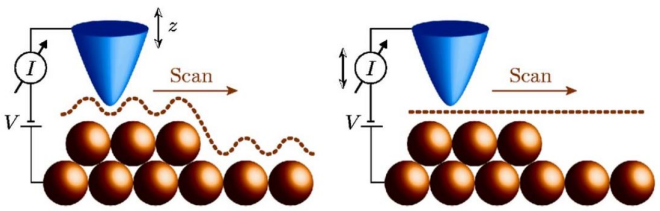

Figure 3.2: *Topographic STM modes. On the left: constant current imaging, distance z is adjusted to maintain the current constant. On the right: constant height imaging, the current I is changing.*

Constant current imaging

The constant current mode is the most often used in STM. Tunneling current is maintained constant by adjusting the vertical position of the tip during the scan. A feedback loop is used to control the distance d.
If the density of states is known as homogeneous on the studied area, then the profile corresponds to a constant tip-sample distance.
The vertical tip position z is recorded as a function of lateral coordinates (x,y). It is encoded in color or grey scale to form artificial maps called "topographic image".
The scan speed is limited by the bandwidth of the feedback loop which is typically of the order of the kiloHertz.

Constant height imaging

When using this imaging mode, the tip which scans the sample is maintained at a constant height. Thus, the feedback loop is open. Variations in the tunneling current are due to variations of the sample density of states.
Fluctuations of the current as a function of the tip position represents the surface topography, provided spatially constant state density.
This imaging mode permits to increase the scan speed, since it does not require the feedback loop to function. However, its utilisation is limited to surfaces with a roughness less than few Angströms, namely the tip-surface distance. Indeed, high protrusions could generate collisions between the tip and the sample surface.

3.3.2 Spectroscopic mode

By varying the bias voltage while maintaining the tip fixed above a given sample location, one can have a direct access to the electronic density of states.
When applying a positive voltage on the sample, electrons tunnels to allowed empty states of the sample. Conversely, when applying a negative voltage, electrons tunnels from occupied states of the sample. It can be seen on the figure 3.1.
dI/dV(V) spectra can be obtained from a numerical derivative of acquired I(V) curves or by using a lock-in amplification technique. In both cases, tunnel conductance is a local measure of the sample density of states. Measuring it in each point of the surface permits to construct a conductance map spatially associated to the topographic map.
In the experimental setup M3, the lowest temperature available is 300mK. However, the duration of one temperature cycle last less than 40h. It is thus essential to determine the duration of the acquisition before starting the measurements. In table 3.1 are the typical parameters of the measurements that were used to acquire the conductance maps and the topography on the experimental setup M3. The topographic measurements last about one hour and the spectroscopic measurements last about 19 hours. Thus, the total acquisition time for the topography/spectroscopy data simultaneously is 20 hours.

The scanning tunneling microscopy is a very sensitive tool and mechanical noises can perturb the measurements. The electronics system can also add some noise during the acquisition of the data. An automatic filtering can be used to remove these noises effects. During this thesis, the amplitude of the noise has been reduced by using a Gaussian filtering. Then, a Median filtering has been applied to the conductance maps to remove the spectra that were completely saturated. This filter compares the neighbouring values and changes it only if there is a big difference. It corresponds to only few spectra in the conductance map.

Topographic parameters	
Scan size	300nm x 300nm
Pixel	512 x 512
Scan speed	30nm/s
It	150pA
Vt	500mV
Spectroscopic parameters	
Grid size	256 x 256
Points/spectra	512
Energy range	[-6mV;+6mV]
Acquisition time	2ms/pts
Is	250pA
Vs	-50mV

Table 3.1: *Typical example of the measurement procedure that was used to acquire the conductance map and its corresponding topography. The total acquisition time for the topography and spectroscopy data simultaneously last about 20 hours.*

3.3.3 Piezoelectric effect

In scanning tunneling microscope, piezoelectric compounds are needed to realize very short displacements of the tip in the three space directions and thus visualize the atoms on a surface. The piezoelectric effect is the property of certain crystals to generate charges when stressed. This effect is due to the intrinsic polarization of the crystalline unit cell, and more generally to a non-centro-symmetric charge distribution (see figure 3.3).
When a crystalline cell with a non uniform charge distribution is mechanically deformed, the geometric centers of positive and negative charges move by a different amount resulting in an electric polarization. Conversely, the application of an electrical field results in different motions of the charges geometric centers in the cell, that finally induces a macroscopic deformation of the material, either shear or longitudinal.
In the STM, piezoelectric tubes with three electrodes are used (see figure 3.3). The first electrode is used for the vertical displacements along the z axis. The two others pairs of electrodes are used for the scanning movement in the (x,y) plane.

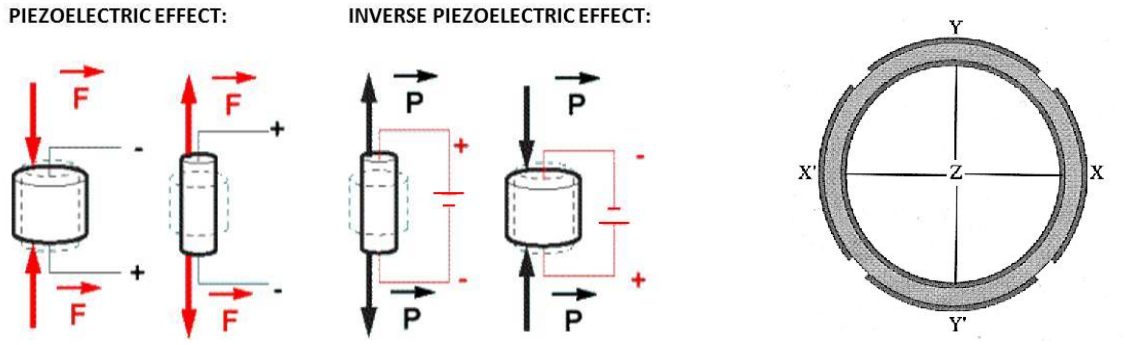

Figure 3.3: *Left: Schematic view of the piezoelectric effect. When applying a mechanical stress to the tube, it generates an electric polarization. When applying an electrical field, namely a voltage to the tube, a macroscopic deformation is induced. Right: Piezoelectric tube with 3 electrodes (x,y,z) (top view).*

3.3.4 Vibration isolations

Atomic resolution and stable spectroscopy can be obtained only if the system is well isolated from external mechanical vibrations. For all microscopes used during this thesis, two solutions were implemented.
First, STM heads are made as small and as light as possible, in order to increase their mechanical resonant frequency. The heads are isolated from the environment by a spring-mass low-pass filters. In our cases 3 STMs used in this work were made of Titanium and ceramics.
The second isolation stage consist of pneumatic anti-vibrational dampers, alimented by compressed air. The dampers (3 or 4) support all the system including the STM, chambers, pumps and a part of electronics. It enables to effectively isolate the microscope from environment mechanical perturbations.

3.4 Experimental setup M2

Three scanning tunneling microscopes are available in the team (called M2, M3 and LangevinSTM). The oldest, M2, has been elaborated in years 1995-2002. The NbN thin films study began on this microscope.

3.4.1 Specifications

General view of the microscope M2

The system is presented in figure 3.4. It is composed of a main ultra-high-vacuum chamber holding STM, a cryostat equipped with a superconducting magnet, a load-lock chamber, pumps and electronics. The load-lock is used to introduce samples and tips in the microscope chamber. A pumping system composed of a primary and a turbo pump permits to reach a pressure of about 10^{-7}mbar before transferring. A magnetic transfer manipulator is used; at its end there is a sample/tip holder stage which can contain 8 samples or tips. In the STM chamber, the base pressure is of the order of 10^{-9}mbar when working at 300K. To reach this vacuum, an ionic pump is used.

STM head

The M2 microscope (see figure 3.4) integrates two piezoelectric ceramics which do different jobs (designed and made by D. Roditchev on the basis of Rener's STM design). The internal tube serves to scan the surface (x,y) and to control the tip height (z). The external tube activates the inertial motor which is used for approaching the sample towards the tip.

Cryogenic system

The cryostat (see figure 3.4) is placed below the STM chamber. It is equipped with a "cold finger" - a vertical tube connected to the STM chamber and closed at its lower end. The vacuum inside the "cold finger" is obtained by pumping through the STM. The microscope goes down into a cold finger thanks to a pulley system. To thermalize the STM head suspended at the end of a cable, it is necessary to introduce exchange He gas in the chamber. Typically, the He pressure is 10^{-3}mbar. Cryopumping insures a clean environment. In this way, a temperature of 4.2K is reached. By pumping on the Helium bath of the cryostat, a limit temperature of 2.1K can be reached. Thanks to the pulley, the STM head position inside cold finger can be changed. It enables to vary the temperature of the sample and study the temperature dependence of the superconducting properties from 2K to 300K.

Electronics and control

In order to convert a low tunnel current (between 10pA and 1nA) into a measurable voltage, a pre-amplifier and current-voltage converter are used. The voltage value is proportional to the current and is thus directly compared to the current value ordered by the user. In the topographic mode, the tip-sample distance is adjusted to maintain the current constant, through the feedback loop. The system is controlled with a computer which interface is home-made (W. Sacks and D. Roditchev).

3.4.2 M2 makeover

During this work, some modifications have been done to improve the performance of the M2 experimental setup (figure 3.4). First of all, the superconducting magnet has been replaced. The new one is smaller and can generate a magnetic field up to 5T. The size difference is very important because it accelerates the cooling down process. Moreover, the thermal insulating screens have been replaced. These two operations have increased the cryostat autonomy at low temperatures.
Then, the piezoelectric elements which were used have been replaced and the *in-situ* cabling renewed. Furthermore, modifications in the current pre-amplifier electronics have permitted to reduce the noise level.
The wobble-stick has been replaced in order to facilitate the manipulation of samples and tips in vacuum. Lots of modifications followed this one to adapt the entire system. Thereby, sample and tip holders have been also redesigned to fit this new manipulator. The sample and tip staircase storage have been modified as well as the load-lock manipulator to accept the new holders.
Finally, the STM head has also been adapted to support the new sample holders.

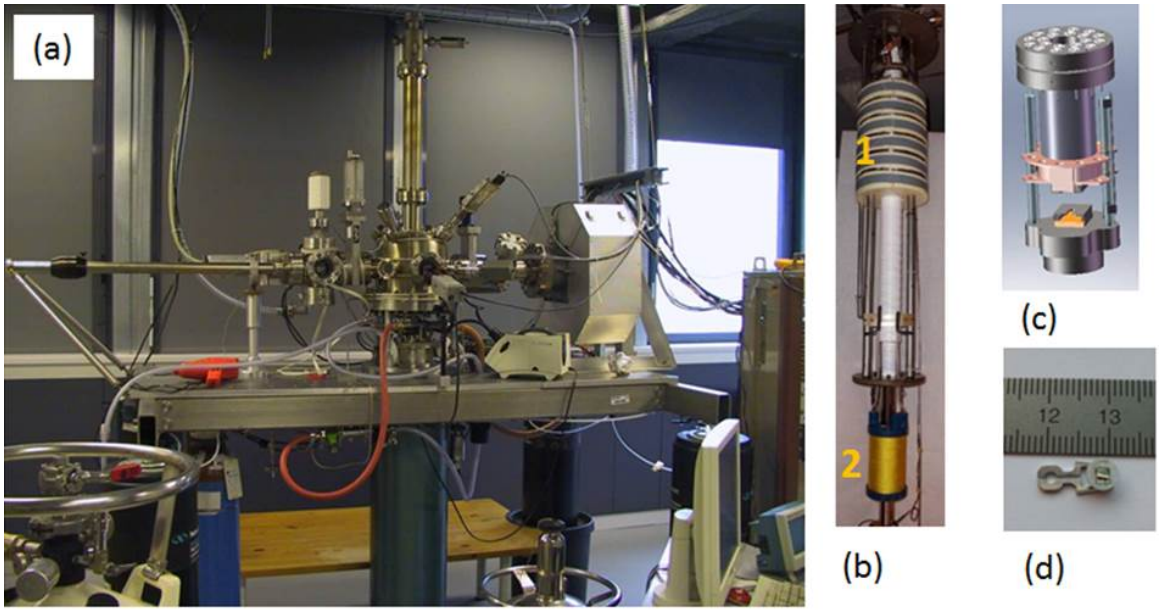

Figure 3.4: *(a) General view of the M2 experimental setup. (b) Cryogenic insert of the* ^{4}He *cryostat. In (1) are the new cryogenic screens and in (2) is the new superconducting magnet. (c) Modified STM head. (d) New sample holder with a* $NbSe_2$ *sample.*

3.4.3 Operating tests and system limitations

The second step consisted in the testing of the renewed system. Graphite is particularly suited to this process. Indeed, atomic resolution is easily obtained and permits to check and calibrate the piezoelectric displacements by counting the atoms in a given image size. Moreover, this test could be done at room temperature. As can be seen in figure 3.5, atomic resolution was obtained on graphite. Then, to check the spectroscopic mode and

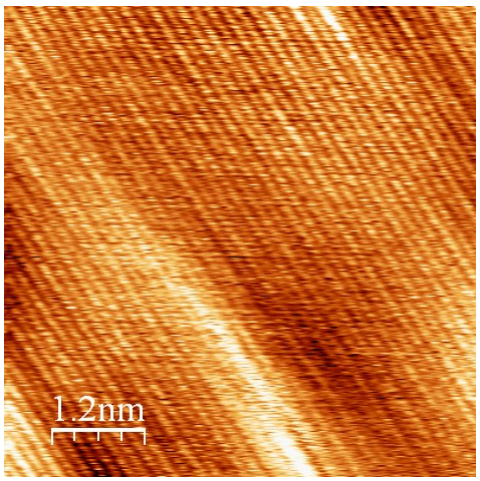

Figure 3.5: *Atomic resolution obtained on graphite during operating tests of the experimental setup M2.*

perform large scale piezo calibration, it is worth using $NbSe_2$. The superconducting gap width is well known in this material and permits to check the spectroscopic resolution. Then, in magnetic field, the vortex lattice is well defined and can be observed easily at

low field (see figure 3.6).
Thus, the operating tests have shown that after the M2 modifications the system is working well.

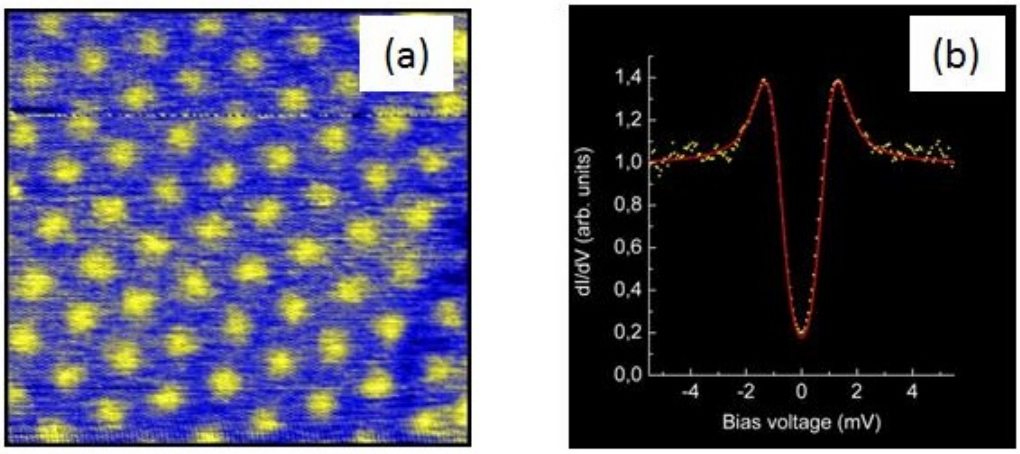

Figure 3.6: *Operating test of the experimental setup M2. (a) Vortex lattice in* $NbSe_2$ *(200nm x 200nm, B=4T, T=2K). Vortices correspond to the yellow circles and the blue area is superconducting. (b) dI/dV spectra in* $NbSe_2$ *without magnetic field and at T=2K. In yellow are the experimental data that can be well fitted by the BCS theory in red.*

3.5 Experimental setup M3

To combine scanning tunneling microscopy/spectroscopy and *in-situ* transport measurements and improve spectroscopy reproducibility, the experimental setup M3 was used. It is another home-made microscope which construction started in years 2000. The STM head was designed by D. Roditchev on the basis of Pan's STM, and realized at INSP. The whole experimental system was designed by D. Roditchev, and settled by D. Roditchev, Denis Fokin, François Debontridder and Tristan Cren at INSP.
In STM measurements, it is essential to control the surface quality of the sample. Contaminations by the environment are multiple and degrade the studied surface. In such conditions, it becomes difficult to realize reproducible and stable measurements. For this reason, it is necessary to work under ultra-high vacuum conditions. Thus, samples prepared *in-situ* are much more suitable to STM measurements.
During this thesis, NbN samples were elaborated in Germany. Samples deteriorations rendered STM measurements difficult. The first STM measurements made using M2 on NbN films revealed some difficulties to scan the surface and obtain reproducible density of states spectra. Indeed, due to the surface oxidation, the samples evolve with time. Their Tc decreases while their resistance per square increases on a time scale of a few weeks after receiving it (see chapter 1). Meanwhile, TEM measurements revealed the presence of an oxide layer. Thus, to continue, it was essential to couple *in-situ* transport measurements and local electronic properties spectroscopy on freshly prepared samples. It was a motivation to pursue with the M3 experimental setup.

3.5.1 Specifications

General view of the microscope

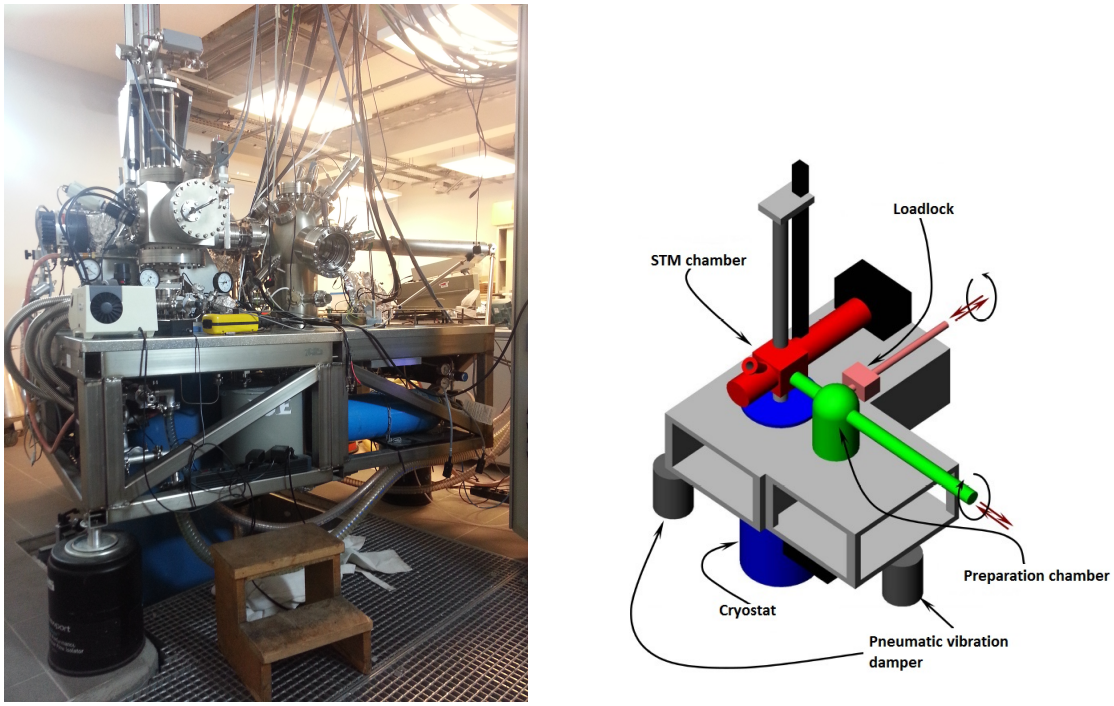

Figure 3.7: *Picture and sketch of the experimental setup M3.*

A fast entry load-lock chamber is used to introduce samples and tips in the preparation chamber. The load-lock chamber is equipped with a turbo-molecular pump and gases entries (N_2 and ^{4}He). Precisely, the load-lock allows to preserve the vacuum in the preparation chamber.
The latter is equipped for in-situ Pb-ultrathin film elaboration and characterization and accommodates a transfer rod which permits to introduce tips/samples in the STM chamber. This rod has a longitudinal rotation movement which is used to rotate the sample in the direction of the triple evaporator or in the direction of the LEED-Auger. At the end of the rod, there is a resistive heater. Thereby, samples and tips can be heated up to 1100K. They can also be cooled down to 200K thanks to a copper bar linked to a copper cone which could be pressed against a liquid nitrogen pot. It is a simple to use and performant system for *in-situ* sample preparations.
In the STM chamber, it possible to store up to six samples and six tips. All elements present in the preparation chamber can be seen in figure 3.9.
During this thesis, only the heating system has been used. Indeed, in the case of our NbN samples it allows for removing water and some surface contaminants in ultra-high vacuum 10^{-11}mbar prior to STM/STS measurements. The composition of the residual gas in the preparation chamber can be analysed by a mass spectrometer. Finally the preparation chamber is equipped with an Ar ion gun. It was used for sample etching. Practice has shown that we could reduce the normal state resistivity (at 300K) of the sample and keep the properties of the films surface (figure 3.8). The idea was to control the film properties in-vacuum, and approach the superconductor-insulator transition on initially the same sample. However, this treatment was attempted only at the end of the thesis, and no systematic measurements of ion sputtering on thickness, superconducting

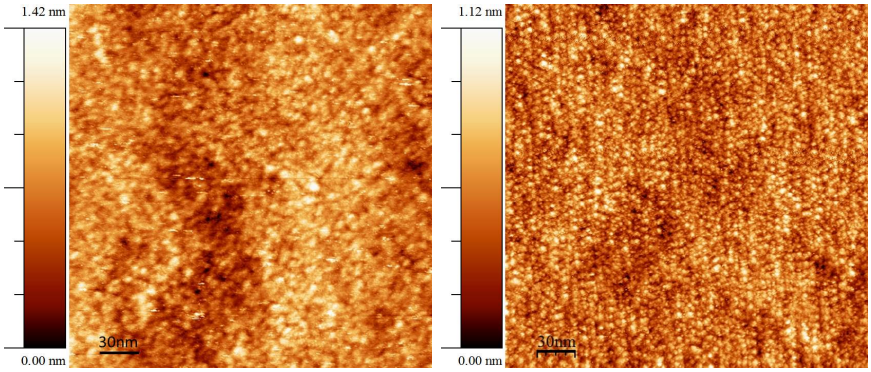

Figure 3.8: *STM images 300nm*300nm before (left) and after (right) ionic bombardment on a NbN sample. In both cases, grains are observed. On the image after ionic sputtering, grains appear smaller. It is a multiple tip effect.*

critical temperature and the proximity to the superconductor-insulator transition were performed.

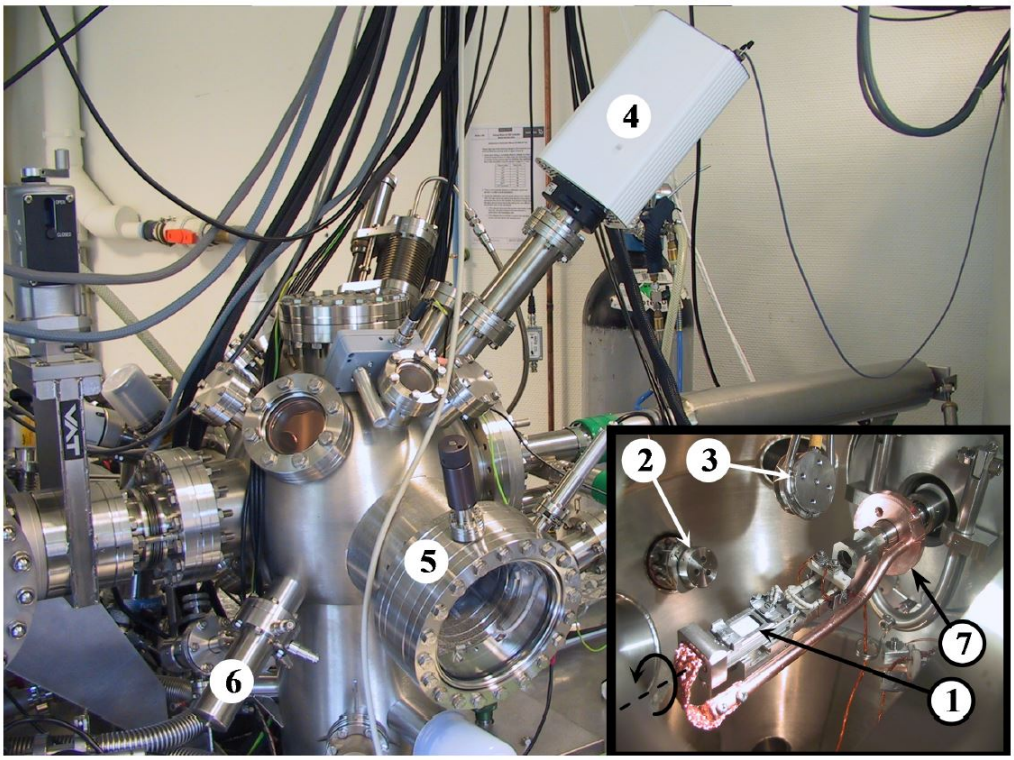

Figure 3.9: *External and Internal views of the preparation chamber: (1) Sample holder system, (2) Triple evaporator, (3) Quartz balance, (4) Mass spectrometer, (5) LEED-Auger system, (6) Ion gun, (7) Copper cone used to have a thermal contact with the nitrogen pot.*

STM head

The STM head is a unique modulus which was designed in a way to accept standard sample holders and tip holders from the "OMICRON Nanotechnology" company (figure 3.10). The scanning system is also based on piezoelectric tube.

One is under the tip and serves to scan the X-Y directions and control the tip-sample distance Z. An XY motor using piezo stacks allows for coarse lateral displacements of the sample.

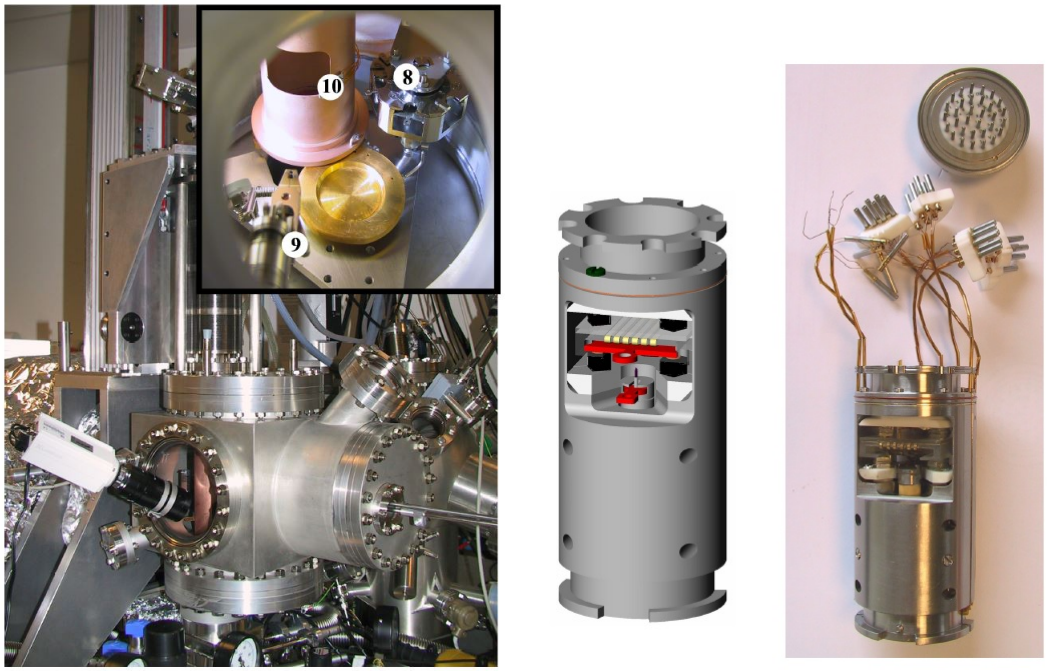

Figure 3.10: *Left: External and internal views of the STM chamber: (8) Tips and samples carousel storage, (9) Wobble-stick, (10) Copper screen shielding the STM head. Right: Sketch and picture of the M3 STM head. In red are the tip holder (below) and the sample holder (above). The contact springs for in-situ transport measurements are seen in yellow, above the sample holder.*

Cryogenic system

To reach the temperature of 300mK, the standard "OXFORD Instrument" superinsulated ^{4}He cryostat (TESLATRON) is associated with a ^{3}He cooling system (originally designed by D. Roditchev and realized by ICE Oxford) adapted for the experimental setup M3. The STM head chamber is connected to the cryostat through a long UHV tube (figure 3.11). A step motor is used to vertically displace the rod at the end of which is the STM head, down to the magnet center. On this rod, a copper cone called "1K cone" is also located. In working position the 1K cone is plugged to the 1K pot - an active element of ^{3}He refrigerator allowing for He re-condensation process. Throughout the rod, copper-golden buffles reflect the radiations coming from the upper part of the rod.
The ^{3}He refrigerator contains a sorption pump. When cold, it adsorbs ^{3}He gas and traps it. The sorption pump is heated until 50K to desorb ^{3}He gas while pumping the 1K pot. He_3 condenses in contact with 1K pot and falls down to the bottom of the cryostat in volume 13 (figure 3.11). Once all initially trapped ^{3}He gas is desorbed out of sorption pump and recondensed at the bottom of the refrigerator, the heater of the sorption pump is turned OFF. The sorption pump cools down, and starts "pumping" on liquid ^{3}He. The pressure and the temperature of liquid ^{3}He lowers down. With the sorption pump, a temperature as low as 300mK can be reached. This temperature lasts about 40 hours until all liquid ^{3}He ends.

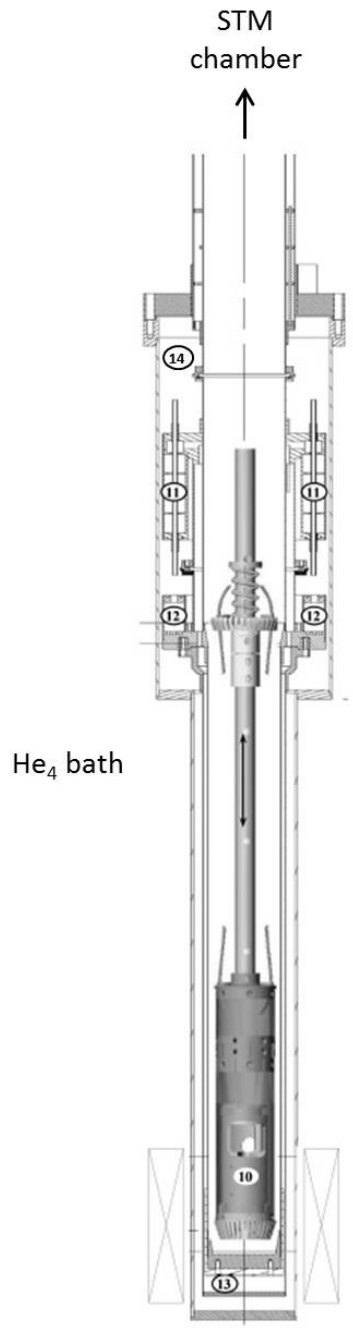

Figure 3.11: *M3 cryogenic system sketch. The STM Head (10) is located at the end of the rod used to move it in the UHV insert. The cone at its extremity is pressed on the* ^{3}He *socket (13) which is in direct thermal contact with the volume where* ^{3}He *is condensed. The* ^{3}He *sorption pump is located on (11), under the 1K pot (12). In (14) is located the Internal Vacuum Can (IVC) used to isolate the helium 4 bath from the* ^{3}He *cooling system.*

Electronics and control

On experimental setup M3, a SCALA current pre-amplifier is associated to MATRIX electronic control. These modulus are both fabricated by the "OMICRON Nanotechnology" company. The electronics was modified by F. Breton to meet requirements of the

home-made STM.

3.5.2 *in-situ* transport measurements

To measure the resistance versus temperature characteristics of NbN samples in M3, it was necessary to make some modifications. The sapphire pocket which receives the sample holder was already equipped with 6 wired electric contacts. In order to measure the resistance of the sample, it was just required to modify the "OMICRON" sample holder and realize the external wiring to the sourcemeter.
As can be seen on figure 3.12, an insulating (MACOR) disc was implemented in the central part of the holder; 4 flat Copper contacts were glued on it. Moreover, to preserve the UHV conditions, a sample fixation system was created. By using this technique, no more glue is needed to fix the sample.
The newly created sample holder, enables to have 4 contacts on the sample. However, it is not yet possible to measure resistance while doing STM/STS experiments.
A Keithley source-measure was used to measure the resistance. It allows to inject a low current down to 1pA and to measure precisely resistances as high as 10 GigaOhms.

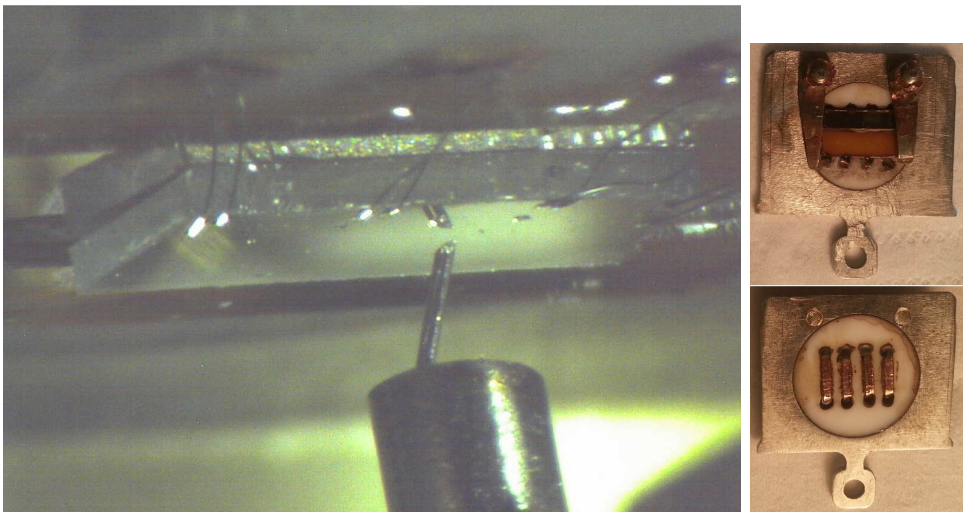

Figure 3.12: *Left: Picture of the NbN sample where one can see the Al-bonding used for transport measurements. Right: Top and bottom views of the modified "OMICRON" sample holder. Contacts are made through copper ribbons and a fixation system for the sample has been created.*

3.6 PPMS transport measurements

To complete the resistance versus temperature characteristics measured in STM M3, PPMS (Physical Properties Measurements Systems) transport measurements have been performed. The "Quantum Design" PPMS includes a cryogenic system permitting to quickly increase and decrease the temperature from 300K to 1.8K.
There are 2 options available to measure resistivity with the PPMS:

- Resistivity option
- ACT (AC Transport) option

The resistivity option uses a DC current source which can generate an excitation ranging from 5nA to 5mA. The voltmeter has a maximum input voltage of 95mV. It is good for resistance from 1Ω to 1MΩ.
The ACT option uses an AC current source which can generate an excitation ranging from 1μA to 2A.The voltmeter is available in the full range [-5V;+5V]. This option is optimized for relatively low resistances. Indeed, the best accuracy obtained is for resistance lower than 100Ω.
Transport measurements were performed by means of a standard four-probe technique with Al-bonding. Measurements are typically made by passing a 0.01mA current through the sample and measuring the voltage drop accross the sample in one direction. An AC bias current of a frequency of 17Hz was used. It is also possible to generate a magnetic field up to 14T perpendicular or parallel to the sample.
I(V) characteristics show no hysteresis when measured with increasing and decreasing current (see figure 3.13). Thus, heating or other thermoelectric effects could be excluded from the measurements.

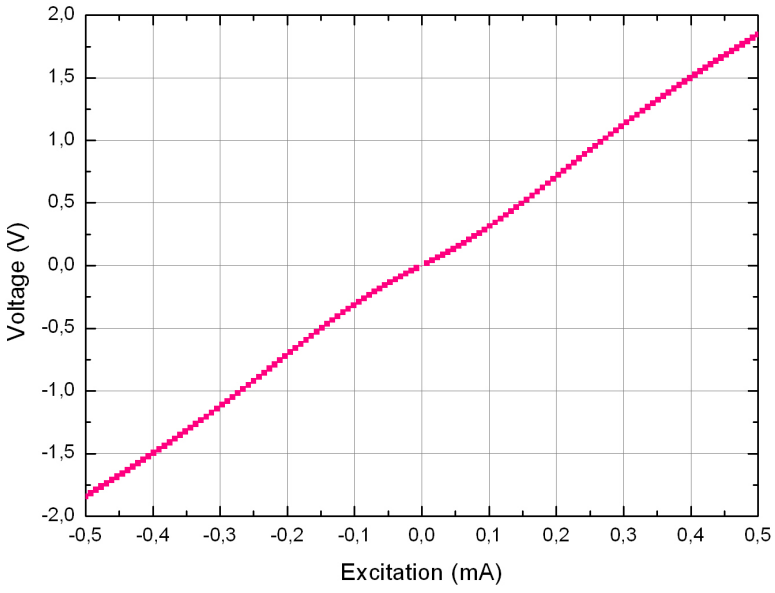

Figure 3.13: *I(V) curve measured at 1.8K with PPMS by passing an AC current from -0.5mA to 0.5mA through a NbN 2.16nm thick sample. It is not possible to distinguish between the increasing or decreasing current. No hysteresis is observed. A non linearity can be seen because the measurement has been performed on a superconducting sample.*

Chapter 4

Effect of magnetic field on the superconducting properties

Contents

4.1 Quantum phase transition

4.1.1 General theory of scaling

The phase transitions which take place at finite temperature are considered to be classical, although involving quantum mechanisms. Conversely, quantum phase transitions [Sac11, Gol10, GD10] occur at absolute zero temperature when a parameter of the Hamiltonian of the system is changed. Thus, all finite-temperature transitions are to be considered classical even in highly quantum-mechanical systems like superconductors. It does not mean that quantum mechanics is not important because in its absence, there would not be an ordered state.
The superconductor-insulator transition at zero temperature is therefore considered as a quantum phase transition. The tuning parameter can be disorder, doping or magnetic field. Close to the quantum critical point, quantum fluctuations are stronger at a microscopic scale but not at the longer scales that control the critical behavior. Namely, quantum mechanics is needed for the existence of an order parameter, but it is classical fluctuations that govern it at long wavelengths.
In order to better understand the origin of the critical exponents, we will give some generalities about quantum statistical mechanics that are described in [SGCS97]. To understand what happens close to the quantum critical point, it is important to know how the system evolves. In statistical mechanics of quantum systems, the quantities of interest are the partition function of the the system:

$$Z(\beta) = Tre^{-\beta H} \tag{4.1}$$

with H the Hamiltonian that governs the system. In this equation, the temperature is assumed to be finite: $K_B T = 1/\beta$. In order to understand what happens when T=0, it is possible to take the limit $T \to 0$. Thus, the free energy becomes the ground state energy and from Z, the thermodynamic quantities of interest can be obtained. It is noticeable that the operator density matrix $e^{-\beta H}$ takes the form of a the time evolution operator $e^{-iH\tau/\hbar}$. The imaginary value $\tau = -i\hbar\beta$ is associated to the time interval over which the system evolves. When the partition function is written in terms of a complete set of states:

$$Z(\beta) = \sum_n \langle n \mid e^{-\beta H} \mid n \rangle \tag{4.2}$$

Z takes the form of a sum of imaginary time transition amplitudes for the system to start in some state $\mid n\rangle$ and return to the same state after an imaginary time interval $-i\hbar\tau$. Thus, calculating the thermodynamics of a quantum system is the same as calculating transition amplitude for its evolution in imaginary time.
Thus, in the region of the quantum critical point, one can represent the quantum system by a classical model of D=d+1 dimensions. Therefore, it is necessary to translate the standard ideas developed in classical statistical mechanics in terms appropriate for d+1 dimensions where the additional dimension is imaginary time. Thus, the quantum phase transition theory is constructed by mapping a given quantum system in d-dimensional space onto a hypothetical classical system in the D-dimensional space. The imaginary time is used to create a subspace at a temperature T. Therefore, The evolution of the system in quantum phase transition is governed by quantum dynamics and has a temporal propagation.
The critical region is characterized by scaling laws which critical exponents are defined only by the dimensionality of the system, the symmetry group of its Hamiltonian, namely the universality class of the transition and the range of interactions. These exponents may not describe the microscopic mechanisms occurring in the system under study.

Close to the quantum critical point, there is a spatial correlation length of the order parameter diverging as:

$$\epsilon = |\delta|^{-\nu} \tag{4.3}$$

with $\delta = (\mathrm{K} - \mathrm{K_c})/\mathrm{K_c}$ and $\mathrm{K_c}$ is the value of the tuning parameter K at the critical point. The time correlation length is diverging as:

$$\xi_T = \epsilon^z = |\delta|^{-\nu z} \tag{4.4}$$

The scaling analysis of the critical regime in the superconductor-insulator transition is of particular interest in our case. The parameter K used to induce the transition in NbN thin films is the perpendicular magnetic field H. The physical quantity under study is the resistance of the sample: R=f(H,T,E) where T is the temperature and E is the electrical field.
The two diverging lengths are characteristic of a quantum critical point and will serve to determine the correlation length exponent ν and the dynamical scaling exponent z. The latter, depends essentially on the range of the interactions and defines the effective dimensionality of the system d+1 where d is the spatial dimension. Due to these divergences, several physical quantities have a finite-size scaling behavior. Thus, the dependence of the physical quantities of interest as a function of the independent variables leads to the relation:

$$R(\delta, T) = Rc\ f(\delta/T^{1/\nu z}) \tag{4.5}$$

where Rc is the value of the resistance at the quantum critical point.
Another relevant parameter to study for the superconductor-insulator transition is the electrical field E as described by Sondhi and al. in [SGCS97]. At fixed temperature, the resistance obeys the scaling law:

$$R(\delta, E) = Rc\ f(\delta/E^{1/\nu(z+1)}) \tag{4.6}$$

This relation is very useful because it gives information about the critical exponents that are not available in the temperature scaling analysis. Indeed, from temperature scaling, one can infer the value of νz while from electrical field scaling, one can infer the value of $\nu(z+1)$. Thus, the two critical exponents ν and z can be obtained separately making it to check their consistency. Close to the critical point, the nonlinear response of the voltage as a function of the current is related to critical fluctuations and the effect of the electrical field can not be associated to a simple heating effect.

The value of the dynamical critical exponent z describes the relative scaling of the time and the length scale in a quantum phase transition problem. It is of great interest since it is used to determine the universality class of the system. In 1990, Fisher and al. [Fis90] argued that the value z=1 is relevant for systems which have long-range Coulomb interactions. In 2001, Igor Herbut [Her01] proposed a theoretical justification for this relation which is widely used. He showed that the competition between the correlated quantum disorder and Coulomb interactions can also lead to a quantum critical point at which the dynamical critical exponent is z=1.

4.1.2 Predictions for the critical exponents

Bosonic scenario

In the bosonic scenario, the superconductivity can be made vanishing by the action of phase fluctuations of the order parameter. In this case, Cooper pairs persist on the insulating side of the transition and the transition can be described by a model of interacting

bosons in the presence of disorder. One of the bosonic scenario is based on the work of M. Fisher [Fis90] in which there is a symmetry between pairs and vortices. Some important predictions of the model are the universal value of the resistance and the range of value for the critical exponents ν>1.

Fermionic scenario

In the fermionic scenario, the density of states and the Cooper pairing are suppressed on the insulating side due to enhanced electron-electron interactions and some important issues have been delivered by the work of Finkelstein [Fin87]. Cooper pairs break up into single electrons at the transition. Fluctuations of the amplitude of the superconducting order parameter induce the transition rather than fluctuations of the phase.

Critical exponents

Transport measurements made in InO [OKSS13, HP90] and MoGe [YK95] amorphous thin films both revealed $\nu = 1.3$ and z=1 for the superconductor-insulator transition tuned by magnetic field. These critical exponents values are claimed by the authors to be associated to the theoretical prediction of the bosonic nature of the insulating state.
However, the interpretation of the critical exponents values is not explicitly given in the bosonic or fermionic scenario. The theory give the following informations about the universality class :

- $\nu = 2/3$ corresponds to a 2D+1 quantum XY model equivalent to a 3D classical XY model,
- $\nu = 4/3$ corresponds to a classical percolative transition,
- $\nu = 7/3$ corresponds to a quantum percolative transition.

Thus, there is various values of the exponents that can be expected for the bosonic scenario proposed by M. Fisher [Fis90].

4.2 Scaling law analysis in NbN

Transport measurements have been performed at LPEM in collaboration with Brigitte Leridon. We have induced the superconductor-normal transition by applying a magnetic field perpendicularly to the sample. The aim of this experiment is to determine the critical exponents of the quantum phase in NbN and then compare it to what is obtained in others systems. First, a sample having a thickness of 2.16nm and a critical temperature close to 4K. The R(T) characteristic is visible on figure 4.1.
Figure 4.2 shows typical R(H) data curves. A fixed point is observed for temperature between 1.8K and 2.6K for Rc = 11kΩ and Hc=10.7T. It is noticeable that Rc is not equal to the quantum of resistance $R = h/4e^2$ predicted by the bosonic scenario.
The resistance per square of NbN versus temperature values are plotted in figure 4.3. A plateau is clearly visible for B=10.7T, which corresponds to a resistivity of about 11kΩ/sq. This is the manifestation of the presence of a quantum critical point at zero temperature. In such case, this plateau corresponds to a region of quantum fluctuations near the quantum critical point. Checking if there is a scaling law is relevant in this range of temperature.

The success of finite size scaling analysis is part of the evidence for the superconducting-metal transition to be a continuous quantum phase transition. The scaling analysis was performed at the vicinity of the fixed point, Hc=10.7T and Rc = 11kΩ/sq. Figure 4.4 shows the scaling of the curves which proves to be of good quality. Next, we extracted the

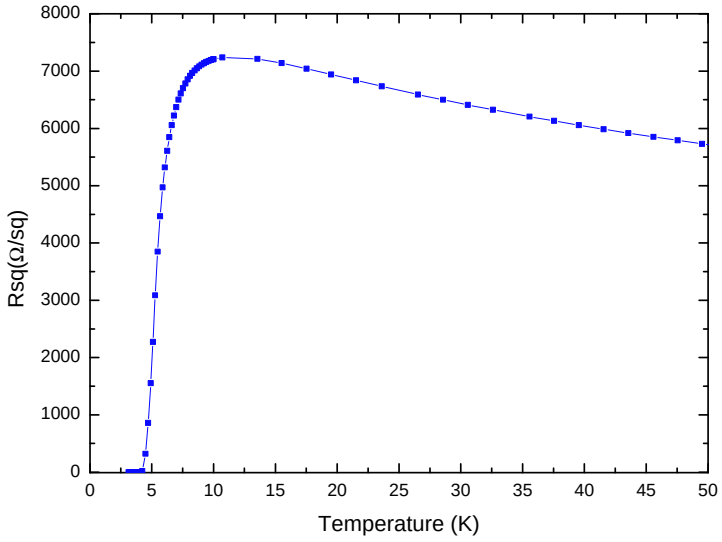

Figure 4.1: *Resistance versus temperature data of the studied sample. The critical transition temperature is close to 4K.*

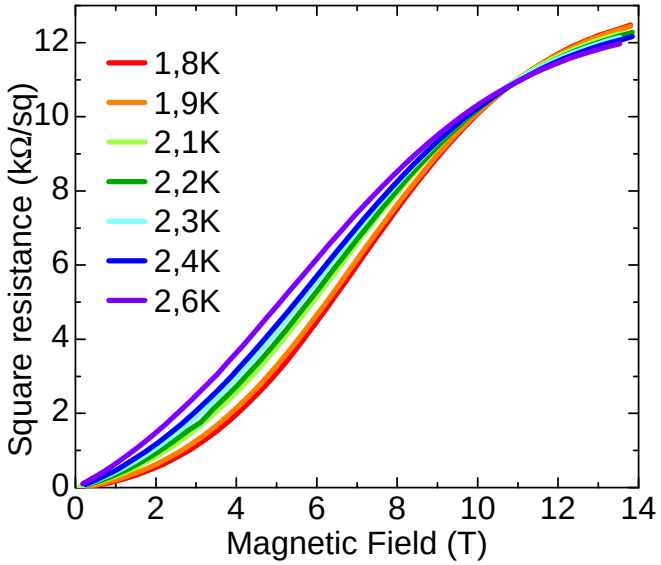

Figure 4.2: *Resistance versus magnetic field data for temperature between 1.8K (lower curve at low field) and 2.6K (upper curve at low field).*

scaling exponents νz as described above. The critical exponents are found experimentally by rescaling of a factor t on a log-log plot, the resistance curves as a function of magnetic field for the different measured temperature T. Thus, one can infer the scaling exponents νz by plotting t versus temperature and determining the slope with a linear fit of the data. The scaling exponent νz is found to be equal to 0.66.

As described by Sondhi [SGCS97] and experimentally studied by Markovic [MCM+99] in Bi thin films, the values of the critical exponents can also be extracted by tuning the

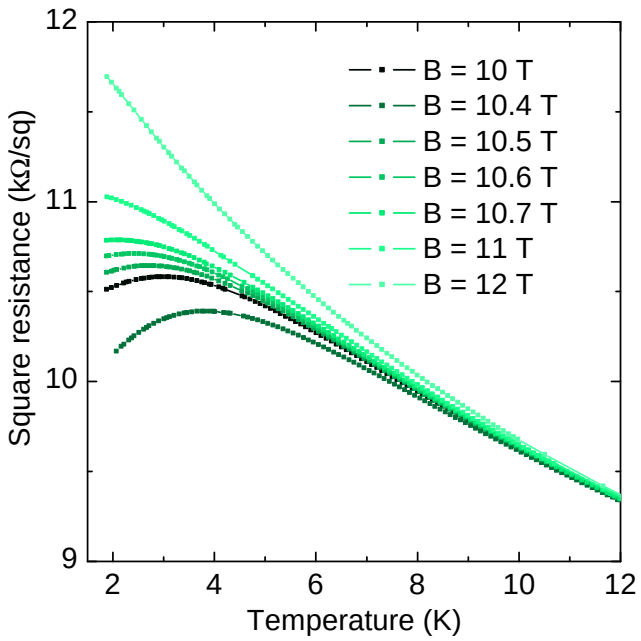

Figure 4.3: *Square resistance as a function of temperature for different magnetic field values ranging from 10T to 12T. A plateau is visible from 1.8K to approximately 2.5K for a magnetic field of 10.7T.*

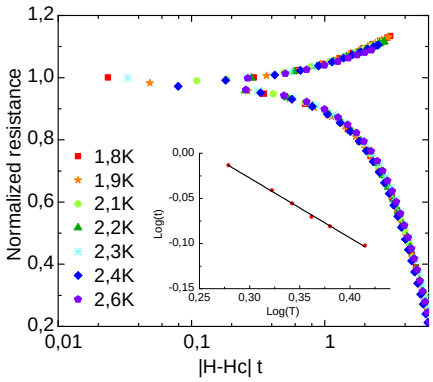

Figure 4.4: *Resistance per square as a function of the scaling variable /H-Hc/t for different temperatures and a critical magnetic field of 10.7T. We adjust* $t = T^{1/\nu z}$ *in order to obtain the best collapse of the data. Inset: log-log plot of the parameter t versus temperature used to determine value of* νz.

electrical field instead of the temperature.
The data of figure 4.5 and figure 4.6 are measured at constant electrical field, namely constant voltage. We performed the measurements at different fixed currents and then selected the points having the same voltage for the different magnetic field. Experimentally, the electrical field applied to the sample is equivalent to the measured current. Figure 4.5 shows a crossing point in the R(H) curves suggesting also the existence of a quantum critical point. At this fixed point, we find Rc = 12.5kΩ and Hc=7.8T. A scaling behavior can be demonstrated by using the same methods described above. As shown in figure 4.6 the slope of the log-log plot gives $\nu z = 1.33$.
The two independent determinations of νz with the temperature and $\nu(z+1)$ with the

electrical field therefore lead to $\nu \simeq 0,66$ and z=1.

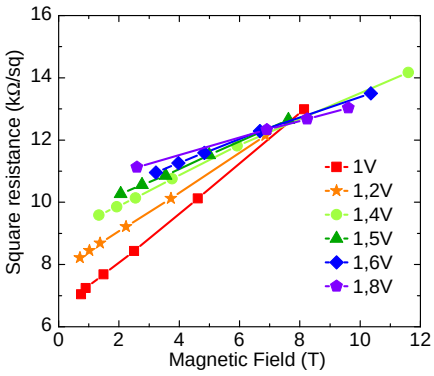

Figure 4.5: *Resistance as a function of magnetic field at different voltage drop across the sample at a temperature of 1.9K.*

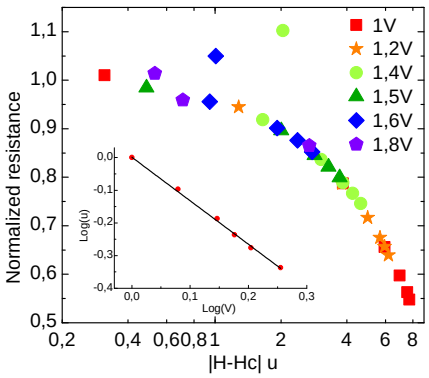

Figure 4.6: *Resistance as a function of the scaling variable /H-Hc/u for different voltage drops across the sample at a temperature of 1.9K. We adjust* $\mathrm{u} = \mathrm{E}^{1/\nu(\mathrm{z}+1)}$ *in order to obtain the best collapse of the data. Inset: log-log plot of the parameter u versus voltage used to determine the value of* $\nu(z+1)$.

Such critical exponents are consistent with a 2D quantum XY model which can correspond to a 2D Josephson junction array model. We may be in the presence of phase fluctuations. In NbN films, our results seem consistent with InO samples [Sac07]. In Bi [MCM$^+$99] thin films, the same exponents are found for comparable critical temperature as we measured. However, if we consider that we are not in the bosonic scenario since $\nu < 1$, but in the fermionic scenario, our results are consistent with the STM/STS results we obtained on a similar sample in the viewpoint of the thickness and the critical temperature. Indeed, we observed that the gap develops on a strong Altshuler-Aronov background which corresponds to electron-electron interactions. This parameter is taken into account only in the fermionic scenario. Moreover, we observed that the normal state square resistance as a function of the Tc for various thickness of samples follow the Finkelstein's law until this particular thickness approximately.

4.3 Superconducting fluctuations

Studying the superconducting fluctuations means studying the appearance of superconductivity, when T>Tc. The presence of short-lived Cooper pairs in the normal state gives a supplementary channel for electron transportation and modifies the conductivity of the material. The extra conductivity is often reffered to as "paraconductivity". Three contributions are distinguished.
The first one has been calculated by Aslamasov and Larkin [AL68]. It corresponds to the direct contribution of the short-lived Cooper pairs to the conductivity.
An indirect effect has been proposed independently by Maki and Thompson [Mak68, Tho70]. It is a quantum correction that correspond to the coherent diffusion of electrons forming a Cooper pair by the impurities. It has been revisited by Reizer [Rei92].
The last contribution is the correction to the density of state. When the electrons are in a short-lived Cooper pair, they are no longer available to participate to the charge transport. The total number of electronic states is therefore affected by the Cooper interactions and thus lead to a diminution of the Drude conductivity of the normal carriers. However, this correction to the conductivity is usually neglected.

4.3.1 Aslamasov-Larkin conductivity

In a classical metal, the conductivity in the absence of superconducting fluctuations is given by :

$$\sigma_{AL} = \frac{ne^2\tau}{m} \tag{4.7}$$

With n the electron density, τ_s the mean scattering time, e is the charge and m the effective mass of the charge carriers.
By analogy, the contribution of the superconducting fluctuations to the conductivity can be expected to be :

$$\sigma_{AL} \simeq \frac{(2e)^2}{m*} \sum_k \frac{\langle|\psi_k|^2\rangle\tau_k}{2} \tag{4.8}$$

Where each terms of the sum corresponds to a supplementary channel of conduction. This sum over k can be calculated by performing an integration if k is considered to be a continuous variable.

$$\sigma_{AL}^{3D} = \frac{e^2}{32\ \hbar\ \xi_0\ ln(T/Tc)^{1/2}} \tag{4.9}$$

$$\sigma_{AL}^{2D} = \frac{e^2}{16\ \hbar\ d\ ln(T/Tc)} \tag{4.10}$$

$$\sigma_{AL}^{1D} = \frac{\pi\ e^2}{16\ \hbar\ A\ ln(T/Tc)^{3/2}} \tag{4.11}$$

ξ_0 is the coherence length at zero temperature, d is the thickness of the film and A is the section of the wire. Moreover, close to the transition, $\epsilon = \ln(\mathrm{T/Tc}) \simeq \frac{\mathrm{T-Tc}}{\mathrm{Tc}}$. More detailed about the calculation can be found in [Tin04, AL68].

4.3.2 Experimental results

The paraconductivity $\Delta\sigma(\mathrm{T})$ is extracted from the normal state $\sigma_{\mathrm{N}}(\mathrm{T})$ conductivity, namely the resistance measured when applying a high magnetic field and the conductivity in zero magnetic field $\sigma(\mathrm{T})$:

$$\Delta\sigma(T) = \sigma(T) - \sigma_N(T) \tag{4.12}$$

By using formula 4.12, the conductivity due to superconducting fluctuations in the normal state is probed. The paraconductivity has been studied for various NbN samples which characteristics are displayed in table 4.1.

sample name	Thickness (nm)	Tc (K)	R_{sq} (300K,Ω/sq)
C_1	2.50	9.4	2370
B_2	2.33	7.1	2450
A_2	2.16	4.5	3150
Y_0	2.10	4.3	2350
F_0	2.90	9.0	1390

Table 4.1: *Sample thickness, critical temperature Tc (estimated by the extrapolation to zero resistance of the tangent at the inflection point of the resistance curve) and resistance per square R_{sq} at room temperature for the different samples studied.*

The analysis of the experimental paraconductivity was done in collaboration with Brigitte Leridon, Sergio Caprara and Marco Grilli.
For samples A_2 and Y_0, it was possible to recover the normal state conductivity by applying a magnetic field of 14T perpendicularly to the sample. It is due to their proximity to the insulating transition already at zero magnetic field. However, for thicker samples, C_1, B_2 and F_0, it was not possible to recover the normal state with 14T. We have assumed that their normal state could be extrapolated with the same law that worked to fit the normal state under 14T in thinner samples:

$$\rho_N(T) = aL_T^3 + bL_T^2 + cL_T + d \tag{4.13}$$

With $L_T = \ln(1/T)$. As the inclusion of the L_T^2 term did not improve the fit, it has been fixed to zero in order to reduce the number of fitting parameters.
By measuring the resistance of F_0 under a very high magnetic field of 55T, it was possible to recover the normal state of this thicker sample. These measurements have been done at LNCMI in collaboration with Baptiste Vignolles (see next section). This gave us the opportunity to check whether the fitting law was well chosen for the others samples. Figure 4.7 shows the data with 55T for sample F_0 and the fit determined by using the law 4.13 without using the data of the normal state measured under 55T. We can conclude from this analysis that the fit assuming 4.13 for the normal state resistance used to calculate the paraconductivity is good since there is only slight differences between the measurements of the under high magnetic field and the assumed calculated normal state.
Figure 4.8 displays the resistance per square under zero magnetic field, the resistance per square under 14T for samples A_2, Y_0, the extrapolated normal state resistance of samples B_2, C_1 and F_0. We distinguish two groups of samples : B_2, C_1 and F_0 that have a thickness higher or equal to 2.33nm and a higher Tc and samples : A_2 and Y_0 that have a thickness lower than 2.33nm and a lower Tc
Figure 4.9 shows the extracted paraconductivity variations as a function of reduced temperature. For samples B_2, C_1, and F_0, which have a higher superconducting transition temperature, the behavior of the paraconductivity is consistent with a 2D Aslamasov-Larkin conductivity when approaching Tc. Moreover, the prefactor exactly matches the AL 2D value, without any adjustable parameter, suggesting that superconductivity in these system is truly BCS-like and that Maki-Thompson fluctuations are absent or negligible [Rei92].
However, for the thinnest samples A_2 and Y_0, the paraconductivity exhibits a very specific

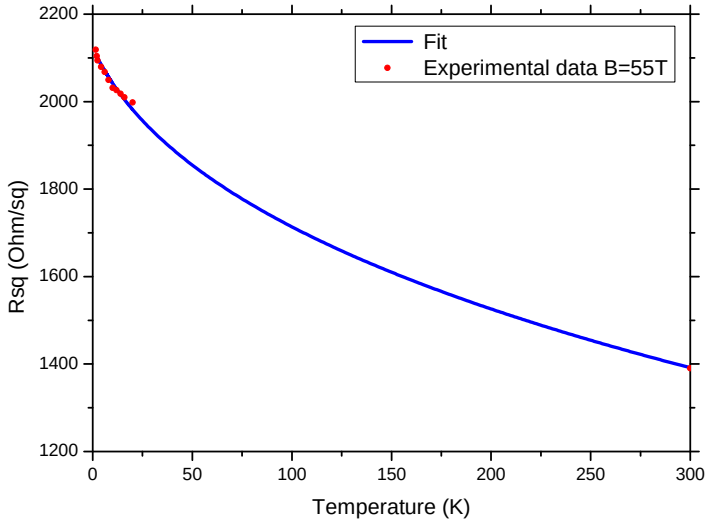

Figure 4.7: *Fit of the experimental data measured under a magnetic field of 55T. The law used to fit the normal state resistance is* $R_N(T) = 3,52L_T^3 + 12,1L_T + 2112,62$. *It has been determined from the experimental data without magnetic field but one can see that it is fully consistent with the normal state data measured at 55T.*

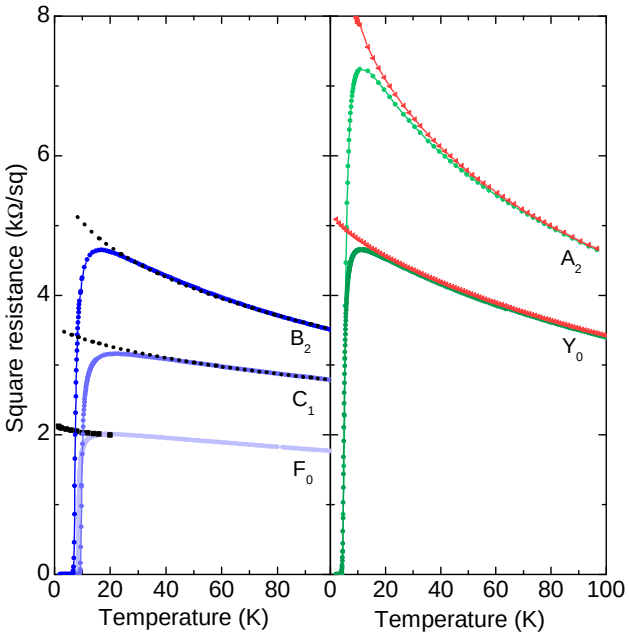

Figure 4.8: *Blue and green dots: Square resistance under 0T as a function of temperature for samples* A_2, B_2, C_1, F_0 *and* Y_0. *Red triangles: resistance under 14T perpendicular magnetic field for sample* A_2 *and* Y_0. *Dotted line: extrapolated normal state resistance for samples* B_2, C_1 *and the normal state measured under 55T for* F_0.

law: $\Delta\sigma \simeq \epsilon^{-2}$. It is clear from figure 4.9 that the paraconductivity cannot be fitted by the classical Aslamasov-Larkin 2D conductivity. If the 2D behavior is present, it could be

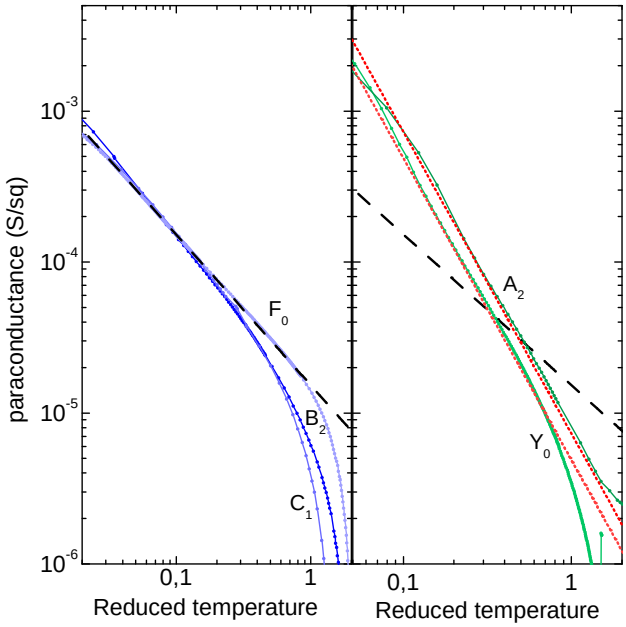

Figure 4.9: *Left: Extracted paraconductivity for the thicker samples B_2 ($d = 2.33\,nm$), C_1 ($d = 2.50\,nm$)and F_0 ($d = 2.90\,nm$) as a function of the reduced temperature $\epsilon \equiv \ln(T/T_c)$. The agreement with Aslamazov-Larkin prediction for a 2D system (black dashed line) is excellent, without any adjustable parameter. Right: Square paraconductance as a function of ϵ for the thinner samples A_2 ($d = 2.16\,nm$) and Y_0 ($d = 2.10\,nm$). The red dotted lines correspond to $\Delta\sigma = 0.01e^2/(\hbar\epsilon^2)$ (lower) and $\Delta\sigma = 0.03e^2/(\hbar\epsilon^2)$ (upper). The expected AL 2D paraconductivity is also shown (black dashed line).*

only close to Tc (see figure 4.10). Such ϵ^{-2} behavior was observed in two other samples of about the same thickness as the one of X_0 and A_2.

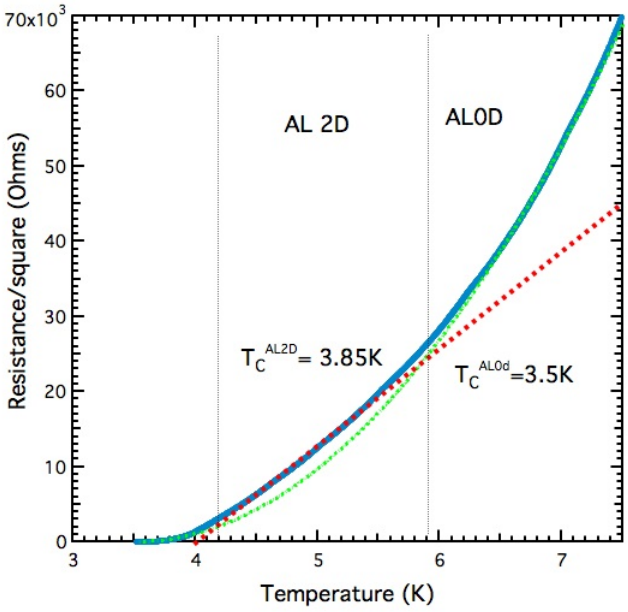

Figure 4.10: *Extracted paraconductivity for sample A2. In blue are the experimental data, in green is the AL0D fit and in red is the AL2D fit. A cross-over between the two regime is observed very close to Tc.*

4.3.3 Interpretation/Discussion

The law $\Delta\sigma \simeq \epsilon^{-2}$ could be interpreted naively as an extrapolation of the Aslamasov-Larkin model in 0D with $\Delta\sigma \simeq \epsilon^{-(2+z-D)\nu}$. Indeed, within the theory of Aslamasov-Larkin, the dynamical exponent z=2 corresponds to the damping of Cooper pairs above Tc and the exponent $\nu = 1/2$ takes the mean field value. This behavior suggests the formation of 0D fluctuating regions that we refer to as "supergrains". Since the transition is observable, our results should evidence a change in the behavior of fluctuations when decreasing the film thickness leading to a 0D-2D crossover. Indeed, close enough to Tc, a conventional 2D behavior should be recovered when the coherence length exceed the typical distance between two supergrains. The magnetic field induced transition which critical exponents were shown to be consistent with a 2D quantum XY model could therefore be explained by a phase fluctuating array of these supergrains.

4.4 High magnetic field study

4.4.1 Introduction

High-field magnetoresistance measurements have been performed at the *Laboratoire National des Champs Magnetiques Intenses de Toulouse* (LNCMI-T) in collaboration with Brigitte Leridon and Baptiste Vignolles. It is classical four points transport measurements under perpendicular magnetic field. An AC current of 1μA and a frequency of 2kHz has been used. These measurements were useful to study thicker samples. Indeed, the critical field above which the superconductivity is destroyed in NbN is very high and in the PPMS, the maximum magnetic field available is 14T. It is not enough to induce the normal state in thicker NbN films. We measured two samples. The first one has a thickness lower than 2.33nm and a lower Tc. The second one has a thickness higher than 2.33nm and a higher Tc.
The generated magnetic field increases very quickly but decreases more slowly. As can be seen in figure 4.11, the entire cycle lasts about 6ms.

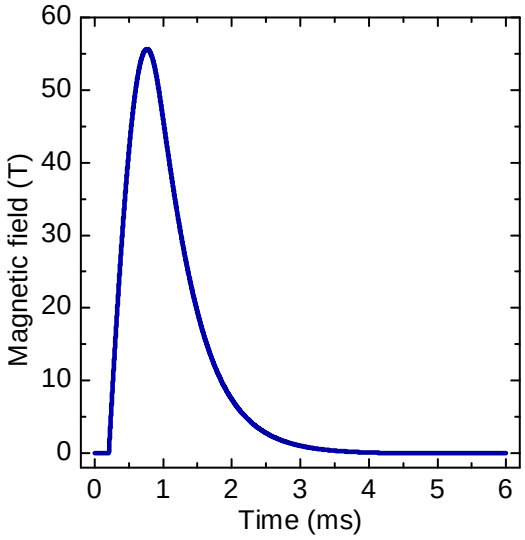

Figure 4.11: *Evolution of the magnetic field amplitude as a function of time for a ramp from 0T to 55T. The acquisition time is 6ms but increasing the magnetic field lasts only 1ms.*

During the decreasing ramp of the magnetic field from 55T to 0T, the sample may be heated up due to the induced voltage in the measurement wires. We observed that the measured points in decreasing magnetic field corresponds to higher temperatures. However, when increasing the magnetic field, the temperature of the system was shown to remain at the setpoint temperature by comparison with the PPMS data up to 14T.

4.4.2 Magnetoresistance on NbN

Magnetoresistance measurements have been performed on two samples (see table 4.2). The temperature varied from 1.5K up to 20K and the magnetic field increased from 0T to 55T. The magnetic field is applied perpendicularly to the sample.
Figure 4.12 shows typical magnetoresistance curves obtained for the studied samples Y_0 and F_0. A slight magnetoresistance peak is visible for the thinnest sample (Y_0). However, it is a weak effect since the resistance reaches only three times its 300K and 0T value

Sample's name	Y_0	F_0
Thickness (nm)	2.1	2.9
Tc (K)	4.3	9.0
Rsq(300K) (Ω/sq)	2350	1390

Table 4.2: *Properties of the samples measured at LNCMI. The magnetic field has been increased up to 55T and the temperature has been varied from 1.5K to 5K in order to study the magnetoresistance.*

between 15T and 55T. The sample does not get into a strong insulating state.
In both cases, a crossing point is visible. This point is associated with the critical field Hc of the magnetic field driven superconductor-metal transition. Indeed, it separates the superconducting state from the normal state. Below Hc, the resistance is decreasing with temperature to the superconducting state. Above Hc, the resistance is increasing when decreasing the temperature. Thus, the situation is similar to the one described previously for quantum phase transition and the scaling law analysis could be done.

4.4.3 Interpretation of the negative magnetoresistance

In the thinnest sample Y_0, the negative magnetoresistance is clearly visible but in the thicker sample F_0, the peak is absent.
The decreasing of resistance with increasing the magnetic field could be related to different scenarii. Especially, it could be attributed to the effect of superconducting fluctuations in superconducting granules for granular systems as described by [BE99, BEL00].
Another scenario has been developed by Shimshoni et al. [SAK98] and is based on percolation. The system is described as superconducting puddles separated by metallic area. The size of these puddles diminishes when increasing the magnetic field due to suppression of superconducting correlations. This lead to the positive magnetoresistance. Up to a particular magnetic field Hc, the puddles are so small that it is no more favorable for the current to pass throughout them but it is preferable to pass through the normal area. This effect increases when increasing the magnetic field and leads to a negative magnetoresistance. The theoretical work of Dubi and al. [DMA06] is consistent with this explanation of the magnetoresistance measurements.
Magneto-transport measurements performed on InO [SEJ+05] or in amorphous nanohoneycomb bismuth films [NHS+09] both reveal the existence of a huge peak of resistance when applying a magnetic field. It is interpreted as localized Cooper pairs in the insulating state. However, it is noticeable that the magnetoresistance peak in these two systems are not of the same order of magnitude as the magnetoresistance peak measured in NbN by Chand and al. [CSK+12]. For them, it is an evidence that even after the destruction of the superconducting state by applying a magnetic field, the superconducting correlations continue to play a key role in the electronic properties.
In our NbN thin films, there is not a huge magnetoresistance peak. However, the negative magnetoresistance is consistent with a scenario of phase fluctuations in supergrains. It should be interesting to performed the same study on thinnest sample, closer to the insulating transition to investigate if the magnetoresistance peak increases. It will help to interpret the small negative magnetoresistance observed here.

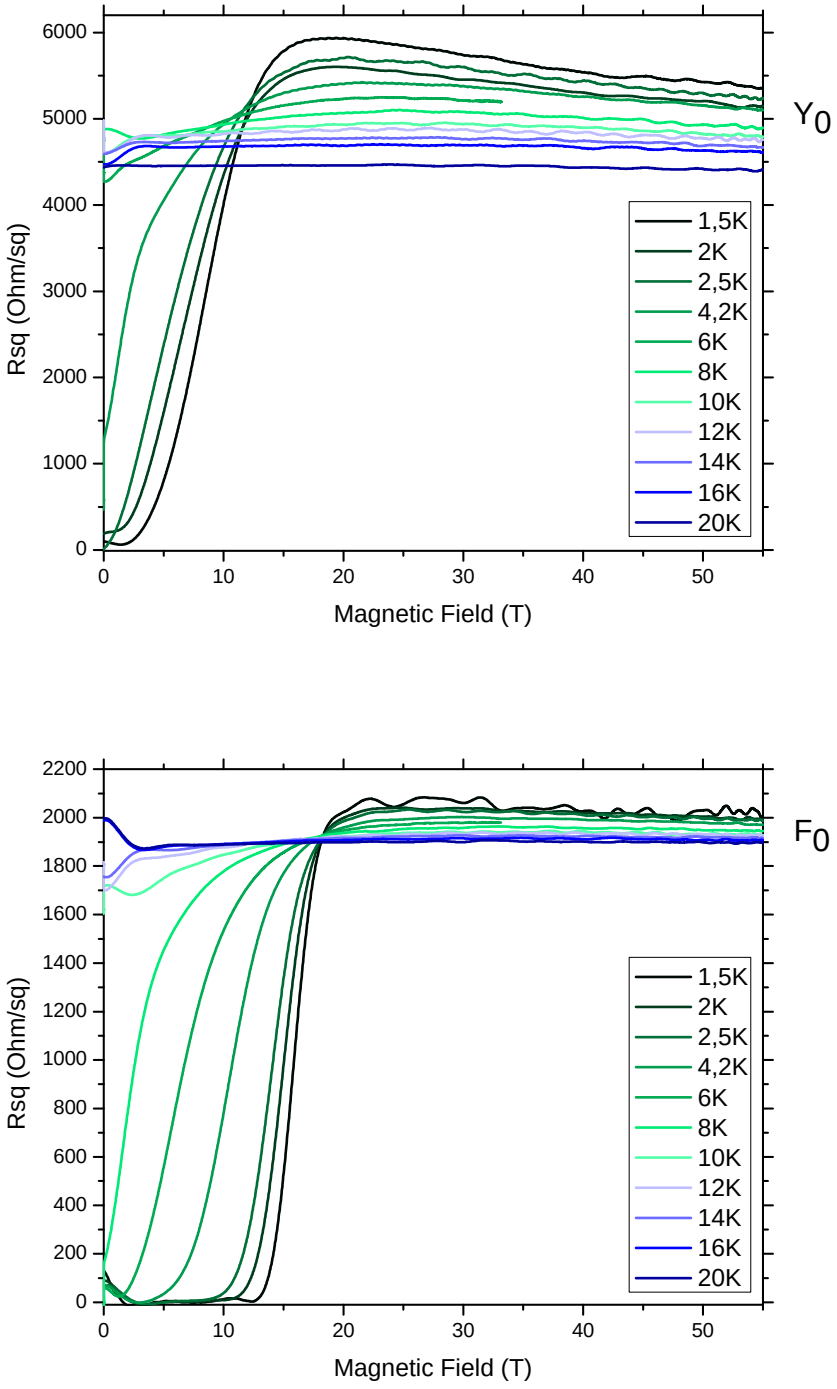

Figure 4.12: *Magnetoresistance of two samples. On the top:* Y_0 *and on the bottom:* F_0. *The magnetic field is increased from 0T to 55T and the temperature varied from 1.5K to 20K. For sample* Y_0*, a small peak appears and the magnetoresistance is then negative. The thicker sample* F_0 *is less sensible to the applied magnetic field. In both cases, a crossing point is clearly visible.*

Chapter 5

Effect of the film thickness on the superconducting properties

Contents

5.1 Introduction

The superconductor-metal transition has been addressed locally by scanning tunneling spectroscopy measurements on our M2 experimental setup. The transition was induced by varying the NbN film thickness. As a result the critical temperature and the Ioffe-Regel parameter which is related to the mean free path, are reduced. $k_F l$ has been determined by [SGB+09] in a previous work, in the framework of the free electron model as:

$$k_F l = \hbar(3\Pi^2)^{2/3} n_e^{-1/3} (e^2 \rho_n)^{-1} \tag{5.1}$$

where n_e is the free electron concentration deduced from Hall measurements and ρ_n is the normal state resistivity, directly extracted from transport measurements.
Our results show evidence of unconventional signatures in the tunneling spectra when approaching the SIT[NCB+13].

5.2 Electrical properties of the films

A series of NbN thin films with various thicknesses has been studied. The bulk superconducting transition temperature of NbN film is about 15K. Properties of the samples evolve with the thickness. For example, in a 12nm thick sample, the Tc is around 15K and $k_F l \simeq 5.7$. These parameters hardly change for the 6nm films for which Tc $\simeq$ 14K and $k_F l \simeq 5.6$. However, when reducing the thickness by a factor two, d=3.2nm, Tc drops to 10.7K and $k_F l \simeq 2.6$ [SGB+09]. Here, the Tc is extracted from transport measurements and is defined as the temperature at which the resistance drops to half its normal state value.
The characteristics of the studied samples are indicated in the following table:

Thickness d (nm)	15	8	4	2.33	2.16
Tc (K)	15	14.5	13.3	9.4	6.7

Table 5.1: *Thickness and corresponding critical temperature of the studied NbN samples by tunneling spectroscopy measurements.*

The low-temperature Ginzburg-Landau superconducting coherence length parameter ξ has been estimated from extrapolated H_{C2} measurements to be between 4 and 6nm [SGB+09] for thicknesses between 15 and 3.2nm. Thus, films with a thickness smaller than 4nm could be assumed to be in the two dimensional limit with respect to the superconducting properties. Indeed, in this case the order parameter is expected to be homogeneous in the direction perpendicular to the surface.
Figure 5.1 shows smooth superconducting transitions, with a continuous and gradual reduction of the Tc with film thickness. These measurements were done from 300K to 4K at the Karlsruhe Institute of Technology directly after the films growth.

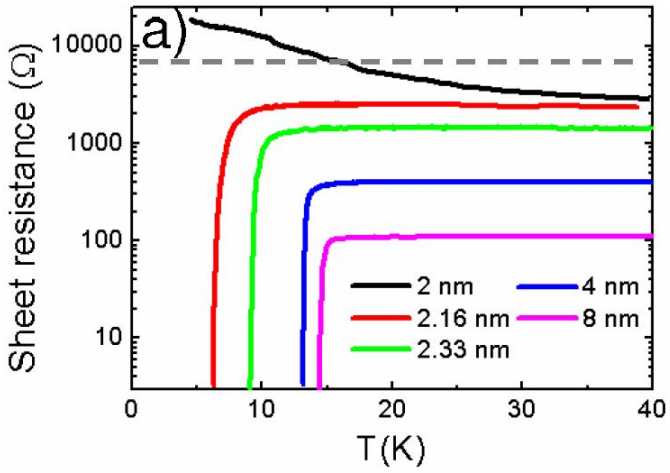

Figure 5.1: *Square resistivity as a function of temperature of the studied samples. The dashed line indicates $h/4e^2$, the quantum resistance for pairs.*

5.3 Tunneling spectroscopy results

5.3.1 Evolution of the tunneling spectra with the thickness

The thickest film (d=15nm) shows a conventional superconducting gap $\Delta = 2.85$meV at 2.3K, spatially homogeneous, with a classical BCS shape (figure 5.2). The gap disappears at Tc as expected for a conventional superconductor. When applying a magnetic field, a disordered vortex lattice appears in the conductance map. It is an evidence of the local disorder existing in this thin film. The presence of vortices is also a proof of the long-range quantum coherence of the superconducting condensate.
The vortex lattice is disordered and it is noticeable that some of them were cut during the scan because they jumped away. They may have interacted with the tip. We observed that the size of the vortex is bigger than ξ. This may also be due to the vortex movement and the tunneling spectroscopy measurements gives thus a mean density of states.

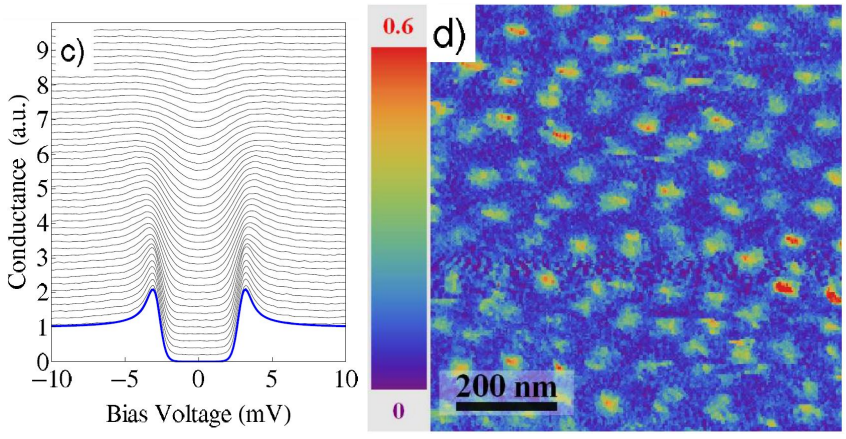

Figure 5.2: *c) Evolution of the tunneling conductance spectra with the temperature from 2.3K to 15K (vertically shifted for clarity). The bottom blue line is the BCS fit at T=2.3K; d) dI/dV conductance map at zero bias under magnetic field B=1T. It reveals a disordered vortex lattice.*

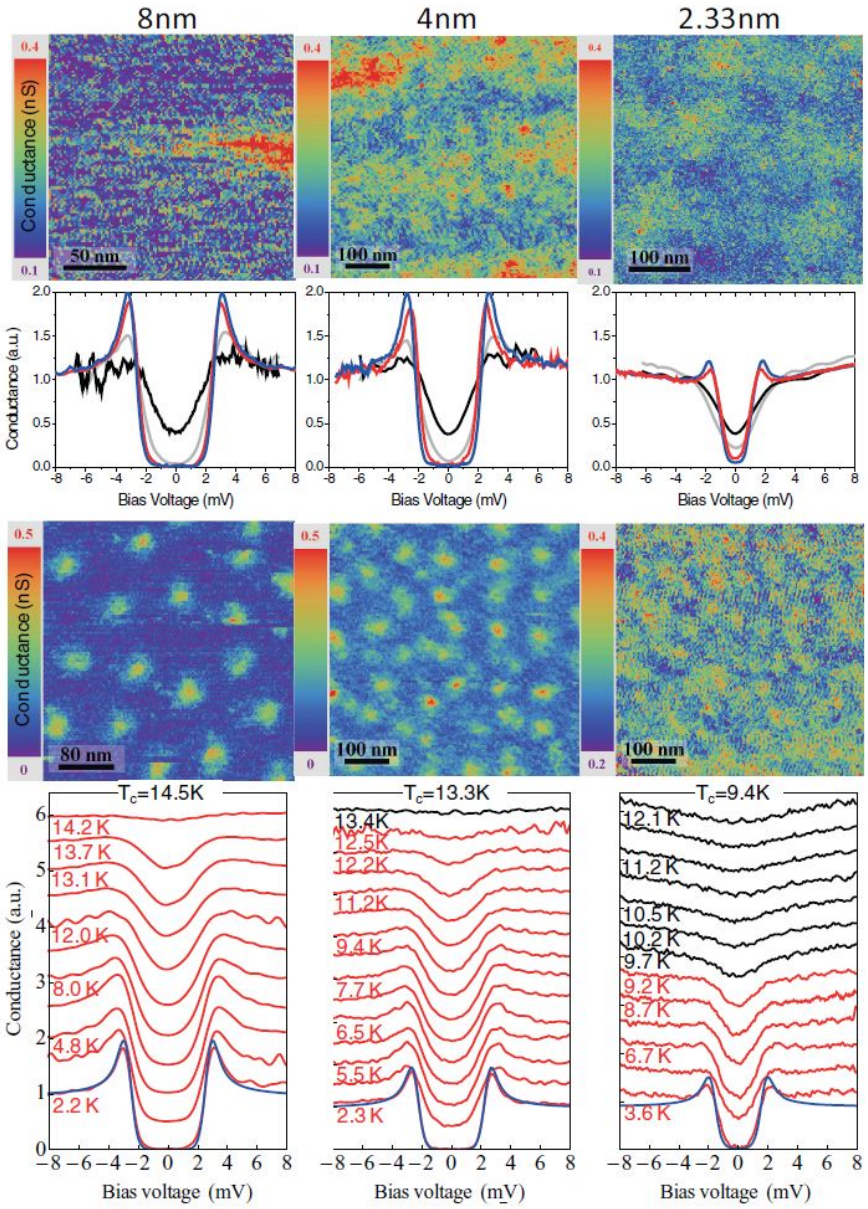

Figure 5.3: *From left to right column: tunneling characteristics of 8, 4 and 2.33nm thick films. From top to bottom: the first row shows normalized STS conductance maps representing the color-coded spatial variations of the dI/dV signal measured at 2.3K at the gap onset (for V=1.7mV, V=1.7mV and V=1.1mV); second row: normalized individual tunneling conductance spectra representative of the spatial variations observed among the local conductance spectra (red and blue curves) at 2.3K; the black curves show typical spectra measured at 4K in magnetic field (B=1T, B=1T and B=2T) at the vortex cores and outside the vortex (gray curves); third row: dI/dV conductance maps at V=0 showing images of the vortex lattice at 4K (for B=1T, B=1T a,d B=2T); fourth row: temperature evolution of the normalized dI/dV tunneling spectra (vertically shifted for clarity). The temperature is indicated below the corresponding spectra. Red and black curves correspond respectively to the superconducting and normal state. The bottom thick blue lines are BCS dI/dV calculations at the indicated temperature.*

Results obtained on the 8nm, 4nm and 2.33nm thick NbN films are shown in figure 5.3. The 8nm thick sample which exhibit a superconducting gap of 2.7meV, showed conductance map with very small spatial inhomogeneities of the superconducting gap. A disordered vortex lattice is also observed. The temperature dependence of the superconducting gap remains conventional, namely the gap disappears at Tc. However a weak broadening of the low temperature gap is observed. To take into account this effect, a pair-breaking parameter has been added: Γ_{dynes}. This is a very small effect since $\Gamma_{\text{dynes}} = 0.01\text{meV}$ in this sample.
The situation changes in the 4nm thick sample. Weak spatial inhomogeneities are observed in the tunneling conductance map. The gap width and the height of the coherence peaks are affected. These inhomogeneities are characterized by two length scales that are visible on the conductance map (figure 5.3). The smaller one is less than 10nm, thus close to the coherence length. The larger one is of few hundreds of nanometers. Our analysis suggests that this latter length is related to slight film thickness variations (see figure 5.4). Indeed the underlying sapphire substrate may have atomic steps of characteristic size, since the substrate is heated at 850°C before and during deposition. The characteristic size should be similar to what has been observed previously [YMO$^+$95]. This size of few hundreds of nanometers agrees well with our observed spectroscopic changes. Thus electronic properties may also be affected as seen in the conductance maps by subtle structural effects of the substrate. Below Tc, the superconducting gap $\Delta = 2.4\text{meV}$ is BCS-like, with a Γ_{dynes} broadening parameter comparable to the 8nm case.
In the 2.33nm thick film, changes are more pronounced. Conductance maps revealed inhomogeneities comparable to those observed in the 4nm thick sample with the two same length scales. A well defined gap of 1.7meV exists everywhere but the amplitude of the coherence peaks is much reduced and broadened with respect to the low-temperature BCS expectation. dI/dV spectra below Tc are only approximately described by the BCS theory and a spectral broadening of $\Gamma_{\text{dynes}} = 0.05\text{meV}$ is now required. The vortex lattice is hardly observable. Nevertheless, a small spectroscopic contrast still allows for their identification. Inside the vortex cores, the conductance is not constant as expected but a large dip without coherence peaks is observed. This unusual feature is also common to 4nm and 8nm thick films and will be addressed later on the next chapter. This may also be due to the vortex motion. Indeed, if they are moving slightly from around their equilibrium position during the scan, we may measured a mean density of state value. Moreover, the normal state spectra (black curves) reveal now a "V-shape" background with a clear minimum at zero-bias, extended over a larger energy scale than the superconducting gap. A shallow pseudo-gap develops up to 1K above Tc. Significant deviations from the BCS theory are observed.

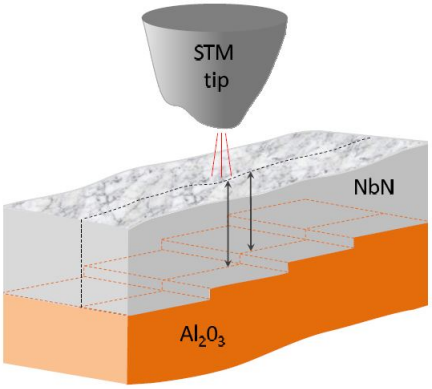

Figure 5.4: *Schematic view of the NbN thin film grown on a sapphire substrate measured by STM. The figure emphasizes the fact that from one sapphire atomic terrace to another, the local thickness of the NbN film might slightly vary, leading to sensitive changes of the electronic properties observed in the conductance maps.*

5.3.2 Unconventional superconductivity close to the SIT

In figure 5.5, are shown the results obtained for the 2.16nm thick sample. Striking changes are revealed in the tunneling characteristics. The superconducting gap is now measured to be equal to 1.3meV. The gap develops on a strong "V-shape" background (figure 5.5-e).
When the Tc is reached, the zero-bias conductance increases linearly with increasing temperature. This is a characteristic of the "V-shape" background. The opening of the superconducting gap occurs at Tc. It is detected as an anomalous kink in the dI/dV spectra (figure 5.5-g).
The spectra are not BCS-like anymore (figure 5.5-c). The Γ_{dynes} parameter is estimated to be equal to 0.1meV. The quasiparticle peaks are very much reduced as in the 2.33nm thick sample and in some area, they even completely disappear.
There are two length scales appearing in the conductance map (figure 5.5-a) showing spectral inhomogeneities comparable to those observed in the 4nm and 2.33nm samples. Indeed, the zero bias conductance and the quasiparticle peaks height vary slightly at the nanometer scale. Furthermore, large scale variations appear strikingly to be spatially ordered in parallel bands in some areas of the sample. It could be attributed as previously, to the sapphire atomic steps.
The spectra are almost insensitive to magnetic field. Up to 3T, no vortices could be observed. According to magnetoresistance measurements presented before, this is much below Hc_2 of this film.
Having a closer look at figure 5.5-a and -b and at spectra in figure 5.5-c and -d, when applying a magnetic field, the zero bias conductance increases. Two kinds of area could be distinguished in the 2.16nm conductance maps measured atB=0T and B=3T. In blue bands, there are small coherence peaks while in green/red bands these are absent. In the latter regions, the gap resembles to the pseudo-gap observed in vortex cores for thicker films and thereby seems to preclude vortices to be observed individually. The spectra in these regions look like to ones calculated on the insulating side of the magnetic field induced SIT [DMA07], supporting the idea that both systems have in common the loss of superconducting phase coherence.

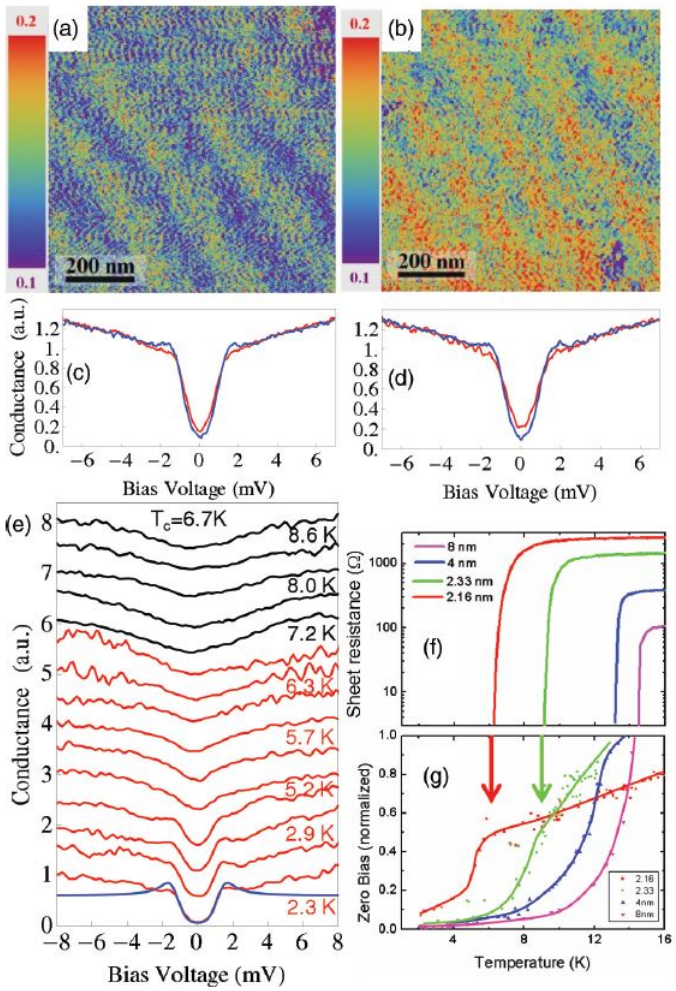

Figure 5.5: *Tunneling characteristics of the 2.16nm thick film at 2.3K. a) zero bias conductance map at B=0T, b) at B=3T. c) Typical variations among the corresponding local spectra for B=0T and d) for B=3T. e) Evolution of the dI/dV spectra with temperature (vertically shifted for clarity). The bottom thick blue line is a BCS dI/dV calculation at the indicated temperature with an additional broadening parameter. f) Zoom on R(T) of the 2.16-8nm films measured by transport compared to their g) temperature dependence of the zero-bias tunneling conductance dI(V=0)/dV.*

5.4 Analysis of the results

In table 5.2, are summarized the evolution of relevant parameters as a function of thickness. The gap Δ and the spectral broadening parameter Γ_{dynes} were determined by a BCS fit of a local tunneling spectra. Clearly, when decreasing the film thickness, while the Tc and Δ decrease, the Γ_{dynes} parameter increases. It is worth noting that the ratio $2\Delta/K_B Tc$ remains quite constant around 4 with a slight reduction. $\delta\Delta_{\text{BCS}}$ represents the typical spatial variation of the gap.

Thickness d (nm)	15	8	4	2.33	2.16
Tc (K)	15	14.5	13.3	9.4	6.7
Δ_{BCS} (meV)	2.85	2.7	2.4	1.7	1.3
$\delta\Delta_{BCS}$ (meV)	<0.03	0.03	0.08	0.2	-
Γ_{dynes} (meV)	<0.01	0.01	0.01	0.05	0.1
$2\Delta/K_BTc$	4.4	4.3	4.2	4.2	4.0

Table 5.2: *Thickness and corresponding parameters of the studied NbN samples.*

5.4.1 Effect of the magnetic field

In order to better understand the effect of a perpendicular magnetic field on NbN thin films, transport measurements were performed on other samples complementary to those studied by STM/STS. Indeed, the macroscopic resistive state is not known in STM but it is necessary to understand what happens to the superconducting state when applying a magnetic field. The characteristics of the samples were chosen in such a way that their critical temperature is close to the one of the sample of interest measured by STM/STS. The thinnest film has a thickness of 2.16nm and a Tc of 6.5K while the sample studied by STM had a thickness of about 2.16nm and a Tc of 6.7K. Thus, the properties of this 2 samples are quite similar. The thickest sample studied by transport measurements was a 17.5nm thick NbN film with a Tc of 15K which is close to the bulk critical temperature. These two samples have been measured from 300K down to 2K under a magnetic field varying from 0T up to 9T. The curves can be seen in figure 5.6.
It is worth noting that the 17.5nm and the 2.16nm thick samples have a completely different behavior in magnetic field. Indeed, the thicker sample remains fully superconducting at 2K for all magnetic field while the thinner become slightly resistive at 2K for $B \geq 1T$. Indeed, under 1T, the square resistance increase to 0.03Ω/sq.
The value of the square resistance at 2K is 6Ω/sq for B=3T. It means that when measuring the local electronic properties by STS at 2K, the 2.16nm thick sample should also be in very slightly resistive state under 3T. This observation may explain why the vortex lattice becomes more and more hardly observable when reducing the film thickness and may also contribute to explain other features. If the vortex lattice becomes less and less rigid as the thickness is reduced, it would lead to an increase of the vortex motion for low magnetic field trough a reduction of vortex-vortex interaction with decreasing thickness. The pinning of the vortex also decreases when decreasing the thickness.
If vortices are moving much faster than the acquisition timescale of a conductance map, then the measured local conductance would be the result of an average value over the different positions of the moving vortices. The pseudo-gap observed in the vortex core by STS would reflect this movement. This could explain why the size of the vortex core appears larger than the value of the coherence length in the conductance maps. Thus, several striking experimental facts can be accounted for by the existence of vortex motion.

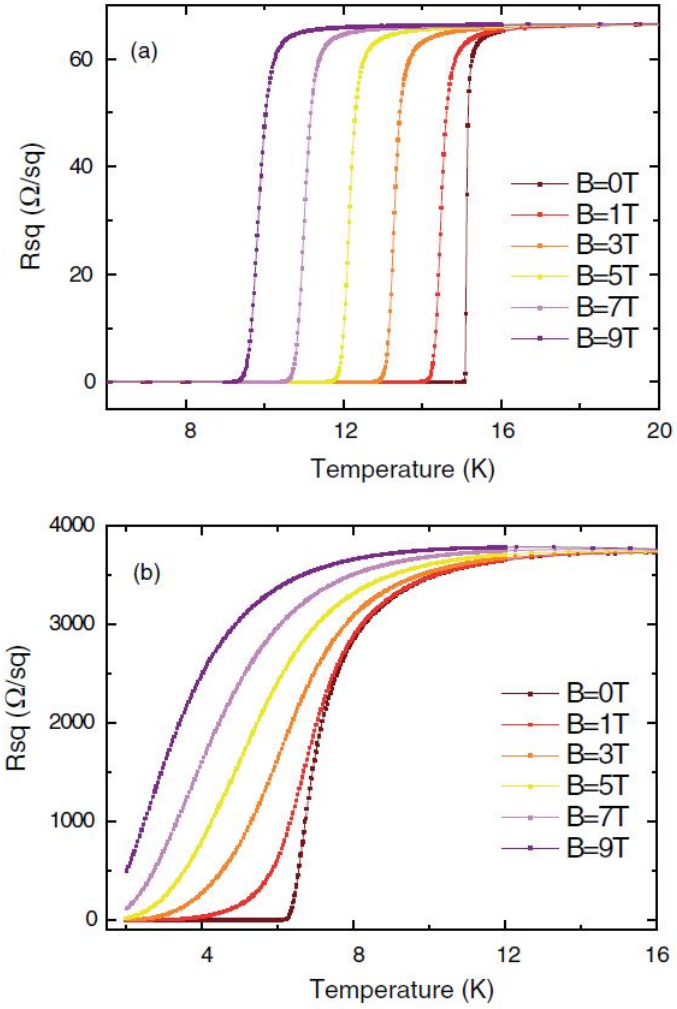

Figure 5.6: *Square resistance versus temperature for different magnetic fields in the range 0-9T for (a) 17.5nm thick NbN film with a Tc of 15K and (b) 2.16nm thick NbN film with a Tc of 6.5K*

5.4.2 Effect of Coulomb interactions

As explained in the fermionic scenario, the Finkelstein's law [Fin87] is used to describe the superconductivity suppression in homogeneous ultra-thin films. The evolution of Tc as a function of thickness can give precious information about the effect of the interactions and scattering of electrons in disordered 2D systems. The evolution of the critical temperature is given in equation 1.3 of the chapter 1. Here, Tc is reduced due to enhanced Coulomb interactions and a depression in the density of states. Figure 5.7 shows the Tc/T_{C-bulk} dependence versus square resistance for our studied NbN films. It follows almost perfectly Finkelstein's law. For high critical temperature (low R_{sq} values), the model gives a linear dependence of R_{sq}. This suggests that the joint action of Coulomb interactions and scattering by disorder (grain boundaries, impurities, surface and interface boundaries) are quite efficient mechanisms to reduce the critical temperature on the metallic side of the SIT, and thus to reduce also the gap amplitude.
The additional fact that the gap develops on a "V-shaped" background for the lower Tc-studied films is also consistent with the good fit of the Tc data by the Finkelstein theory.

Indeed, enhanced Coulomb interactions with increasing disorder are known to reduce the tunneling density of state at Fermi level [AAL80] which effects are at the basis of the Finkelstein theory. These spectroscopic features will be studied in details and at lower temperature in the next chapter.

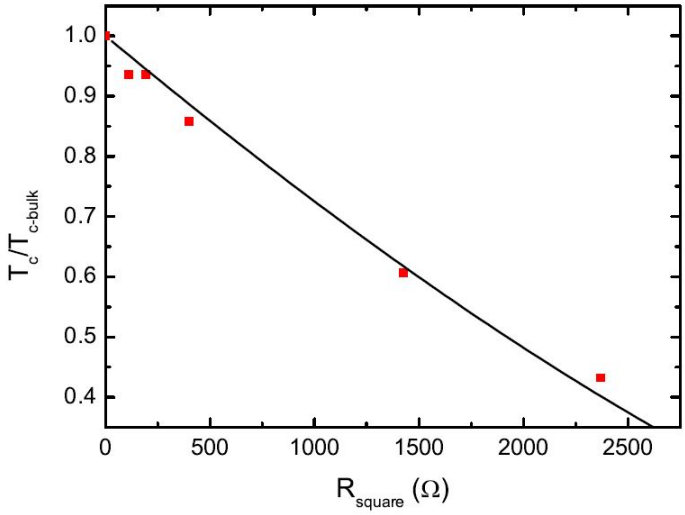

Figure 5.7: *Dependence of Tc/Tc-bulk, the superconducting critical temperature normalized by the bulk one, as a function of their square resistance* R_{sq} *in the normal state at 40K. Red squares are experimental data extracted from resistivity measurements. The black line is the fit by the Finkelstein law.*

Various other mechanisms could affect the Tc but the parameter selected by Finkelstein is $\ln(1/\tau Tc_0)$ because it is the dominant effect. For $|\ln(1/\tau Tc_0)| >> 1$, disorder and Coulomb interactions exist in the films.
In NbN, $\ln(1/\tau Tc_0) \simeq -5.65$. To compare, in TiN: $\ln(1/\tau Tc_0) \simeq -6.2; -6.8$ [SCB$^+$08, SCB$^+$10] and in MoGe: $\ln(1/\tau Tc_0) \simeq -7$ [GB84, DWGG86]. Thus, NbN films undergo comparably strong disorder and enhanced Coulomb interactions but maybe a bit smaller.

5.4.3 Does the passivation layer induce a proximity effect?

It is important to determine in which proportion the oxide layer on top of the NbN film could affect the superconducting properties. Even if the experimental measurements seemed to show that it is a very thin and insulating layer. The most unfavorable case would be when the oxide layer introduces a metallic layer in contact to the underlying NbN film, which would weaken the superconductivity in NbN films through proximity effect.
To take into account a possible proximity effect between the oxide layer and the NbN film, the McMillan model can be used (or equivalently the Usadel-bilayer model in the limit where $d < \xi$, d being the typical thickness of the proximity layer, since these two formalisms are mathematically equivalent). The proximity layer has been modelled by a non-superconducting layer, namely with zero superconducting gap. Firstly, the case of a NbN superconducting film thicker than the oxide layer has been studied. The intrinsic gap of the superconductor is $\Delta_{NbN} = 2.9$meV. The ratio between the integrated density of states is assumed to be of 20, as the NbN layer is much thicker ($\sim$ 20nm) than the oxide

layer ($\sim$ 1nm).

$$\frac{N_S\ d_S}{N_N\ d_N} \sim 20$$

Where d_S, d_N, N_S and N_N are respectively the thickness and the density of states per unit volume in the superconducting layer and in the oxide layer.
With a coupling parameter $\Gamma_N = 1$meV, the simulation figures 5.8-a are obtained. The blue curve corresponds to the density of state in the proximity layer and the black curve corresponds to the density of state in the superconducting layer. The red curve is the simulated differential tunneling conductance measured by STM on top of the proximity layer, at low temperature (T=2.3K). It is clearly different from the dI/dV measured by tunneling spectroscopy as the spectrum shows a gap close to the bulk value. Thus, the hypothesis of a weak coupling is not in agreement with the measured spectra.
When considering a larger coupling, $\Gamma_N = 10$meV, the resulting excitation spectrum exhibits a strong deviation from BCS which is not observed in the measurement. For a very strong coupling, $\Gamma_N = 50\text{meV} \gg \Delta_{NbN}$, a BCS-like density of state is recovered. This shape of the tunneling DOS is compatible with our spectra measured on thick NbN film.
Secondly, the case of a thinnest film has been studied. In this sample Tc is divided by 2.2 as compared to the thickest sample. Such a Tc reduction implies in the strong coupling approximation that the ratio $N_S d_S / N_N d_N$ should be of the order or less than unity (~ 0.82), if solely attributed to proximity effect.
Simulations have been done for the same parameters Γ_N as previously. The comparison with experimental spectra shows again that the scenario which is the most compatible with our measurements should assume a strong coupling between the proximity layer and the superconducting layer.
However, we are then led to the conclusion that the oxide layer would have a larger density of state than NbN itself that is not physical. It is also noticeable that Nb_2O_5 which is the more probable composition of the oxide layer, is an electric insulator. Moreover, the proximity effect does not explain the reduction of the coherence peaks height and the presence of the "V-shape" background. Thus, the proximity effect plays a minor role in our experiment and can be neglected. In conclusion, the oxide layer is strongly coupled to the NbN film and the system has to be considered as a whole system.

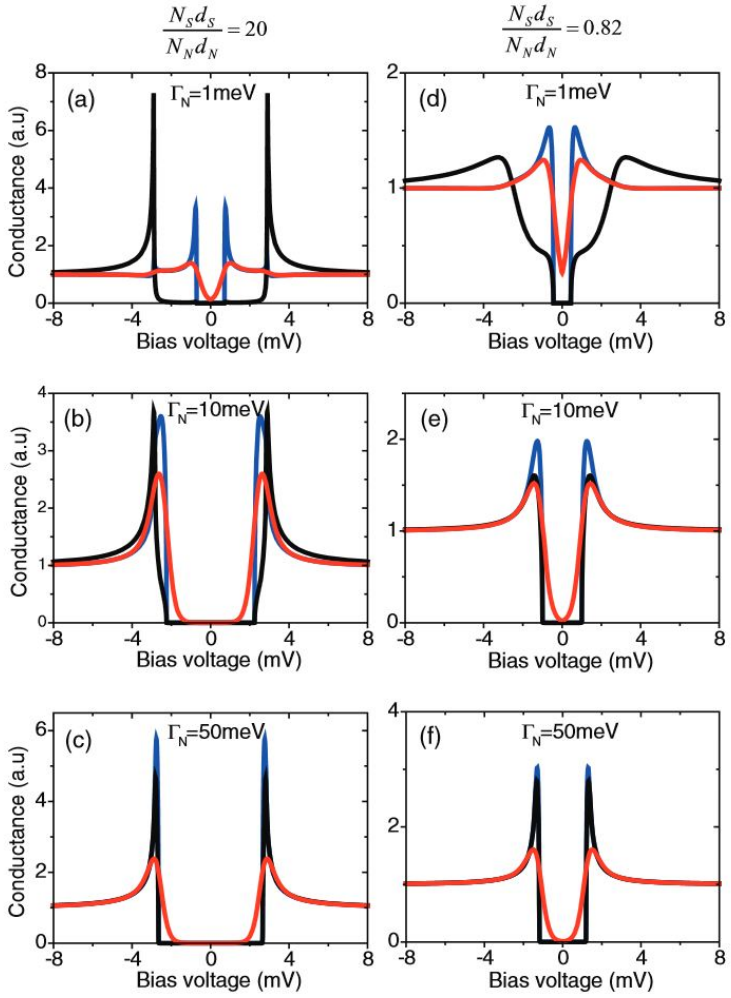

Figure 5.8: *Modelling of a possible proximity effect between the oxide layer and the superconducting NbN film calculated in the framework of the McMillan model for different values of the coupling parameter* $\Gamma_N = 1, 10, 50$meV *and assuming a ratio of 20 and 0.82 between the integrated density of states. Black curves: Partial DOS in the superconducting layer. Blue curves: Partial DOS in the proximity layer. Red curves: Simulated tunneling conductance at 2.3K.*

5.4.4 Tunneling data : comparison with previous works

It is noticeable that the ratio $2\Delta_{BCS}/kTc$ is almost constant when decreasing the film thickness. It corresponds to a scenario in which the amplitude of the order parameter is reduced when approaching the superconductor-insulator transition [Fin94]. However, these results seems at first glance in disagreement with those obtain by Sacepe et al. on TiN [SDC+11]. Indeed, in these systems, the ratio $2\Delta_{BCS}/kTc$ reaches higher values for films closer to the transition. It is probable that increasing further the disorder in NbN films would also lead to the same results, namely a $2\Delta_{BCS}/kTc$ increase. Indeed, experiments performed on a sample having a Tc equal to 4K goes in this direction. These results are shown in the next chapter.
There are several similarities between our spectroscopic data and measurements performed by the other groups. Particularly concerning:

- Spectral broadening leading to a gap filling
- Disappearance of the coherence peaks
- Shallow pseudo-gap over Tc
- "V-shape" background

These similarities have been observed in thick NbN (50nm) films in which the superconductor-insulator transition is induced by increasing disorder [CCJ$^+$08, CCK$^+$09, MKC$^+$11b]. The evolution of Tc as a function of $k_F l$ is very close to what is measured in our samples. Indeed, Chockalingam et al. studied films with Tc=6K ($k_F l = 2.2$) and Tc=4.1K ($k_F l = 1.6$) and in our 2.16nm thick NbN film, Tc=6.7K ($k_F l \leq 2.6$). Thus, these two systems have similar characteristics which lead to similar observations in tunneling conductance measurements. But it is noticeable that the main difference is the dimensionality of the system. In our case, the system is 2D in the viewpoint of the superconductivity and Chockalingam et al. samples are 3D.

On the other hand, these results present differences with reports on TiN (3.6-5nm) and InO (15 and 30nm). The difference concerns the ratio $2\Delta_{BCS}/kTc$ which hugely increases with disorder in these systems and also the pseudo-gap region which is larger [SCB$^+$08, SCB$^+$10, SDC$^+$11]. However, TiN and InO samples are closer to the insulating transition ($Tc \leq 0.4Tc_{bulk}$) than the films studied in this section. Indeed, in our case, $Tc \geq 0.4Tc_{bulk}$. An important feature is that in our case, the reduction of the density of state above and close to Tc is mostly due to the V-shape background and is not only an effect of the pseudo-gap. This issue seems to have been overlooked in the TiN and InO former studies. Nevertheless, these systems have in common the presence of spatial gap inhomogeneities. Moreover, in NbN as well as in TiN or InO, the coherence peaks disappear when increasing disorder while the conductance spectra deviate more and more from BCS behavior.

Thus, the study of NbN thin films as a function of their thickness reveal the deviation from the BCS theory when approaching the superconductor-insulator transition. We observed a decrease of the coherence peaks height, spatial inhomogeneities of the gap and the development of a "V-shape" background. However, further investigation closer to the insulating transition are necessary to compare our results with the theoretical predictions. We studied a 2.14nm thick film which a have Tc of 3.8K and the results are shown in chapter 6.

Chapter 6

Spectroscopic study of a thin film close to the superconductor-insulator transition

Contents

6.1 Experimental conditions

Previous results, presented in chapter 5, have been obtained with the experimental setup M2. We have obtained interesting results on NbN thin films having various thicknesses. However, the lowest temperature accessible is 2K , and the magnetic field was limited to few Tesla during the experimental run. Moreover, the long term stability of the microscope was not good enough to allow for the measurements of several conductance maps at the same sample area by varying successively parameters like B or T. In order to complete and extend this work, it was necessary to study thinner samples with a lower Tc to get closer to the insulating transition and have interesting and more striking features. The experimental setup M3 has been used to reach 300mK and be able to increase the magnetic field up to 7T. Moreover, in this experimental setup, it is possible to measure *in-situ* the resistance of the sample.

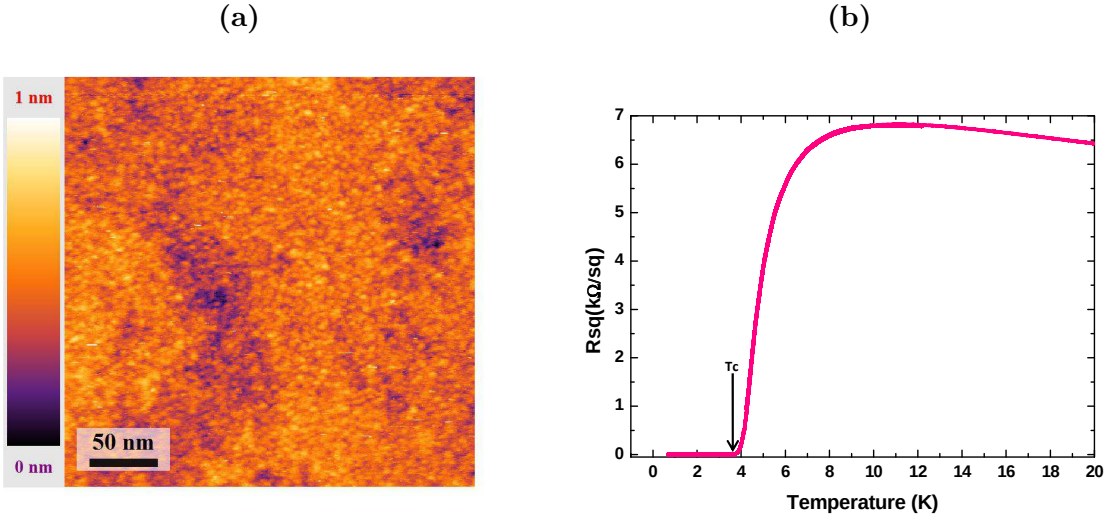

Figure 6.1: *(a) Scanning tunneling topography of the studied sample showing a roughness of few Angströms. All the measurements have been done on the same place. (b) Four-probe resistance as a function of temperature measured in-situ on the 2.14nm thick sample.*

During this experimental run, only one sample was studied. Its nominal thickness was 2.14nm and its Tc was 3.8K (see the resistance curve in figure 6.1-b). The critical temperature in this case is defined as temperature at which the measured resistance reaches zero when decreasing the temperature. Thus, this sample is closer to the insulating transition than the previous one since $Tc/T_{C0} \simeq 0.25$. With T_{C0} the bulk superconducting transition temperature.
All measurements we will show in this chapter have been done at the same region of the sample which is shown on figure 6.1-a.

In figure 6.2 a zoom of the area of interest is shown. We observed in STM topographic images that the sample is made of nanocrystallites that have a typical size of 5nm to 10nm. This is consistent with the Transmission Electron Micrscopy measurements we performed on a 2.33nm thick sample. On the profile plotted in figure 6.2, one can see that the apparent roughness does not exceed 0.5nm except some selected grains.

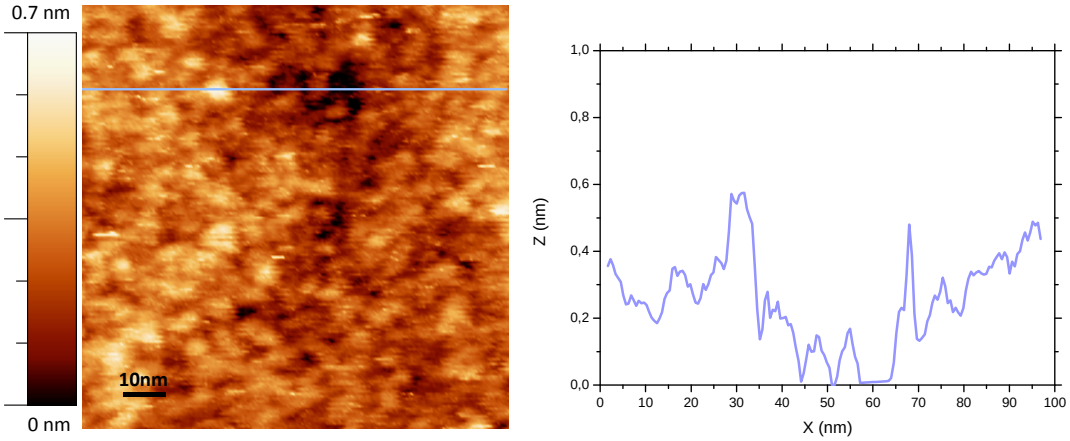

Figure 6.2: *Zoom on the topography of the interest area of the sample. Nanocrystallites having a size of 5 to 10nm are visible. This observation is consistent to what observed with the TEM. The profile of the surface shows only slight thickness variations.*

6.2 Phase diagram

The temperature and the magnetic field can be varied in order to tune the transition between the superconducting and a non-superconducting state. Figure 6.3 shows the points of the B-T phase diagram that were studied during this experimental run. In orange is the superconducting state (SC) and in yellow is the cross-over region where Rsq $\neq 0$ and Rsq $<$ R(10K), before the normal bad metal state. The black line which delimits the superconducting state has been determined experimentally on the basis of the measured points that are shown in figure 6.3. It is noticeable that it is not what is expected for the type II superconductors as shown in figure 1.3.
The temperature has been increased from 300mK to 7K and the magnetic field was varied from 0T to 7T. First, we will compare the results obtained at the same area of the sample shown in figure 6.1 between 300mK and 4.2K and up to 6T. In the second experimental run, the temperature and the magnetic field have been increased more. The tip has been changed and thus, the studied area also changed.

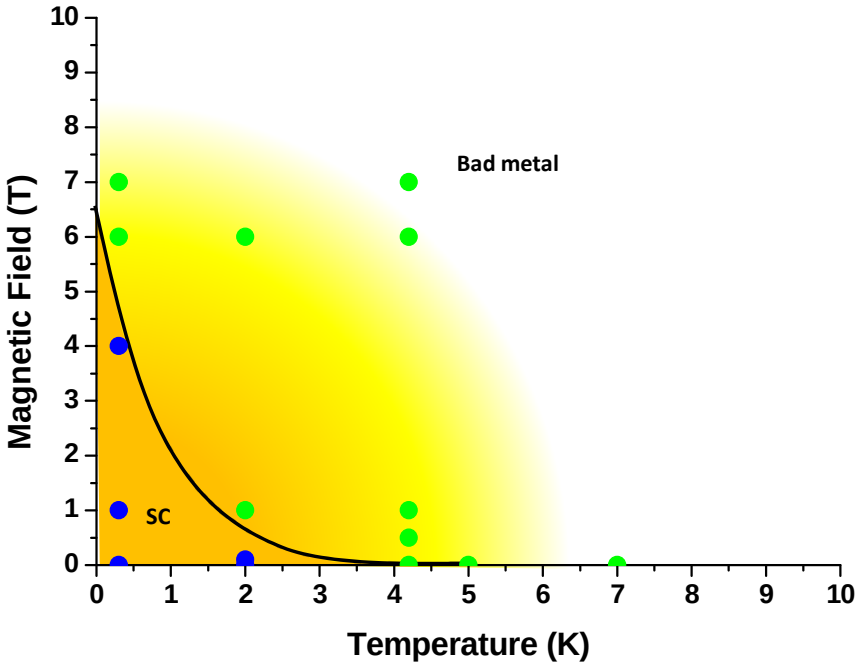

Figure 6.3: *B-T phase diagram representing point corresponding to all situation studied by STS. The transition between the superconducting state (SC) and the bad metal state is induced by varying the temperature or the magnetic field. In blue are the points corresponding to the superconducting state, when the measured resistance is truly zero, and in green are the points for which the resistance of the film is different from zero.*

6.3 Nanoscale spectroscopic properties at low temperature

At low temperature when the sample is superconducting and the measured resistance is zero, some inhomogeneities are present, as can be seen in figure 6.4. It is the zero bias conductance map which is plotted at each point of the 256x256 spectroscopic grid. The spatial resolution is of 1.2nm, and the spectral resolution is about 0.02mV. More details on the measurement parameters are given in chapter 3 section 3.3.2.
The STS map clearly shows a superconducting gap in the local tunneling spectra. The shape of the spectra varies in space. The inhomogeneities affect both the height of the coherence peaks and the width of the gap. Figure 6.4 shows the gap values over the conductance map. Since it is not possible to fit the superconducting gap with the BCS theory, the gap Δ is defined as the peak-to-peak value. This first result is in perfect agreement with what was observed previously at 2K on thicker samples (see chapter 4) namely, the emergence of an electronic granularity induced by disorder. However, it is noticeable that the dI/dV spectra have now sharp peaks at 300mK. Indeed, the energy resolution is better than at 2.3K and allows to resolve the coherence peaks everywhere over the area. Nevertheless, there is no conservation of the spectral weight since the gap develops on a V-shape background. We will discuss this point later.
The map of the spatial variations of the gap width is shown in figure 6.5.
It is noticeable that the ratio Δ/k_BTc is about 6. In our previous study of thicker samples, the ratio was constant as a function of thickness and equal to about 4. Thus with larger disorder, closer to the superconductor-insulator transition, we find a behavior similar to

the case of TiN, InO and thick NbN films, i.e. Tc and Δ start to decouple.
At T=300mK and B=0T, the characteristic length scale of the inhomogeneities varies from 25nm to 50nm, which is larger than the coherence length. When the temperature or magnetic field vary the spectral fingerprint of local inhomogeneities changes but spatially they remain fixed. Thus, they are intimately related to intrinsic disorder.

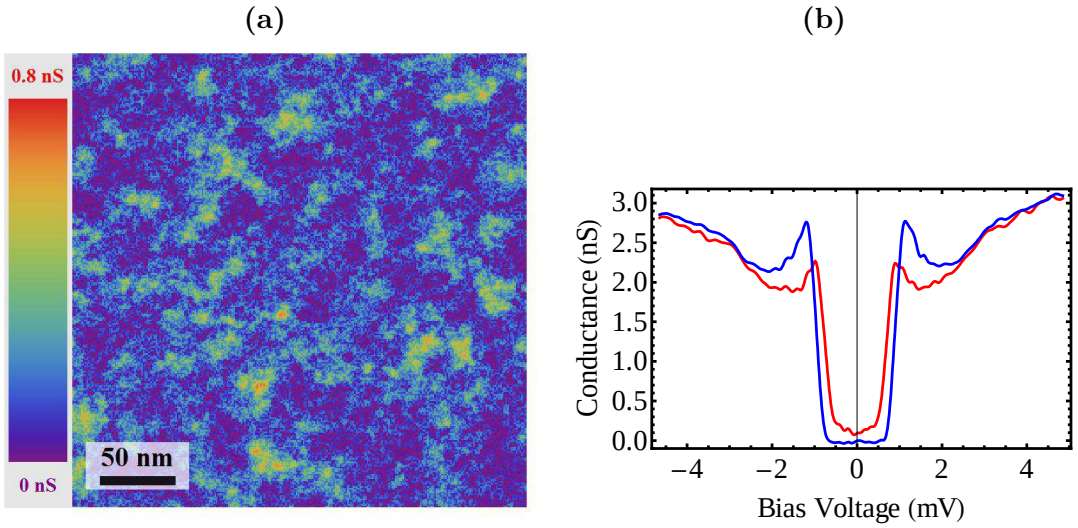

Figure 6.4: *(a) Tunneling spectroscopy dI/dV(V=0) conductance map measured at 300mK and in zero magnetic field. The color code represents the spatial variations of the dI/dV signal. Spectral inhomogeneities are visible, attesting for an emergent granularity. (b) Individual tunneling dI/dV spectra representative of the inhomogeneities observed in the conductance map. Blue spectra is measured in a blue zone and red spectra in a red/yellow one.*

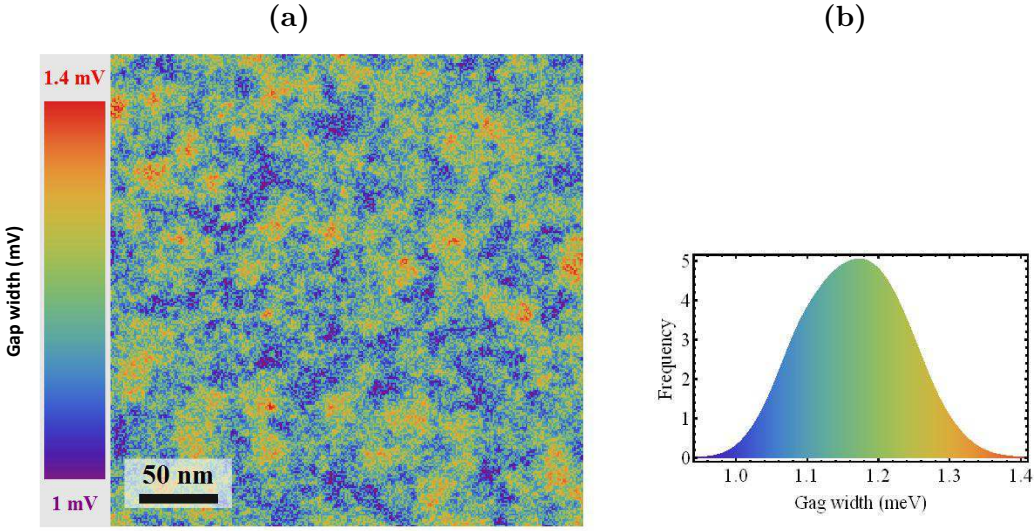

Figure 6.5: *(a) Superconducting gap map corresponding to the conductance map in figure 6.4 and showing the spatial variations of the gap width. The gap Δ is defined as the peak-to-peak value. (b) Histogramm of the frequency of the gap width, the mean value is 1.2meV.*

6.4 Temperature effect on the spectroscopic properties

6.4.1 Evolution of the conductance map with the temperature

It is interesting to study how the temperature can affect the superconducting properties. The macroscopic resistance measured *in-situ* is zero at 300mK and 2K but increases to 1kΩ/sq at 4.2K thus approaching the bad metal state. The three conductance maps measured at these temperatures are shown in figure 6.6. The white or black circles are landmarks of identical location in the three images. It is noticeable from the comparison of the conductance maps that the size of the area having a weakened gap increases with increasing temperature, both between 300mK and 2K and then between 2K and 4.2K. Moreover, the various patterns forming the inhomogeneities observed at 300mK are still at the same place when increasing the temperature.
At 2K, the coherence peaks are already very small but still present in the majority of conductance spectra : they are visible on the blue spectra, thus they are present in all blue zones of the spectroscopic map. On the other hand, in the bright regions, the coherence peaks have almost disappeared. Since at 4.2K Rsq=1kΩ/sq, these bright regions at 2K are most probably about to become non-superconducting and drive the transition to the normal state.
At 4.2K, the sample is no more superconducting but the density of states is not constant, contrary to what is expected for a normal metal. Indeed, there is a dip in the dI/dV spectra at zero bias. We can conclude that the density of states measured at 4.2K is representative of the bad metal normal state of the sample.
When increasing the temperature further, the conductance becomes more and more homogeneous and the inhomogeneities well seen at 300mK tends to disappear. However, there is still some local variations of the zero bias conductance. The blue regions are probably small superconducting areas that remain in a non-superconducting matrix. These regions correspond to the large gap regions at 300mK.
From the comparison of the maps at 2K and 4.2K, we see directly that this transition is percolative in nature.

T=300mK and R=0Ω/sq

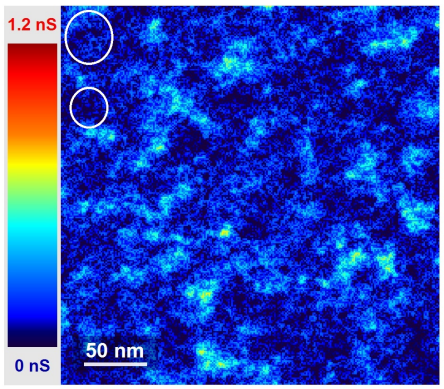

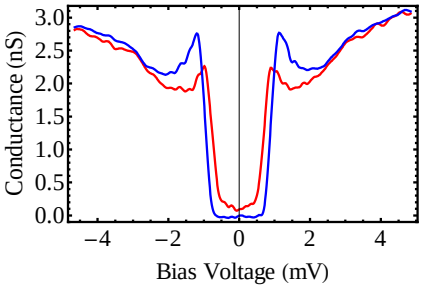

T=2K and R=0Ω/sq

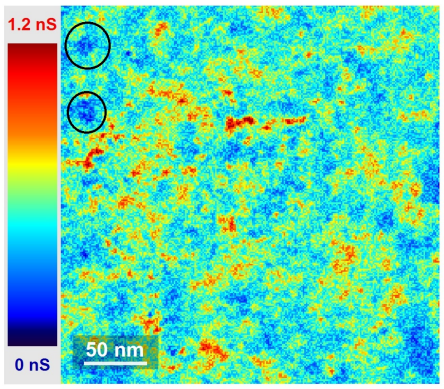

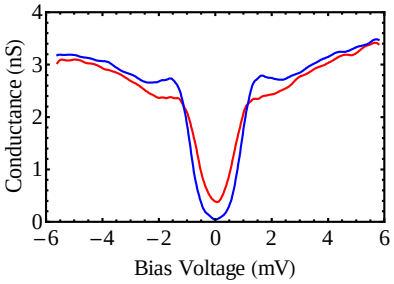

T=4.2K and R=1020Ω/sq

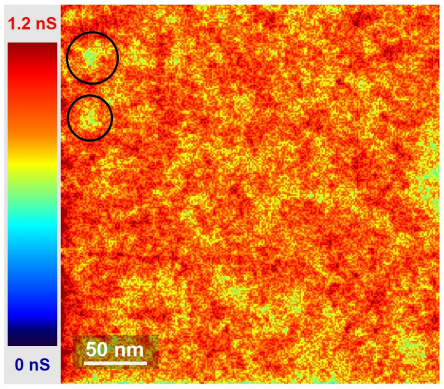

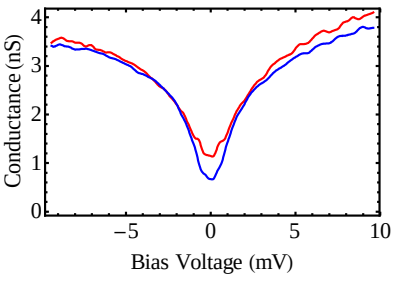

Figure 6.6: *First line: Conductance map and representative spectra of the spatial variations observed among them at 300mK when R=0Ω. Second line: Conductance map and representative spectra of the spatial variations observed among them at 2K when R=0Ω. Third line: Conductance map and representative spectra of the spatial variations observed among them at 4.2K when R=1020Ω/sq. These three maps are measured at the same location as the area shown in figure 6.1.*

6.4.2 Conductance map above Tc

In figure 6.7-b we show a zero bias conductance map measured at 7K. The corresponding topography is shown in figure 6.7-a. These STS data correspond to the second experimental run, and thus have not been measured over the same sample area. However, it is clear that when increasing more the temperature above Tc, the gap is closing and the conductance become completely homogeneous. The characteristic spectra displayed in figure 6.7-c highlight the presence of the V-shape background in the bad metal normal state.

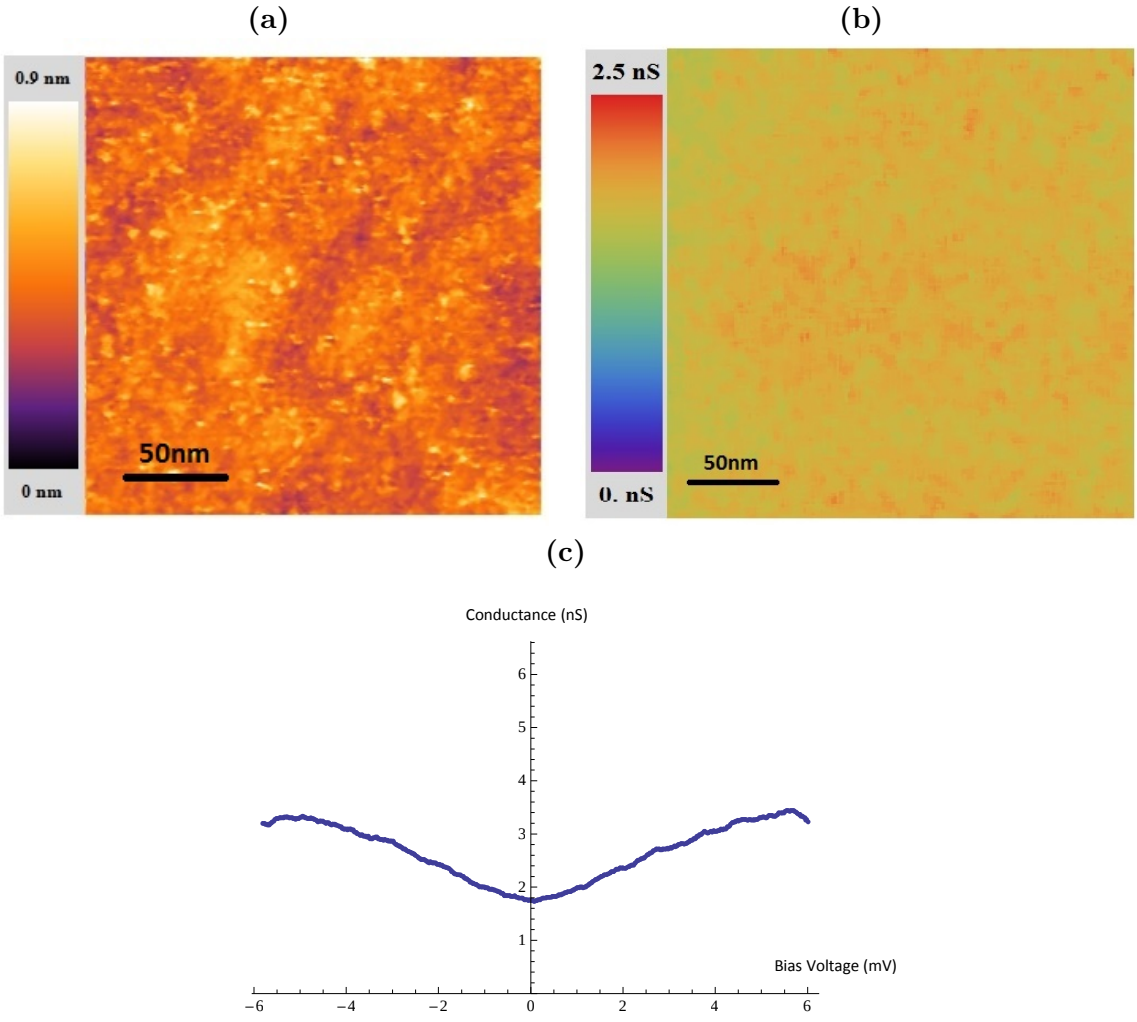

Figure 6.7: *a) STM topography image measured at 7K. The typical nanocrystallites composing the samples are visible. b) Corresponding zero bias conductance map measured at 7K. It becomes completely homogeneous when increasing the temperature well above Tc. c) Characteristic spectrum measured on this conductance map.*

6.5 Magnetic field effect on the spectroscopic properties

6.5.1 At 300mK

When applying a magnetic field of 1T at 300mK, the *in-situ* measured macroscopic resistance is still zero. It means that the sample is globally in the superconducting state. With zero magnetic field, the inhomogeneities described before are present : there are some areas with smaller gap which are in red/yellow in the conductance map, the other zones with bigger gap are in blue (see figure 6.8).
In a magnetic field of 1T, the vortex lattice appears. The vortices appear in the regions with the highest conductance (red or yellow) that corresponds to weakened superconducting gap at 0T. We indicate the location of pinned vortices in these high conductance area by the three arrows in figure 6.8. In this figure, the spectra in red are measured on the red/yellow areas, namely the vortex core and the spectra in blue are measured in the blue areas, namely the superconducting areas. It is noticeable that in the vortex core, we measured a V-shape pseudo-gap-like spectrum reminding the characteristic "bad metal" normal state of this sample and the coherence peaks disappeared. In the superconducting areas that do not exhibit sharp peaks when measured at 300mK and zero magnetic field, the coherence peaks almost disappear because they are damped by the applied magnetic field.
The vortex lattice is disordered but tends to form an hexagonal pattern as can be seen on figure 6.8. It is worth noting that the vortex density is the correct one expected at 1T. Indeed, we measure a distance of 50 nm between two vortices.

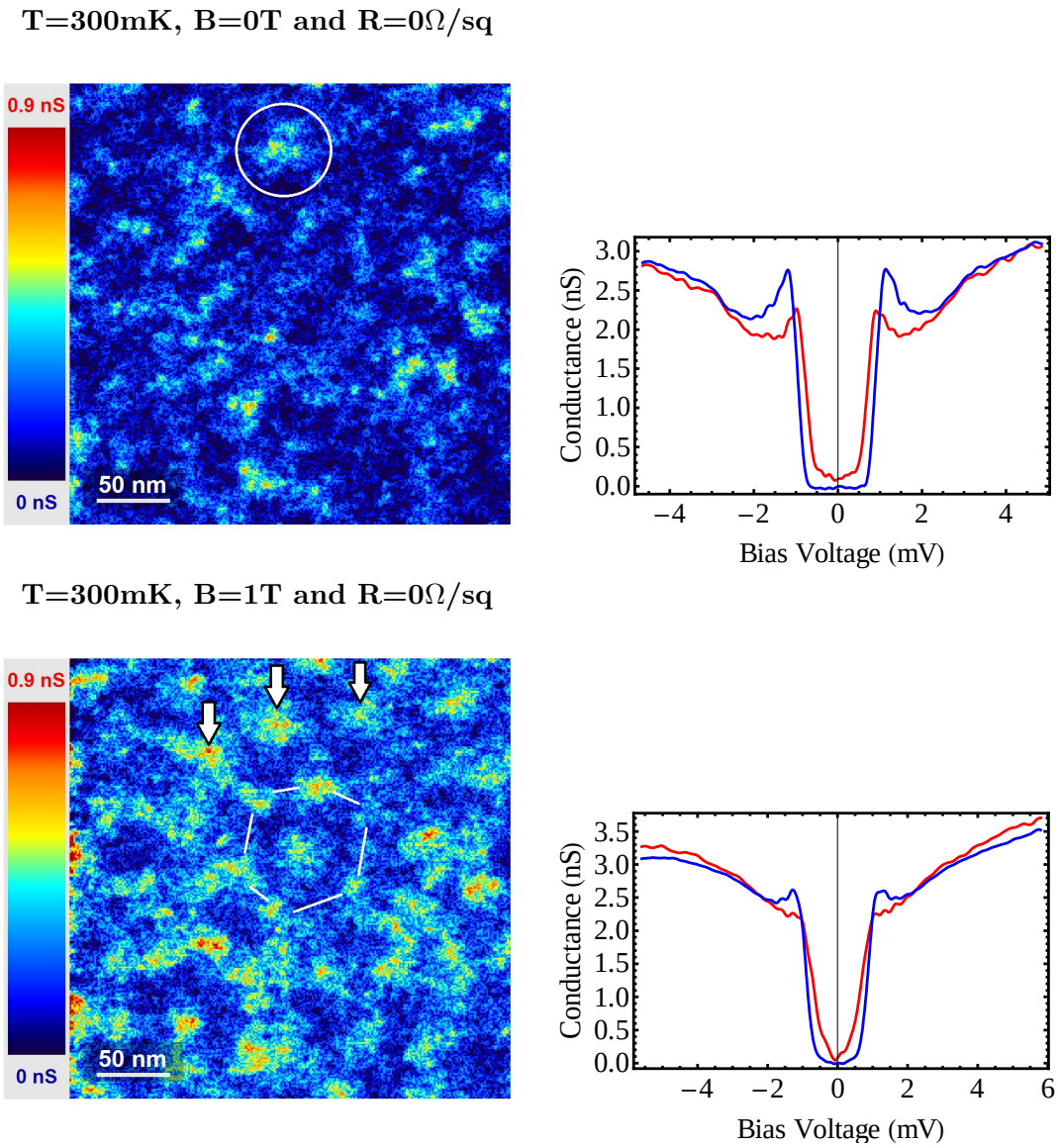

Figure 6.8: *First line: dI/dV(V=0) conductance map and representative spectra of the spatial variations observed among them at 300mK and 0T when R=0Ω/sq. Second line: Conductance map and representative spectra of the spatial variations observed among them at 300mK and 1T when R=0Ω/sq. These two maps are measured at the same location as the area shown in figure 6.1.*

6.5.2 At 2K

At 2K and without magnetic field, the sample is in the superconducting state. Indeed, the measured resistance is zero. Nevertheless, when applying a magnetic field, the sample becomes quickly resistive. At 1T, the resistance is already 83Ω/sq and at 6T, the resistance increases to 2.4kΩ/sq.
In zero magnetic field, the conductance map (figure 6.9) shows areas which differ by their spectral fingerprint. In the blue areas, the dI/dV spectra still have small coherence peaks. But in the red/yellow areas the gap exhibits no coherence peaks. The sample is superconducting, thus there is a majority of blue areas.
When applying 1T, the sample is at the percolative threshold : indeed, the inhomogeneities observed previously are still at the same place but it is difficult to distinguish if it is the blue areas or the red/yellow areas that cover a larger surface. At this cross-over field between the superconducting and the bad metal state, the spectra have no coherence peaks in the brighter regions (corresponding to the spectra in red in figure 6.9 line two). Those red/yellow regions represent the larger part of the surface. In the remaining blue regions, small coherence peaks are still visible, suggesting superconducting islands, surrounded by non-superconducting regions.
Finally, at 6T, when the resistance is higher, the bad metal state is recovered. The conductance map becomes homogeneous and the dI/dV spectra show the characteristic V-shape background of the normal state. Small superconducting correlations persists in some regions where the gap was the largest at 0 field, revealed by slightly deeper dip between red and blue spectra of the third line figure 6.9.

T=2K, B=0T and R=0Ω/sq

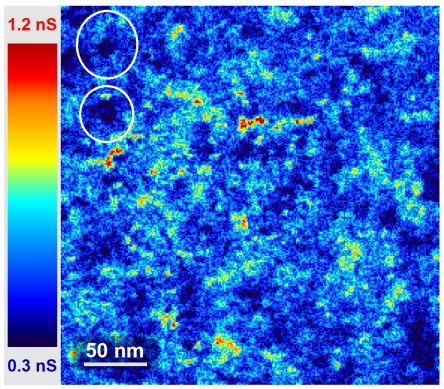

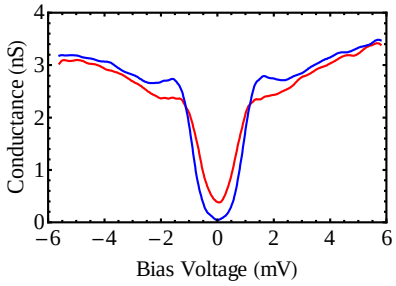

T=2K, B=1T and R=83Ω/sq

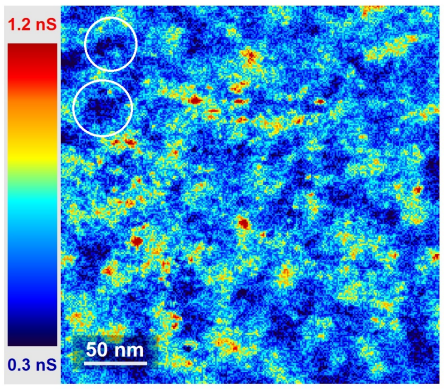

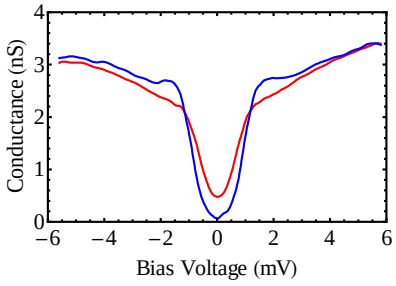

T=2K, B=6T and R=2400Ω/sq

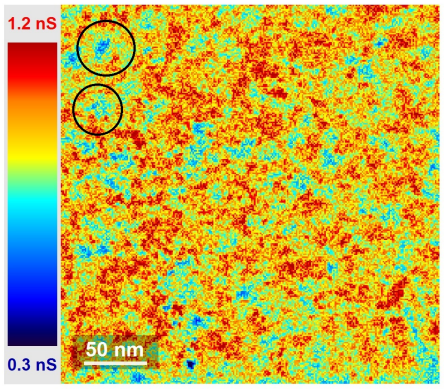

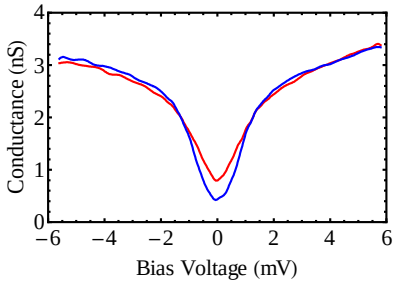

Figure 6.9: *First line: dI/dV conductance map and representative spectra of the spatial variations observed among them at 2K and 0T when R=0Ω/sq. Second line: Conductance map and representative spectra of the spatial variations observed among them at 2K and 1T when R=83Ω/sq. Third line: Conductance map and representative spectra of the spatial variations observed among them at 2K and 6T when R=2400Ω/sq. These three maps are measured at the same location as the area shown in figure 6.1.*

6.5.3 At 4.2K

Finally, we can compare these results with those obtained at 4.2K when the sample is no more superconducting even without magnetic field. At 0T, the resistance is already 1kΩ/sq. At 1T, it reaches 2.2kΩ/sq and at 6T, it increases to 5.7kΩ/sq.
Without magnetic field, there are still some inhomogeneities in the conductance map that affect the zero-bias conductance and reveal remaining superconducting regions with superconducting correlations which we know are related to larger gap regions at 300mK and 0T.
When the magnetic field increases, these inhomogeneities become weaker and the local conductance becomes more and more homogeneous. At 6T, Rsq is about twice the 300K value, and about 80% the 10K value, and the local conductance becomes almost homogeneous. The V-shape background is still present. We also observed very weak pseudo-gap spatial variations that persists in very few blue patches.

T=4.2K, B=0T and R=1020Ω/sq

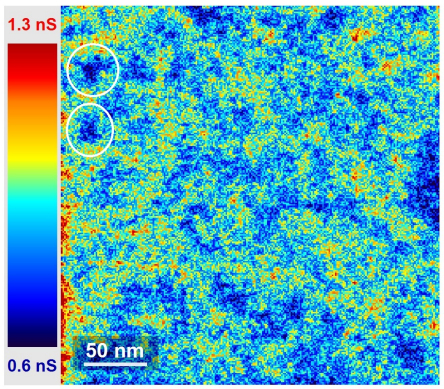

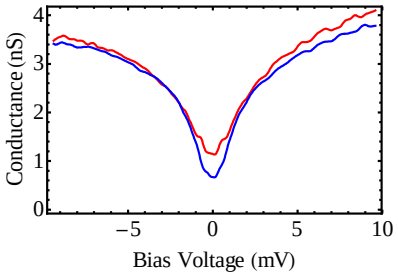

T=4.2K, B=1T and R=2200Ω/sq

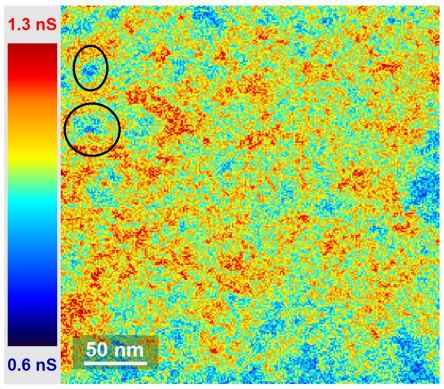

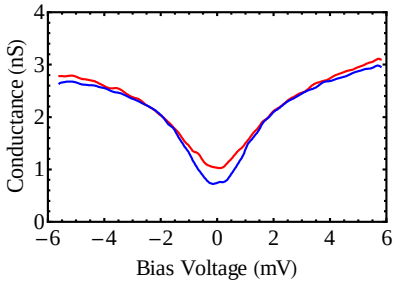

T=4.2K, B=6T and R=5700Ω/sq

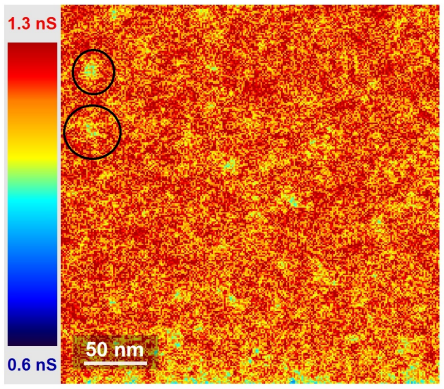

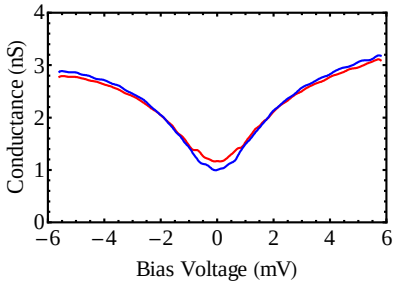

Figure 6.10: *First line: dI/dV conductance map and representative spectra of the spatial variations observed among them at 4.2K and 0T when R=1020Ω/sq. Second line: Conductance map and representative spectra of the spatial variations observed among them at 4.2K and 1T when R=2200Ω/sq. Third line: Conductance map and representative spectra of the spatial variations observed among them at 4.2K and 6T when R=5700Ω/sq. These three maps are measured at the same location as the area shown in figure 6.1.*

6.6 Study of the V-shape background

6.6.1 Electron-electron interactions and disorder

It is necessary to take into account the electron-electron interactions which are reinforced by disorder because it can lead to profound changes of the properties of the system. Indeed, Alshuler and Aronov[AA79] have shown that Coulomb interactions in systems close to the weak disorder limit ($k_F l >> 1$) lead to the appearance of an anomaly in the effective density of states at the Fermi level. It is different from the Anderson localization theory [And59] which describes the localization of the wave functions by quantum interferences but without taking into account the electron-electron interactions.
Coulomb interactions reinforce the diffusive motion of the electrons : it results in a decrease of the dynamic screening of the Coulomb interactions. Indeed, a charge in a disordered metal will be less screened than in a clean system due to the weaker mobility of the electrons. Thereby, electronic correlations are reinforced.
In two dimensional systems, Altshuler and Aronov have shown that the effective density of states follows a logarithmic evolution with energy E [AAL80]:

$$\frac{\delta N(E)}{N_1} = \frac{1}{\pi}\frac{v(q)N_1}{E_F\tau} ln(|E|\tau) \tag{6.1}$$

where N_1 is the unperturbed density of states and $v(q)$ is a weak short-range potential that interacts with the system.

It is worth noting that tunneling experiments are the most appropriate techniques to study the Altshuler-Aronov effect since they can measure directly the zero-bias anomaly in the tunnel density of states.

6.6.2 Modelling the zero-bias anomaly

Ingold and Nazarov [IN05] have calculated the current-voltage characteristics of ultrasmall tunnel junctions, showing the so-called dynamical Coulomb blockade. It has been shown by Rollbuhler and Grabert [RG01] that the dynamical Coulomb blockade is finally equivalent to tunnel in 2D disordered metal i.e. Altshuler-Aronov effect. They determined that the current-voltage characteristic for small voltages is the following expression:

$$I(V) = \frac{exp(-2\gamma/g)}{\Gamma(2+2g)}\frac{V}{R_T}\left[\frac{\pi}{g}\frac{e|V|}{Ec}\right]^{2g} \tag{6.2}$$

with $g = R_K/R_T$ the conductance, R_T the tunneling resistance, $R_K = h/e^2$ the quantum of resistance, Ec the charging energy, Γ the tunneling rate and $\gamma = 0.5777$ the Euler constant.
This expression leads to a zero-bias anomaly of the conductance dI/dV which is reduced according to :

$$\frac{dI}{dV} \sim V^{2/g} \tag{6.3}$$

More details about the calculation can be found in [IN05]. The geometry considered by Rollbuhler and Grabert [RG01] corresponds to our system, we used the formula 6.2 to fit our data.

6.6.3 Experimental results

When measuring the local tunneling density of states in this NbN samples we observed that the superconducting gap develops on a V-shape background that becomes more and more pronounced when the film thickness is reduced, approaching to the superconductor-insulator transition. Further spectroscopy at higher energy, over ±30mV range around E_F, has been realized, and the spectra obtained can be seen in figure 6.11. The tunneling density of states at high energy is not constant as expected for a conventional superconductor but rises at high energy. The superconducting gap sets-in on this V-shape background. The coherence peaks are well defined but there is no conservation of the integrated density of states as for a BCS system. The observed background is characteristic of the Altshuler-Aronov effect. We can conclude that electron-electron interactions have an important role in the electronic properties of the NbN thin films.

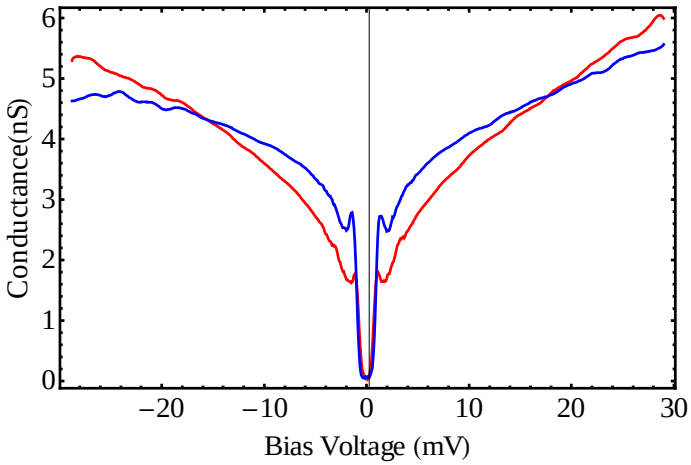

Figure 6.11: *dI/dV tunneling spectroscopy measurements of the local density of states over an energy scale about 10-15 times* Δ *:* $[-30\text{mV}; +30\text{mV}]$ *and at T=300mK and B=0T. The observed V-shape background is characteristic of the Altshuler-Aronov effect that describes bad metal films.*

We have fitted the dI/dV background by using the formula 6.3 and extracted the conductance g which is the dynamical Coulomb blockade exponent. The mean value of this exponent is 0.35 over the 300nm by 300nm area of interest shown in figure 6.1. This means that in the Ohmic model of Ingold and Nazarov, the local resistance of the environment felt by the tunneling electrons is about one third of the quantum of resistance : $0.35\ h/e^2 \simeq 4.55\text{k}\Omega$. This value is close to the square resistance measured at 10K which corresponds to the highest resistance as a function of temperature. A better fit of the data, by using a more precise formula, could lead to a better approximation of the dynamical Coulomb blockade exponent.
It is noticeable that the inhomogeneities observed in the dynamical Coulomb blockade map (figure 6.12) are at the same place that the superconducting inhomogeneities observed in the conductance map above (figure 6.4).
In the figure 6.13 we clearly see that the inhomogeneities are at the same place, with a direct correspondence between the various colored patches of the two maps. It is also possible to calculate the cross-correlation between the dynamical Coulomb blockade exponent map and the gap map measured experimentally.

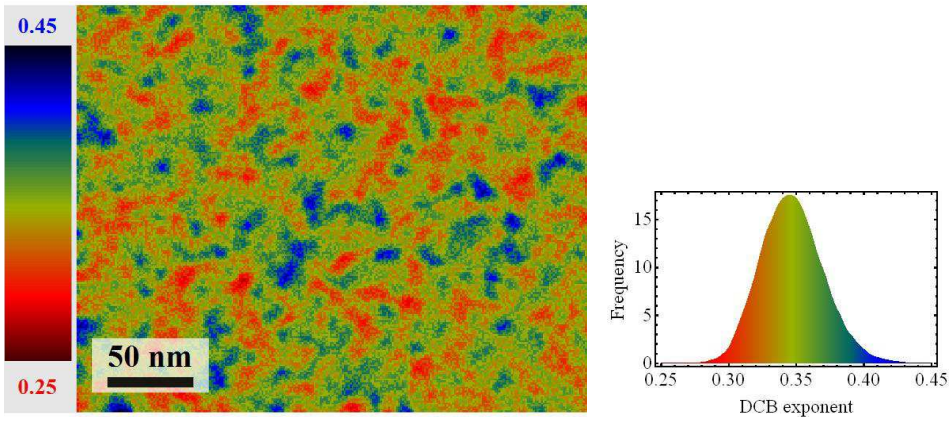

Figure 6.12: *Left: Map of the dynamical Coulomb blockade exponent extracted from the fit of all spectra measured on the area of figure 6.1 using the formula:* $dI/dV \sim V^{2/g}$. *Right: Histogram of the frequency of the value of the dynamical Coulomb blockade (DCB) exponent. The mean value is 0.35.*

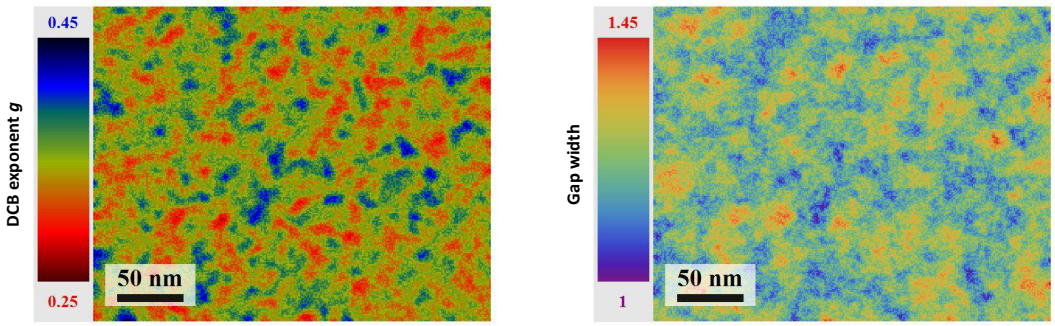

Figure 6.13: *Comparison between the dynamical Coulomb blockade exponent map (on the left) and the superconducting gap map (on the right) measured in the same area. The red and blue patches of the dynamical Coulomb blockade g map correlate directly with the red (larger gap) and blue regions (lower gap) of the studied area. This shows a direct link between the local disorder potential combined to electron-electron interactions and the local gap values.*

The correlations were calculated by using the Mathematica software. It enables to determine the intensity of the link between to two variables by using the Pearson's formula. The coefficient obtained can vary between -1 and 1. The sign determines if the two variables are correlated or anti-correlated. If the absolute value is close to 1, it means that the two variables are perfectly correlated, namely they are spatially similar. The cross-correlation map obtained between the dynamical Coulomb blockade exponent and the gap width is shown in figure 6.14. The circle at the center of the map is representative of the correlation length. Typically, in this case, the two variables g and Δ are correlated on a length scale of about 10nm. Moreover, we obtained a Pearson's coefficient of -0.56. It means that the dynamical Coulomb blockade exponent and the gap width are strongly anti-correlated. Precisely, when the V-shape due to Altshuler-Aronov effect is deeper, the local gap width is smaller. The red and blue patches of the dynamical Coulomb blockade g map (figure 6.13) correlate directly with the red (larger gap) and blue regions (lower

gap) of the studied area. This shows a direct link between the local disorder potential combined to electron-electron interactions and the local gap values.

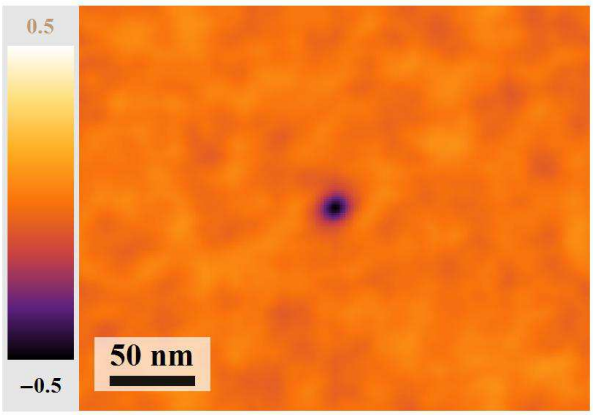

Figure 6.14: *Cross-correlation map between the dynamical Coulomb blockade exponent map and the superconducting gap map shown in figure 6.13. The black disk at the center of the image indicates that there is a strong correlation between the two map. The value obtained is -0.56 meaning that there is a strong ant-correlation between the dynamical Coulomb blockade exponent and the gap width : the smaller is the exponent, the larger is the local gap value.*

6.7 Interpretation and discussion of the results

In this 2.14nm thick NbN sample having a Tc close to 3.8K, we have found several features and properties going beyond previous reported results.

First, we have identified and performed a detailed study of the V-shape background existing in the dI/dV spectra. This background is characteristic of an Altshuler-Aronov effect that describes disordered metallic films.
By fitting the spectra, we have shown that the gap width is strongly anti-correlated with the background. Namely, when the V-shape is deeper the gap is smaller. It means that electron-electron interactions are an efficient mechanism to weaken superconductivity when increasing disorder. Such effects are not only due to localization. Our results strongly suggest that the inhomogeneities of the gap width observed, is a result of the combination of local disorder potential and strong electron-electron interaction effects. This is also consistent with the fact that for $0.4T_{c-bulk} \leq Tc \leq T_{c-bulk}$ our NbN films follow the Finkelstein law.

We observed an increase of the ratio Δ/k_BTc. Indeed, in our previous measurements, this ratio was just slowly rising with thickness reduction but it was close to 4. In the sample which is the closest to the superconductor-insulator transition among the studied ones, the ratio reaches the value of 6. This result is in agreement with the work of Sacepe et al. [SCB+08].
It is important to note that measuring the critical superconducting temperature of the sample *in-situ* enables us to have a much better precision on the determination of the ratio Δ/k_BTc. Although as for thinner samples no analytical formula exists to precisely fit the spectra, we estimated the gap value from peak-to-peak energy. In our previous work (chapter 5), the Tc was measured before the STM measurements. Due to the degradation of the sample with time and thermal cycling, the real ratio could be a bit different from the one we estimated.

When studying the evolution of the local spectroscopic properties as a function of temperature or magnetic field, we observed a percolative transition. Due to the electronic inhomogeneities described above, the system is made of puddles having a more or less large gap which spatial distribution corresponds to the Altshuler-Aronov spatial inhomogeneities we measured. When approaching the bad metal state by increasing temperature or magnetic field, the global phase coherence between the puddles will be destroyed and lead progressively to a more and more homogeneous state. The puddles can contain coherent or incoherent Cooper pairs that can survive well above Tc leading to the measured pseudo-gap that correspond to the small zero-bias conductance spatial variations above Tc. These observations might be in agreement with the transport measurements results, particularly with the changes observed in the Aslamazov-Larkin fluctuations. Indeed, our conclusion was that the system is formed of short superconducting puddles, leading to a 2D-0D cross-over when the superconducting critical temperature and the square resistance becomes below 4K. This is also consistent with the fact that the local low-temperature superconducting properties of the Tc=3.8K sample studied by STS.
Besides, the evolution of the density of states as a function of temperature is similar to the one observed recently in epitaxial NbN films [KDG+13].

Dubi et al. [DMA07] numerically modeled the superconducting condensate in the presence

of disorder, including thermal phase fluctuations. They have found spatial inhomogeneities of the local superconducting parameter. Thus, the system is made of superconducting puddles having a gap Δ, embedded in regions having a smaller gap. Since Δ remains non zero, the system is still superconducting. When increasing the temperature or the magnetic field, the global phase coherence is destroyed even if the superconducting order parameter is finite.
These simulations support the idea of a percolative transition when increasing the temperature or the magnetic field as we observed in our NbN thin film which is close to the superconductor-insulator transition.

On the other hand, pursuing their numerical approach [GRT01], Bouadim et al. [BLRT11] have studied the superconductor-insulator transition induced by disorder in thin films. They modeled the competition between superconductivity and localization but they ignored electron-electron interactions.
They have shown that, when increasing the disorder, a gap in the single-particle excitation spectrum remains finite in the insulating side and the coherence peaks vanish. They also determined the evolution of the superconductivity in weak and strong disordered samples as a function of temperature. The results they obtained are consistent with various experimental observations, including ours. Indeed, in weakly disordered film, they have shown that the superconducting gap does not close with increasing temperature as what is expected in the BCS theory. However, the coherence peaks height gradually decrease with increasing disorder and the states in the gap are filled but a pseudo-gap persists above Tc. When increasing disorder, the gap persists up to higher temperature. This is exactly the behavior we have observed in our NbN film.
Bouadim and al. simulated the local spectroscopic properties and have found that the system becomes more and more inhomogeneous when increasing disorder. They concluded from their study that the superconductor-insulator transition occurs due to the loss of global coherence between the superconducting puddles composing the system in a similar way as Dubi et al. [DMA07].
All theoretical simulation results obtained by Bouadim et al. are consistent with the experimental results we get on NbN. However, they did not take into account the electron-electron interactions while in our system we observed from our STS measurements that they are not negligible. It should be interesting to remove the Altshuler-Aronov background from our measured spectra to compare more precisely our spectra with the simulated one. Indeed, in our case, the coherence peaks disappear when increasing the temperature or the disorder. Additionally, the prediction of a gap in the two-particle excitation spectrum in the insulating phase remains a very interesting feature to be investigated experimentally with a superconducting tip.

The pseudo-spin model of Feigelman and al.[FIKC10] describes the superconductor-insulator transition in disordered thin films. This theory is not based on the effects produced by the fluctuations of the superconducting order parameter, and also neglects the Coulomb interactions. The fractal nature of the wave functions is the central phenomenon of this theory.
This theory has been developed to furnish an analytical theory able to handle situations in which : $Tc << E_F$, $|E_F - E_C| << E_F$, $\lambda << 1$, these key parameters to play with are not accessible to numerical methods. Although we observed a pseudo-gap state and the disappearance of the coherence peaks in our system too, we have no clear evidence of the fractal character of electronic inhomogeneities. The insulating state as to be studied, in

order to highlight the presence or the absence of localized Cooper pairs in the insulating state.

Chapter 7

Application: Toward a local study of superconducting nano-stripes used for single-photon detection

Contents

7.1 General informations about the single-photon detectors

7.1.1 Introduction

NbN nanowires are used to elaborate Superconducting Single-Photon Detectors (SSPD). First results on the characteristics of these devices have been obtained in 2001 by Gol'tsman and al[GOC$^+$01]. Their initial detector was a NbN wire 10nm thick and 200nm wide. They showed that when a photon is absorbed on a nanowire carrying a supercurrent, a resistive hotspot is formed. It could lead to a voltage pulse developed across the ends of the nanowire if the cross section of the nanowire is small enough. When a photon is absorbed on the nanodevice, it heated locally the system forming the hotspot and breaking Cooper pairs. Thus, the particle can be detected if its energy E is higher than the superconducting gap Δ. Then, they have shown how to improve the quantum efficiency of the detector by decreasing the thickness and the width of the superconducting wire [VZS$^+$02].
Due to their applicability in many fields where a very short time resolution and high sensitivity to low photon levels are required, these systems gave rise to a lot of interest.

7.1.2 Parameters characterizing the performance of the detectors

Several parameters are used to determine the performances of single-photon detector. The detector performance is often dependent on the application. However, one can define a number of requirements a detector must satisfy.

- The spectral range: Single-photon detectors are sensitive to a given spectral range which depends on the material used for the stripe.
- Dark count: These are detection events when no photon is absorbed but a pulse is generated at the device ends.
- Dead time: This is the time it takes after a detection event before the next event can be registered.
- Jitter: This is the time between the real absorption of the photon by the stripe and the moment that the detection occurs.

For real applications, the dark counts should be few, the dead time short (few nanoseconds) and the jitter time low (less than 50 picoseconds) in order to increase the detection efficiency and the ability to resolve the largest number of photons.

7.1.3 Detection principle

There is not only one technology which can be used to detect single-photons but in this part we focus on the Superconducting Single-Photon Detectors.
In 1996, Kadin and Johnson [KJ96] suggested a new detection mechanism, based on the nucleation of a hot point induced by the absorption of a photon on a very thin superconducting layer. This idea has been implemented by Gol'tsman and al[GOC$^+$01] who proposed a theoretical model [SGK01] of a detector based on the hot point phenomenon in NbN nanowires (few nanometers of thickness, a hundred nanometers wide and a hundreds micrometers of length).
In operation, the superconducting nanowire is biased with a direct current close to the critical current. It means that the current density flowing through the wire is close to the critical current density above which superconductivity of the wire breaks down. When a photon is absorbed by the meander, a resistive area is formed, it is named a hotspot. The heat deposited in this region will diffuse away from the absorption center and due to the short width of the wire, will ultimately render normal a whole transverse section of the wire. As a result, the superconducting current cannot cross the wire anymore. It will

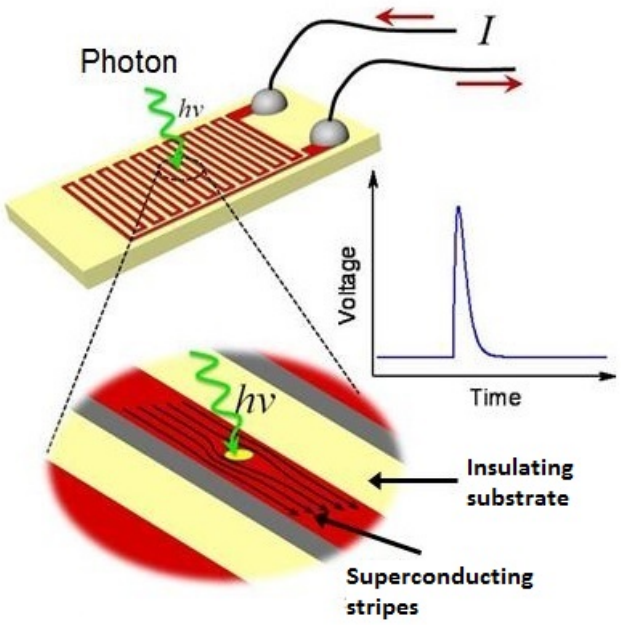

Figure 7.1: *Schematic view of the Superconducting Nano-Stripe Photon Detector operating mode. When a photon is absorbed on the wire, a resistive hotspot is formed and a voltage pulse can be detected at both ends of the meander.*

create a measurable voltage pulse across the nanowire.
In order to increase the detection surface, the superconducting wire is folded on itself to form a meander [MFS+08]. This represents a challenge for nanofabrication because the stripes should be homogeneous over all the length of the meander. Indeed, the quality of the structures limits the detector's sensitivity.

7.1.4 Motivations

The aim of this work was to study an operating detector. Especially the current repartition over the wire. It could help to determine where are the weaker area in which are located the dark count. This phenomenon limits the detection efficiency of the device, thus, ideally it has to be suppress. The current density is predicted to be higher in the corners of the meander and be the cause of the dark counts. The magnetic field could help to locate the weakened area of the nano-stripe since we know the vortex appear in the system by placing first in the area where the superconductivity is weaker.
First of all, the local spectroscopic properties at low temperature of the nano-device have to be studied without current or magnetic field.

7.2 Nanofabrication of the NbN detectors

The photon detector devices were elaborated from NbN layers similar to those we studied previously by STM. It has been proven that the meanders which have the best performances for applications have typically nanometric size ($\sim$ 5nm thick and $\sim$ 100nm wide). We have tried to reproduce the fabrication of a detector which has these operating characteristics. Obtaining such a system requires a succession of processes that will be discussed further.

The nanometric dimensions of this device make the fabrication process a delicate one. In figure 7.2 is a Scanning Electron Microscopy image of a meander that we used to test the process.

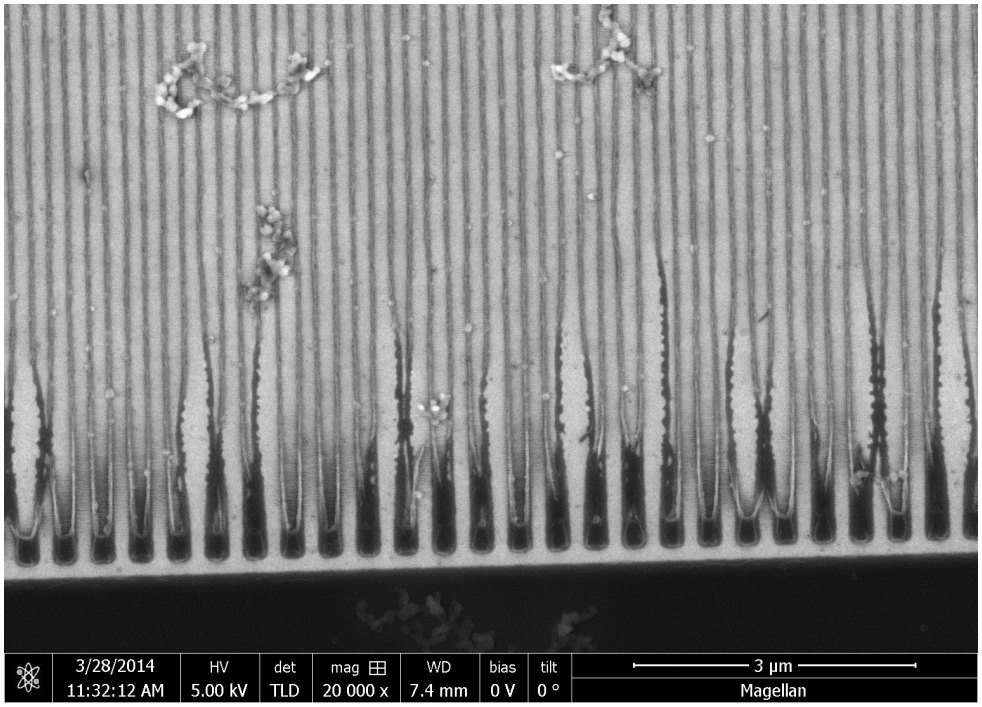

Figure 7.2: *Scanning Electron Microscopy image of a test sample for the elaboration of a NbN meander by e-beam lithography. The NbN layer has been etched to create the meander but defects are visible in the meander as well as resist residues.*

7.2.1 Sample preparation

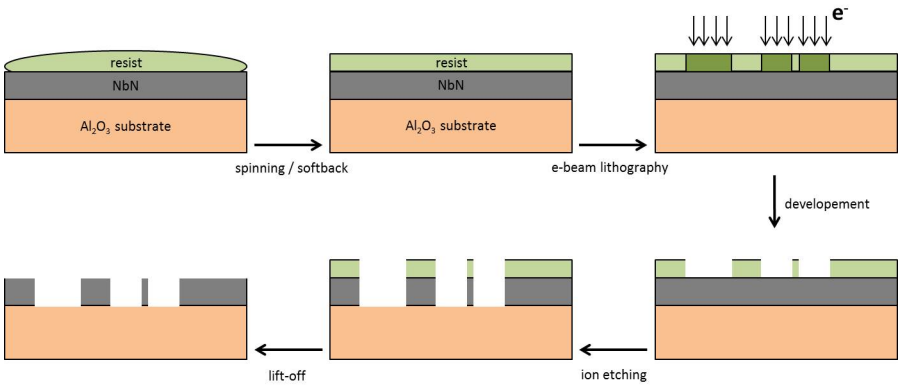

Figure 7.3: *Typical nanofabrication process: a resist is deposited on the NbN thin film that is further spinned in a coating machine and baked to obtain a uniform layer of resist. The sample is then exposed to an incident electron beam following the pre-drawn patterns. The exposed resist is removed during a development process. The sample undergoes further an ion etching step. Finally, the remaining resist is removed during a lift-off process.*

The nano-fabrication was made at ESPCI and ENS with Cheryl Feuillet-Palma and Michael Rosticher.
Working with samples of nanometric sizes render the electronic lithography an essential tool. The lithographic process consists in exposing the surface of the sample covered by a resist film, to a beam of incident electrons.
The exposed parts of the resist, Polymethyl methacrylate (PMMA), become consequently soluble in a specific developer. Thus, unexposed sample regions situated below the remaining resist areas will be kept by etching all exposed sample areas with reactive ion etching. The remaining resist is removed during the last step of the lithographic process called "lift-off". All these steps are presented on figure 7.3.

7.2.2 The resist

For this sample fabrication, A7 PMMA resist has been used. This is a standard positive resist which will be developed away in the areas exposed to the beam of electrons.
Samples were prepared for lithography by depositing few drops of PMMA on the NbN layer. Then, it is spun by a spin coating machine at 4000 revolutions/min during 30 seconds. The sample will be further heated at 130℃ for 10 minutes. That process will create a 700nm thick layer of resist.

7.2.3 Ionic etching

The Reactive Ion Etching (RIE) is an anisotropic etching process using one or more gaseous chemical species ionised by a radiofrequency field generated between two electrodes. This step has been used to transfer the resist pattern obtained after the lithography to the NbN layer. The resist acts as a mask by protecting the areas of the superconductor which should not be removed. The gas used in this process is SF_6. The thickness of NbN film to be eliminated is about 5nm. Thus, the time of etching is around 10 seconds.

7.2.4 The electronic lithography

To chose the values for the parameters like the aperture size, which determines the size of the e-beam and indirectly also the writing speed, we need to take into account the shape and characteristics size of the wanted patterns. The smaller the aperture, the longer the time the resist will be exposed to the electronic sputtering. The exposure gives the amount of charges that reach the resist per area unit. In case of overexposure, oversized patterns are to be expected while for underexposure, the development will not be complete.
Dose tests were performed in order to determine the right parameters of e-beam lithography. For the fine structures such as the meander or the positioning system, the aperture was reduced and the dose increased. On the contrary, for the delimitation of the contacts pads, the aperture was increased and the dose reduced.

7.2.5 Final appearance of the sample

During the nanofabrication of the NbN detector, a positioning system is also patterned. It will be helpfull to localize the meander on the sample surface with the AFM/STM. Indeed, in this microscope, the maximal scan size is $20\mu m * 20\mu m$ at room temperature. Moreover, It is difficult to estimate precisely the position of the tip above the sample with the camera during the first coarse approach. In figure 7.4 is visible the final appearance of the sample elaborated using the whole process described before.

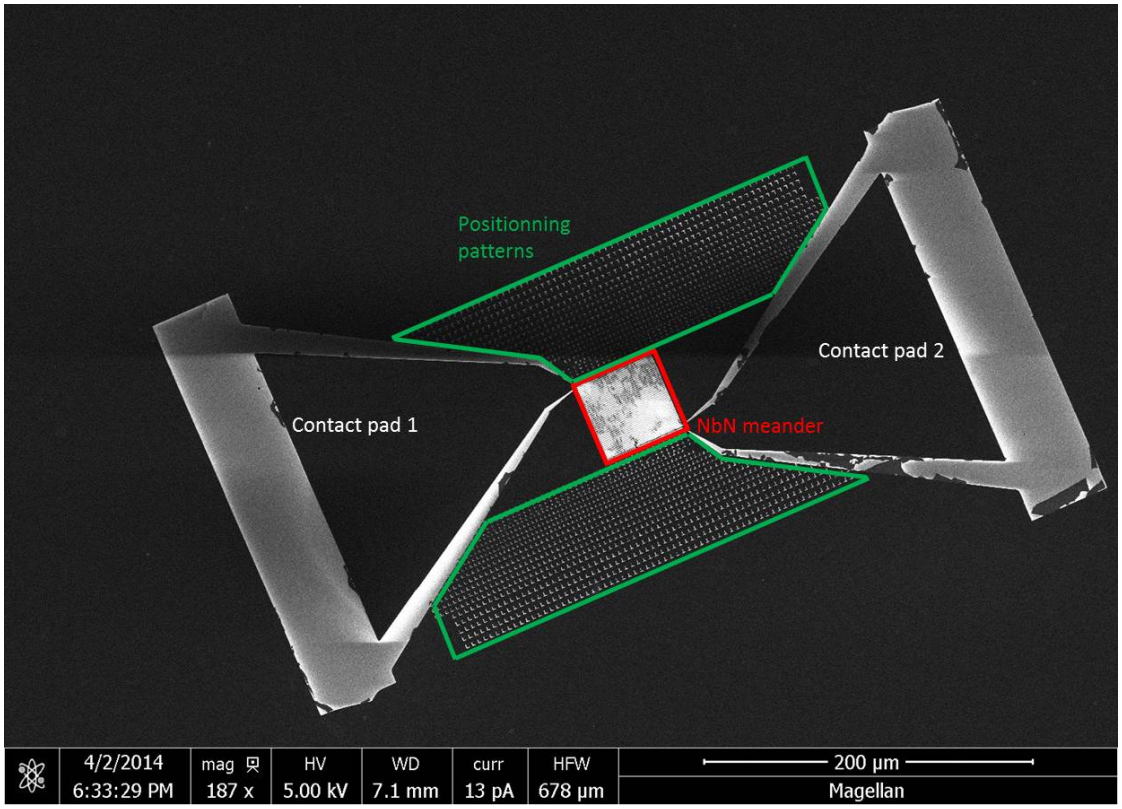

Figure 7.4: Final appearance of the patterned sample.

7.3 STM/AFM measurements of a NbN meander

Preliminary measurements have been performed at ESPCI by using a commercial JT-STM/AFM from the "SPECS" society. The lowest temperature available in this system is 1.5K but it is not yet possible to apply a magnetic field to the sample. The Kolibri sensor [1] is used to performed both STM and AFM measurements with the same tip. It is a very stable system that works in ultra-high vacuum condition.
It was a first test for the designed sample. Measurements have been performed at room temperature only and the best image has been obtained in AFM mode due to resist residues on the surface. It is necessary to improve the sample design particularly to render the pattern more visible with the camera used in small angle incidence for approaching the tip in the region of interest : the meander. Moreover, the contact pads were to close to each other and due to the spatial dimensions of the Kolibri sensor tip, it destroyed it when scanning the meander. Finally, the resist residues at the surface of the sample render the STM measurement difficult. But we succeeded to measure I(V) curves at room temperature.

1. http://www.specs.de/cms/upload/PDFs/SPECS_Prospekte/1404_SPECS-Brochure_red-KolibriSensor_RZ_Web.pdf

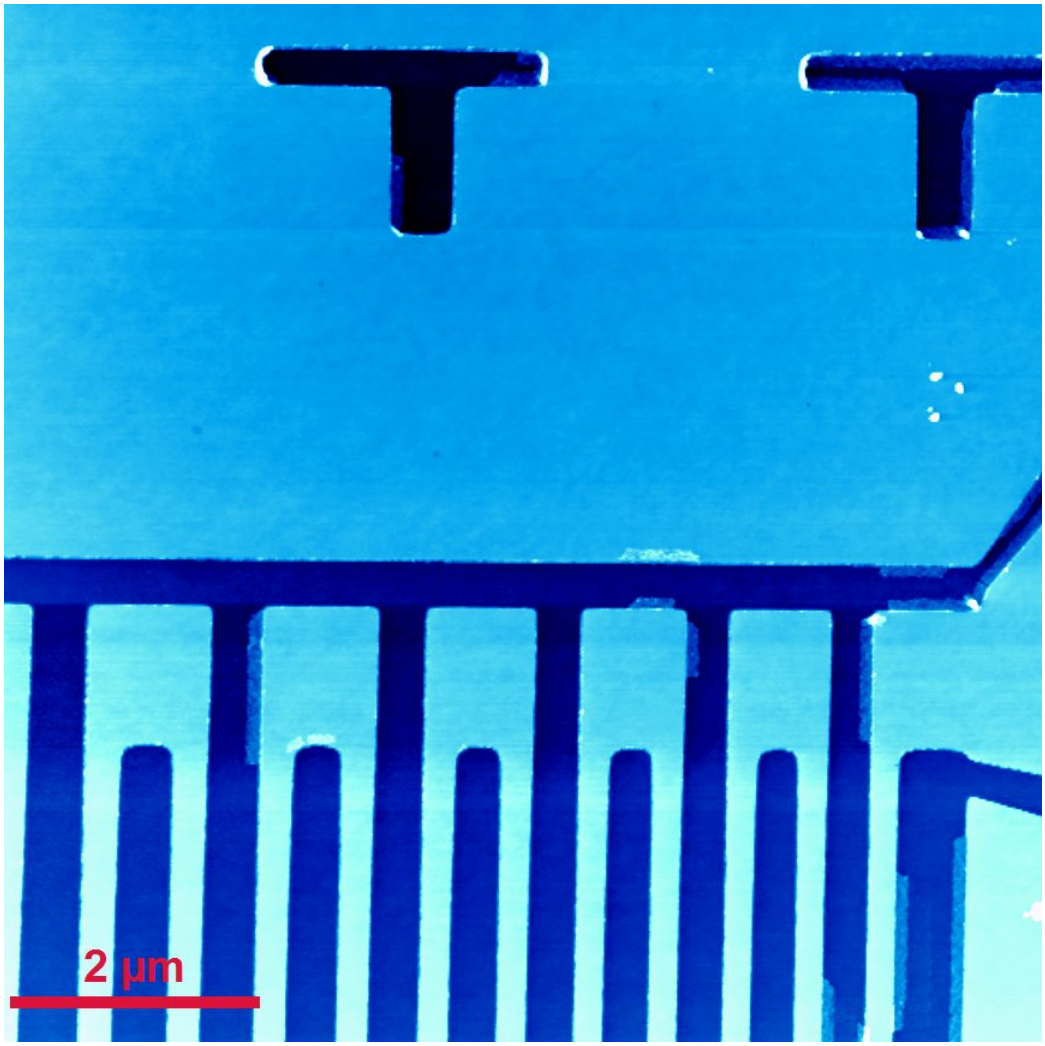

Figure 7.5: *AFM image of the NbN meander. In light blue are the areas covered with NbN wires and in dark blue are the areas where the NbN layer has been etched.*

7.4 Conclusion

These first tests are determining for a further study of the operating single-photon detector. Indeed, we developed a fabrication process that allow us to elaborate a meander with few defects. However, there are too much resist residues at the surface of the sample that render the STM measurements difficult. Moreover, we concluded from these tests that the positioning patterns have to be extend over a wider area in order to be more visible by eyes for the first approach of the tip above the meander. Last but not least, the contact pads have to separated by longer distance to let a bigger access for the Kolibri sensor.

Conclusion

The study of the superconductor-insulator transition in NbN thin films grown *ex-situ* on sapphire substrate began in our team few years ago before my own work by scanning tunnelling microscopy and spectroscopy measurements. The transition has been induced by varying the films thickness. The results have shown that while thicker films that are far from the superconductor-insulator transition have the behavior of conventional BCS superconductors, it is not the case of thinner films. Indeed, strong deviations from the BCS theory have been observed when decreasing the thickness of the NbN layer. In the range $0.4T_{C-bulk}<Tc< T_{C-bulk}$ resistivity measurements are consistent with Finkelstein's reduction of Tc induced by disorder and electron-electron interactions.
Locally, it is noticeable that inhomogeneities of the superconducting properties develop in thin films when approaching the insulating transition and lead to an emergent granularity. These inhomogeneities affect the height of the coherence peaks and the width of the gap. It has also been observed that the gap develops on a strong V-shape background. Moreover, The coherence peaks vanish in thinner samples and the vortex lattice observed in thick films disappear in sample for which Tc $\sim$ 6.7K. Since the lower temperature available with this experimental setup was 2.3K, it may be necessary to have a better energy resolution, to be able to study such a precise phenomenon.

In order to learn more about our sample characteristics, we performed Transmission Electron Microscopy on a 2.33nm thick NbN film. The measurements have been done in collaboration with Dominique Demaille (INSP) and Ludovic Largeau (LPN). We observed that the films are made of nanocrystallite that have different orientation due to the underlaying substrate of sapphire.

In a second part of my work, STM/STS measurements combined to macroscopic transport measurements have been performed *in-situ* on a NbN thin film closer to the superconductor-insulator transition with a more advanced experimental set-up (base temperature : 300mK).
It allowed us to obtain more stable and precise spectroscopy results when varying the temperature and the magnetic field, over a unique sample area.
A further detailed study of the Altshuler-Aronov effect has been done and we have shown that it is spatially varying. Furthermore, it is strongly anti-correlated with the superconducting local gap width. Namely, the conductance background is deeper when the gap is smaller. We have collaborated with Boris Altshuler and Lev Ioffe in order to improve the analysis of the experimental data and to explain theoretically the meaning of such a local correlation. A paper will be published soon.
Otherwise, we have performed a complete study of the B-T phase diagram of the local superconducting properties from 300mK to 7K and from 0T up to 7T over a single sample area of mesoscopic size. According to our results, the transition to the bad metal state induced by both the temperature and magnetic field is percolative.

In a second part of this work, we investigated the global electronic properties NbN thin films using transport measurements at low temperature, in order to learn more about the behaviour of the films under magnetic field. Our efforts concentrated on NbN thin films close to the superconductor-insulator transition. The measurements have been done in collaboration with Brigitte Leridon at ESPCI.
We have studied the evolution of the Aslamazov-Larkin superconducting fluctuations above Tc, with thickness reduction. Our results show that there is a cross-over between the 2D regime for the thicker sample (thickness$\geq$2.33nm) and 0D regime for the thinnest samples (thickness$<$2.33nm). Our theoreticians collaborators Sergio Caprara and Marco Grilli could calculate the 0D Aslamazov-Larkin fluctuations contribution. A nice agreement is found with the experimental transport data and the local STS data at 300mK characterized by an electronic granularity with patches of several nanometers size.
A scaling law analysis has been performed to study the quantum critical point of the magnetic field driven superconductor-bad metal state transition. Two determinations of the critical exponents lead to the values $\nu = 1$ and z=0.7 that are consistent with a 2D+1 XY model.
We also had the nice opportunity to perform magneto-transport measurements under high magnetic fields at LNCMI with Baptiste Vignolles. The magnetoresistance measurements highlighted the presence of a very small magnetoresistance peak. Some measurements on a sample having a lower Tc are required to know if a more pronounced peak appear. Indeed, in InO thin films, the magnetoresistance measurement exhibits the presence of a huge peaks.

In the last part of my work, we started to study one NbN meander structure used to fabricate single photon detectors patterned out of NbN films. The elaboration of the samples have been done in ESPCI and ENS, in collaboration with Cheryl Feuillet-Palma. The first goal as been reached : we succeeded to fabricate a superconducting meander by means of e-beam lithography and etching processes. Then, we could image this sample by AFM but were not able yet to perform a spectroscopic STS study. We understand from this first step the backdraws that have to be overcome to have such a study successful.

More investigations need to be pursued to establish with certainty the nature of the superconductor-insulator transition in NbN thin films. In order to approach closer to the transition, the thickness can be reduced *in-situ* by using ion gun sputtering, thus keeping a cleaner surface for STS measurements. The first try with this technique has shown that it works well.
Spectroscopic measurements on the NbN superconducting meander with and without current and magnetic field, should also give precious informations about the processes that contribute to destroy locally the superconductivity when a photon is detected. Moreover, the repartition of the superconducting current in the meander as well as precise location of vortices in the meanders are subjects of theoretical predictions that would be very interesting to check with our local probe technique. It will be continued in further studies.

Bibliography

[AA79] B.L. Altshuler and A.G. Aronov. Zero bias anomaly in tunnel resistance and electron-electron interaction. *Solid State Communications*, 30(3):115–117, April 1979.

[AAL80] B. L. Altshuler, A. G. Aronov, and P. A. Lee. Interaction effects in disordered fermi systems in two dimensions. *Physical Review Letters*, 44(19):1288–1291, May 1980.

[AALR79] E. Abrahams, P. W. Anderson, D. C. Licciardello, and T. V. Ramakrishnan. Scaling theory of localization: Absence of quantum diffusion in two dimensions. *Physical Review Letters*, 42(10):673–676, March 1979.

[Abr57] A. A. Abrikosov. On the magnetic properties of superconductors of the second group. *Soviet Physics JETP*, 5(6):1174 – 1182, 1957.

[AL68] L. G. Aslamasov and A. I. Larkin. The influence of fluctuation pairing of electrons on the conductivity of normal metal. *Physics Letters A*, 26(6):238–239, February 1968.

[And59] P. W. Anderson. Theory of dirty superconductors. *Journal of Physics and Chemistry of Solids*, 11(1-2):26–30, September 1959.

[BA71] J. J. Hanak B. Abeles. Superconducting and semiconducting phases of granular films. *Physics Letters A*, 34(3):165–166, 1971.

[Bar61] J. Bardeen. Tunnelling from a many-particle point of view. *Physical Review Letters*, 6(2):57–59, January 1961.

[BE99] I. S. Beloborodov and K. B. Efetov. Negative magnetoresistance of granular metals in a strong magnetic field. *Physical Review Letters*, 82(16):3332–3335, April 1999.

[BEL00] I. S. Beloborodov, K. B. Efetov, and A. I. Larkin. Magnetoresistance of granular superconducting metals in a strong magnetic field. *Physical Review B*, 61(13):9145–9161, April 2000.

[BLRT11] Karim Bouadim, Yen Lee Loh, Mohit Randeria, and Nandini Trivedi. Single- and two-particle energy gaps across the disorder-driven superconductor-insulator transition. *Nature Physics*, 7(11):884–889, November 2011.

[BLVE07] I. S. Beloborodov, A. V. Lopatin, V. M. Vinokur, and K. B. Efetov. Granular electronic systems. *Reviews of Modern Physics*, 79(2):469–518, April 2007.

[BV13] Tatyana I. Baturina and Valerii M. Vinokur. Superinsulator-superconductor duality in two dimensions. *Annals of Physics*, 331:236–257, April 2013.

[CAJ+07] R. Crane, N. P. Armitage, A. Johansson, G. Sambandamurthy, D. Shahar, and G. Gruner. Survival of superconducting correlations across the two-dimensional superconductor-insulator transition: A finite-frequency study. *Physical Review B*, 75(18), 2007.

[CCB+14] O. Crauste, F. CouÃ«do, L. BergÃ©, C. A. Marrache-Kikuchi, and L. Dumoulin. Destruction of superconductivity in disordered materials: A dimensional crossover. *Physical Review B*, 90(6):060203, August 2014.

[CCJ+08] S. P. Chockalingam, Madhavi Chand, John Jesudasan, Vikram Tripathi, and Pratap Raychaudhuri. Superconducting properties and hall effect of epitaxial NbN thin films. *Physical Review B*, 77(21):214503, June 2008.

[CCK+09] S. P. Chockalingam, Madhavi Chand, Anand Kamlapure, John Jesudasan, Archana Mishra, Vikram Tripathi, and Pratap Raychaudhuri. Tunneling studies in a homogeneously disordered s-wave superconductor: NbN. *Physical Review B*, 79(9):094509, March 2009.

[CDB+13] P. C. J. J. Coumou, E. F. C. Driessen, J. Bueno, C. Chapelier, and T. M. Klapwijk. Electrodynamic response and local tunneling spectroscopy of strongly disordered superconducting TiN films. *Physical Review B*, 88(18):180505, November 2013.

[CKS+11] Madhavi Chand, Anand Kamlapure, Garima Saraswat, Sanjeev Kumar, John Jesudasan, Mintu Mondal, Vivas Bagwe, Vikram Tripathi, and Pratap Raychaudhuri. Study of pseudogap state in NbN using scanning tunneling spectroscopy. In *AIP Conference Proceedings*, volume 1349, pages 61–64. AIP Publishing, July 2011.

[CMK+12] Madhavi Chand, Mintu Mondal, Sanjeev Kumar, Anand Kamlapure, Garima Saraswat, S. P. Chockalingam, John Jesudasan, Vivas Bagwe, Vikram Tripathi, Lara Benfatto, and Pratap Raychaudhuri. Magnetoresistance studies of homogenously disordered 3-dimensional NbN thin films. *Journal of Physics: Conference Series*, 391(1):012086, December 2012.

[CMX+09] Madhavi Chand, Archana Mishra, Y. M. Xiong, Anand Kamlapure, S. P. Chockalingam, John Jesudasan, Vivas Bagwe, Mintu Mondal, P. W. Adams, Vikram Tripathi, and Pratap Raychaudhuri. Temperature dependence of resistivity and hall coefficient in strongly disordered NbN thin films. *Physical Review B*, 80(13):134514, October 2009.

[Cra10] Olivier Crauste. *Etude des transitions de phases quantiques supraconducteur-isolant, metal-isolant dans des materiaux amorphes desordonnes proches de la dimension 2.* PhD thesis, UniversitÃ© Paris Sud - Paris XI, December 2010.

[CSK+12] Madhavi Chand, Garima Saraswat, Anand Kamlapure, Mintu Mondal, Sanjeev Kumar, John Jesudasan, Vivas Bagwe, Lara Benfatto, Vikram Tripathi, and Pratap Raychaudhuri. Phase diagram of the strongly disordered s-wave superconductor NbN close to the metal-insulator transition. *Physical Review B*, 85(1), 2012.

[DBC+80] G. Deutscher, B. Bandyopadhyay, T. Chui, P. Lindenfeld, W. L. McLean, and T. Worthington. Transition to localization in granular aluminum films. *Physical Review Letters*, 44(17):1150–1153, April 1980.

[DGR78] R. C. Dynes, J. P. Garno, and J. M. Rowell. Two-dimensional electrical conductivity in quench-condensed metal films. *Physical Review Letters*, 40(7):479–482, February 1978.

[DMA06] Yonatan Dubi, Yigal Meir, and Yshai Avishai. Theory of the magnetoresistance of disordered superconducting films. *Physical Review B*, 73(5):054509, February 2006.

[DMA07] Yonatan Dubi, Yigal Meir, and Yshai Avishai. Nature of the superconductor-insulator transition in disordered superconductors. *Nature*, 449(7164):876–880, October 2007.

[DWGG86] R. C. Dynes, A. E. White, J. M. Graybeal, and J. P. Garno. Breakdown of eliashberg theory for two-dimensional superconductivity in the presence of disorder. *Physical Review Letters*, 57(17):2195–2198, October 1986.

[Efe80] K. B. Efetov. Phase transition in granulated superconductors. *Journal of Experimental and Theoretical Physics*, 51(5):1015, 1980.

[FIKC10] M. V. Feigel'man, L. B. Ioffe, V. E. Kravtsov, and E. Cuevas. Fractal superconductivity near localization threshold. *Annals of Physics*, 325(7):1390–1478, July 2010.

[Fin87] A. M. Finkelstein. Superconducting transition temperature in amorphous films. *Pis'ma Zh. Eksp. Teor. Fiz.*, 45:46, 1987.

[Fin94] A. M. Finkelstein. Suppression of superconductivity in homogeneously disordered systems. *Physica B: Condensed Matter*, 197(1-4):636–648, March 1994.

[Fis90] Matthew P. A. Fisher. Quantum phase transitions in disordered two-dimensional superconductors. *Physical Review Letters*, 65(7):923–926, August 1990.

[GB84] J. M. Graybeal and M. R. Beasley. Localization and interaction effects in ultrathin amorphous superconducting films. *Physical Review B*, 29(7):4167–4169, April 1984.

[GD10] Vsevolod F. Gantmakher and Valery T. Dolgopolov. Superconductor-insulator quantum phase transition. *Physics-Uspekhi*, 53(1):1, January 2010.

[Gia60] Ivar Giaever. Energy gap in superconductors measured by electron tunneling. *Physical Review Letters*, 5(4):147–148, August 1960.

[GOC+01] G. N. Gol'tsman, O. Okunev, G. Chulkova, A. Lipatov, A. Semenov, K. Smirnov, B. Voronov, A. Dzardanov, C. Williams, and Roman Sobolewski. Picosecond superconducting single-photon optical detector. *Applied Physics Letters*, 79(6):705–707, August 2001.

[Gol10] A. M. Goldman. SUPERCONDUCTOR-INSULATOR TRANSITIONS. *International Journal of Modern Physics B*, 24(20n21):4081–4101, August 2010.

[GRT01] Amit Ghosal, Mohit Randeria, and Nandini Trivedi. Inhomogeneous pairing in highly disordered s-wave superconductors. *Physical Review B*, 65(1):014501, November 2001.

[Her01] Igor F. Herbut. Quantum critical points with the coulomb interaction and the dynamical exponent: When and why z=1. *Physical Review Letters*, 87(13):137004, September 2001.

[HLG89] D. B. Haviland, Y. Liu, and A. M. Goldman. Onset of superconductivity in the two-dimensional limit. *Physical Review Letters*, 62(18):2180–2183, May 1989.

[HP90] A. F. Hebard and M. A. Paalanen. Magnetic-field-tuned superconductor-insulator transition in two-dimensional films. *Physical Review Letters*, 65(7):927–930, August 1990.

[HRI+10] M. Hofherr, D. Rall, K. Ilin, M. Siegel, A. Semenov, H.-W. Hubers, and N. A. Gippius. Intrinsic detection efficiency of superconducting nanowire single-photon detectors with different thicknesses. *Journal of Applied Physics*, 108(1):014507, July 2010.

[IN05] Gert-Ludwig Ingold and Yu V. Nazarov. Charge tunneling rates in ultrasmall junctions. *arXiv:cond-mat/0508728*, August 2005. arXiv: cond-mat/0508728.

[JHOG89] H. M. Jaeger, D. B. Haviland, B. G. Orr, and A. M. Goldman. Onset of superconductivity in ultrathin granular metal films. *Physical Review B*, 40(1):182–196, July 1989.

[KA00] P.J Kelly and R.D Arnell. Magnetron sputtering: a review of recent developments and applications. *Vacuum*, 56(3):159–172, March 2000.

[KDG+13] Anand Kamlapure, Tanmay Das, Somesh Chandra Ganguli, Jayesh B. Parmar, Somnath Bhattacharyya, and Pratap Raychaudhuri. Emergence of nanoscale inhomogeneity in the superconducting state of a homogeneously disordered conventional superconductor. *Scientific Reports*, 3, October 2013.

[KJ96] A. M. Kadin and M. W. Johnson. Nonequilibrium photon-induced hotspot: A new mechanism for photodetection in ultrathin metallic films. *Applied Physics Letters*, 69(25):3938–3940, December 1996.

[KOM08] Haruhisa Kitano, Takeyoshi Ohashi, and Atsutaka Maeda. Broadband method for precise microwave spectroscopy of superconducting thin films near the critical temperature. *Review of Scientific Instruments*, 79(7):074701, July 2008.

[KSR+14a] P. Kulkarni, H. Suderow, J. Rodrigo, S. Vieira, M. R. Baklanov, T. Baturina, and V. Vinokur. Conductance behavior with temperature and magnetic field in the disordered films of titanium nitride. *arXiv:1402.0395 [cond-mat]*, February 2014. arXiv: 1402.0395.

[KSR+14b] P. Kulkarni, H. Suderow, J. Rodrigo, S. Vieira, M. R. Baklanov, T. Baturina, and V. Vinokur. Electronic charge density modulations in the disordered film of titanium nitride. *arXiv:1402.3178 [cond-mat]*, February 2014. arXiv: 1402.3178.

[KT73] J. M. Kosterlitz and D. J. Thouless. Ordering, metastability and phase transitions in two-dimensional systems. *Journal of Physics C: Solid State Physics*, 6(7):1181, April 1973.

[LKSA11] Wei Liu, Minsoo Kim, G. Sambandamurthy, and N. P. Armitage. Dynamical study of phase fluctuations and their critical slowing down in amorphous superconducting films. *Physical Review B*, 84(2), 2011.

[LPW+13] Wei Liu, LiDong Pan, Jiajia Wen, Minsoo Kim, G. Sambandamurthy, and N. P. Armitage. Microwave spectroscopy evidence of superconducting pairing in the magnetic-field-induced metallic state of InOx films at zero temperature. *Physical Review Letters*, 111(6), 2013.

[Mak68] Kazumi Maki. The critical fluctuation of the order parameter in type-II superconductors. *Progress of Theoretical Physics*, 39(4):897–906, January 1968.

[MCM+99] N. Markovic, C. Christiansen, A. M. Mack, W. H. Huber, and A. M. Goldman. Superconductor-insulator transition in two dimensions. *Physical Review B*, 60(6):4320–4328, August 1999.

[MF81] Sadamichi Maekawa and Hidetoshi Fukuyama. Effects of localization on superconducting transition in two-dimensional disordered systems. *Physica B+C*, 107(1-3):123–124, August 1981.

[MFS+08] Shigehito Miki, Mikio Fujiwara, Masahide Sasaki, Burm Baek, Aaron J. Miller, Robert H. Hadfield, Sae Woo Nam, and Zhen Wang. Large sensitive-area NbN nanowire superconducting single-photon detectors fabricated on single-crystal MgO substrates. *Applied Physics Letters*, 92(6):061116, February 2008.

[MKAP+08] C. A. Marrache-Kikuchi, H. Aubin, A. Pourret, K. Behnia, J. Lesueur, L. Berge, and L. Dumoulin. Thickness-tuned superconductor-to-insulator transitions under magnetic field in a-NbSi. *Physical Review B*, 78(14), October 2008. arXiv: 0810.2321.

[MKC+11a] Mintu Mondal, Anand Kamlapure, Madhavi Chand, Garima Saraswat, Sanjeev Kumar, John Jesudasan, L. Benfatto, Vikram Tripathi, and Pratap Raychaudhuri. Phase fluctuations in a strongly disordered s-wave NbN superconductor close to the metal-insulator transition. *Physical Review Letters*, 106(4):047001, January 2011.

[MKC+11b] Mintu Mondal, Sanjeev Kumar, Madhavi Chand, Anand Kamlapure, Garima Saraswat, G. Seibold, L. Benfatto, and Pratap Raychaudhuri. Role of the vortex-core energy on the berezinskii-kosterlitz-thouless transition in thin films of NbN. *Physical Review Letters*, 107(21):217003, November 2011.

[MKG+13] Mintu Mondal, Anand Kamlapure, Somesh Chandra Ganguli, John Jesudasan, Vivas Bagwe, Lara Benfatto, and Pratap Raychaudhuri. Enhancement of the finite-frequency superfluid response in the pseudogap regime of strongly disordered superconducting films. *Scientific Reports*, 3, February 2013.

[ML85] Michael Ma and Patrick A. Lee. Localized superconductors. *Physical Review B*, 32(9):5658–5667, November 1985.

[NCB+13] Y. Noat, V. Cherkez, C. Brun, T. Cren, C. Carbillet, F. Debontridder, K. Ilin, M. Siegel, A. Semenov, H.-W. Hubers, and D. Roditchev. Unconventional superconductivity in ultrathin superconducting NbN films studied by scanning tunneling spectroscopy. *Physical Review B*, 88(1):014503, July 2013.

[NHS+09] H. Q. Nguyen, S. M. Hollen, M. D. Stewart, J. Shainline, Aijun Yin, J. M. Xu, and J. M. Valles. Observation of giant positive magnetoresistance in a cooper pair insulator. *Physical Review Letters*, 103(15):157001, October 2009.

[OJG85] B. G. Orr, H. M. Jaeger, and A. M. Goldman. Local superconductivity in ultrathin sn films. *Physical Review B*, 32(11):7586–7589, December 1985.

[OKSS13] Maoz Ovadia, David Kalok, Benjamin Sacepe, and Dan Shahar. Duality symmetry and its breakdown in the vicinity of the superconductor-insulator transition. *Nature Physics*, 9(7):415–418, July 2013.

[Rei92] M. Yu. Reizer. Fluctuation conductivity above the superconducting transition: Regularization of the maki-thompson term. *Physical Review B*, 45(22):12949–12958, June 1992.

[RG01] JÃ¶rg RollbÃ¼hler and Hermann Grabert. Coulomb blockade of tunneling between disordered conductors. *Physical Review Letters*, 87(12):126804, August 2001.

[Sac07] Benjamin Sacepe. *Spectroscopie tunnel dans des films minces proche de la transition supraconducteur-isolant*. PhD thesis, UniversitÃ© Joseph-Fourier - Grenoble I, November 2007.

[Sac11] Subir Sachdev. *Quantum Phase Transitions*. Cambridge University Press, April 2011.

[SAK98] Efrat Shimshoni, Assa Auerbach, and Aharon Kapitulnik. Transport through quantum melts. *Physical Review Letters*, 80(15):3352–3355, April 1998.

[SCB+08] B. Sacepe, C. Chapelier, T. I. Baturina, V. M. Vinokur, M. R. Baklanov, and M. Sanquer. Disorder-induced inhomogeneities of the superconducting state close to the superconductor-insulator transition. *Physical Review Letters*, 101(15):157006, October 2008.

[SCB+10] Benjamin Sacepe, Claude Chapelier, Tatyana I. Baturina, Valerii M. Vinokur, Mikhail R. Baklanov, and Marc Sanquer. Pseudogap in a thin film of a conventional superconductor. *Nature Communications*, 1:140, December 2010.

[SDC+11] Benjamin Sacepe, Thomas Dubouchet, Claude Chapelier, Marc Sanquer, Maoz Ovadia, Dan Shahar, Mikhail Feigel'man, and Lev Ioffe. Localization of preformed cooper pairs in disordered superconductors. *Nature Physics*, 7(3):239–244, January 2011.

[SEJ+05] G. Sambandamurthy, L. W. Engel, A. Johansson, E. Peled, and D. Shahar. Experimental evidence for a collective insulating state in two-dimensional superconductors. *Physical Review Letters*, 94(1):017003, January 2005.

[SGB+09] A. Semenov, B. Gunther, U. Bottger, H.-W. Hubers, H. Bartolf, A. Engel, A. Schilling, K. Ilin, M. Siegel, R. Schneider, D. Gerthsen, and N. A. Gippius. Optical and transport properties of ultrathin NbN films and nanostructures. *Physical Review B*, 80(5):054510, August 2009.

[SGCS97] S. L. Sondhi, S. M. Girvin, J. P. Carini, and D. Shahar. Continuous quantum phase transitions. *Reviews of Modern Physics*, 69(1):315–333, January 1997.

[SGK01] Alex D. Semenov, Gregory N. Gol'tsman, and Alexander A. Korneev. Quantum detection by current carrying superconducting film. *Physica C: Superconductivity*, 351(4):349–356, April 2001.

[SGP+14] Daniel Sherman, Boris Gorshunov, Shachaf Poran, Nandini Trivedi, Eli Farber, Martin Dressel, and Aviad Frydman. Effect of coulomb interactions on the disorder-driven superconductor-insulator transition. *Physical Review B*, 89(3):035149, January 2014.

[SSD12] Katrin Steinberg, Marc Scheffler, and Martin Dressel. Broadband microwave spectroscopy in corbino geometry at 3he temperatures. *Review of Scientific Instruments*, 83(2):024704, February 2012.

[STKC70] Myron Strongin, R. S. Thompson, O. F. Kammerer, and J. E. Crow. Destruction of superconductivity in disordered near-monolayer films. *Physical Review B*, 1(3):1078–1091, February 1970.

[TH83] J. Tersoff and D. R. Hamann. Theory and application for the scanning tunneling microscope. *Physical Review Letters*, 50(25):1998–2001, June 1983.

[Tho70] Richard S. Thompson. Microwave, flux flow, and fluctuation resistance of dirty type-II superconductors. *Physical Review B*, 1(1):327–333, January 1970.

[Tin04] Michael Tinkham. *Introduction to Superconductivity: Second Edition*. Dover Publications, June 2004.

[TK82] H. Takagi and Y. Kuroda. Anderson localization and superconducting transition temperature in two-dimensional systems. *Solid State Communications*, 41(9):643–648, March 1982.

[VDG92] J. M. Valles, R. C. Dynes, and J. P. Garno. Electron tunneling determination of the order-parameter amplitude at the superconductor-insulator transition in 2d. *Physical Review Letters*, 69(24):3567–3570, December 1992.

[VZS+02] A. Verevkin, J. Zhang, Roman Sobolewski, A. Lipatov, O. Okunev, G. Chulkova, A. Korneev, K. Smirnov, G. N. Gol'tsman, and A. Semenov. Detection efficiency of large-active-area NbN single-photon superconducting detectors in the ultraviolet to near-infrared range. *Applied Physics Letters*, 80(25):4687–4689, June 2002.

[YK95] Ali Yazdani and Aharon Kapitulnik. Superconducting-insulating transition in two-dimensional a-MoGe thin films. *Physical Review Letters*, 74(15):3037–3040, April 1995.

[YMO+95] M. Yoshimoto, T. Maeda, T. Ohnishi, H. Koinuma, O. Ishiyama, M. Shinohara, M. Kubo, R. Miura, and A. Miyamoto. Atomic-scale formation of ultrasmooth surfaces on sapphire substrates for high-quality thin-film fabrication. *Applied Physics Letters*, 67(18):2615–2617, October 1995.

[ZCL+10] Tong Zhang, Peng Cheng, Wen-Juan Li, Yu-Jie Sun, Guang Wang, Xie-Gang Zhu, Ke He, Lili Wang, Xucun Ma, Xi Chen, Yayu Wang, Ying Liu, Hai-Qing Lin, Jin-Feng Jia, and Qi-Kun Xue. Superconductivity in one-atomic-layer metal films grown on si(111). *Nature Physics*, 6(2):104–108, February 2010.